

Spin-Polarized Electron Scattering at Ferromagnetic Interfaces

Daniel Christopher Hatton^{1 , 2 , 3 , 4}

17th August, 2003

¹Physics and Chemistry of Solids Group, Department of Physics, University of Cambridge, Madingley Road, Cambridge, UK. CB3 0HE

²Girton College, University of Cambridge, Huntingdon Road, Cambridge, UK.
CB3 0JG

³dan.hatton@btinternet.com

⁴This dissertation is submitted for the degree of Doctor of Philosophy.

Contents

1	Motivation	31
I	Theory of Polarized Electron Reflection	33
2	Theory	35
2.1	New Theory Introduction	39
2.1.1	Polarized Neutron Reflection	39
2.1.2	Polarized Electron Reflection	40
2.2	Amplitude Reflection Coefficient	43
2.3	Reflection of an Unpolarized Beam	46
2.4	Multi-Layers	47
2.5	Comments	50
2.6	Conclusions	51
2.7	Classical Theory	53
2.8	Motivation for Experiments	56
2.9	Literature Review	58
2.10	The Experimental Context	62
2.11	Repeated Adaptation List	67
2.12	PER Theory	69
2.12.1	Amplitude Reflection Coefficient	69
2.12.2	Unpolarized Beam	71
II	The Experimental Apparatus	77
3	Polarimetry	79
3.1	Theoretical Physics of Mott Polarimetry	79
3.1.1	The Spin-Dependence of the Scattering Potential	80
3.1.2	Cross-Section	80
3.2	The Instrument at the Cavendish Laboratory	81

3.2.1	The Channeltron	82
3.3	Systematic Errors Specific to Mott Polarimetry	85
3.3.1	Derivation and Explanation of Equation 3.7	86
3.4	Additive Offsets	88
3.5	Drift Effects	88
III	Polarized Electron Reflection Study	89
4	Chamber and Method	91
4.1	Sample Holder	91
4.2	Argon Ion Sputtering Gun	97
4.3	Electron-Beam Evaporators	98
4.4	Method	99
4.4.1	Procedure for Cleaning the $Cu(001)$ Surface	100
4.4.2	Growth and Measurement	101
4.4.3	Procedure for Conducting Polarized Electron Reflection Measurements on One Film	101
5	Results and Discussion	103
5.1	Visual Inspection of the Data	105
5.2	Traditional Estimation	114
5.3	Further Discussion and Conclusions	118
5.3.1	Why Is This Statistical Analysis Necessary?	119
5.3.2	Statistical Inference Process	124
5.3.3	Conclusions	129
5.3.4	The Details of the Inference Method	135
5.4	Intermediate Experiment 1	147
5.5	Intermediate Experiment 2	155
6	Conclusions	159
6.1	Suggestions for Further Work	162
A	Fine Details of the Experimental Method	165
A.1	Sample Placement	165
A.2	Procedure for Magnetizing a Sample	165
A.2.1	Single Magnetization Direction	166
A.2.2	Single Channeltron	167
A.3	Single Beam Energy	168
A.4	Single Beam Current	168
B	Auger Electron Spectrum Interpretation	169

IV Legal Notices 173**C GNU Free Documentation License 175**

C.1	Applicability and Definitions	176
C.2	Verbatim Copying	177
C.3	Copying in Quantity	177
C.4	Modifications	178
C.5	Combining Documents	180
C.6	Collections of Documents	181
C.7	Aggregation With Independent Works	181
C.8	Translation	181
C.9	Termination	182
C.10	Future Revisions of This License	182

List of Figures

2.1	A Figure Reproduced from “Elastic Spin-Polarized Low Energy Electron Diffraction from Non-Magnetic Surfaces” [1], Showing the Comparison between a Band-Structure Calculation (Lines) and Experimental Measurements (Vertical Bars,) on Graphs of Reflected Electron Beam Polarization, from $Ni(001)$, against Electron Energy, for a Variety of Angles of Incidence θ . For High Energies (above ~ 60 eV,) the Simpler New Theory of This Chapter Predicts an Energy-Independent Polarization. The Figure Mentions that $\phi = 0$. The Source Describes ϕ as the ‘Azimuthal Angle,’ and Explains That This Is the Angle Between Some Fixed Crystallographic Axis and the Normal to the Scattering Plane; Returning to the Source’s Source [2] Reveals That the Fixed Crystallographic Axis is [110].	38
2.2	Surface of a Bulk Magnetic Sample	41
2.3	Reflection of an Electron Wave by a Single Step in Electric Potential and Magnetic Flux Density	42
2.4	Predicted Reflected Beam Polarization against the Ratio of Weiss Field to Electric Potential, in the Sample	48
2.5	Reflection Paths for an Electron Wave in a Single Magnetic Layer	49
2.6	Current Arriving at Channeltron 1, against Rotation Angle of Sample; Points with Error Bars Show Experimental Results, and Lines Show the Predictions of Best-Fit Versions of Two Models, One with a Reflection Coefficient Independent of Angle of Incidence I , and One with a Reflection Coefficient Proportional to $\frac{1}{\cos^4 I}$	54

2.7	Current Arriving at Channeltron 2, against Rotation Angle of Sample; Points with Error Bars Show Experimental Results, and Lines Show the Predictions of Best-Fit Versions of Two Models, One with a Reflection Coefficient Independent of Angle of Incidence I , and One with a Reflection Coefficient Proportional to $\frac{1}{\cos^4 I}$	55
2.8	A Graph of the [100] Component of the Magnetic Flux Density B , Inside the Surface Layers of $Co/Cu(001)$ Samples, as Measured Using MOKE, against the [100]-Direction Applied Magnetic Field Strength H ; the Thickness of the Cobalt Layer in Any Individual Sample Is Denoted by t , and the Thicknesses Overlap with the Domain of Thicknesses Used for the Main Polarized Electron Reflection Experiments, Presented in this Thesis. These data have previously appeared in <i>Electron Spin Polarimetry Studies of Ultra-Thin Magnetic Films</i> [3].	63
2.9	A Figure Reproduced from “Elastic Spin-Polarized Low-Energy Electron Scattering from Magnetic Surfaces” [4], Showing Experimental Measurements on a Graph of Reflected Electron Beam Polarization, Due to Exchange Effects, from $Fe(110)$, as a Percentage, against Electron Energy. For High Energies (above ~ 60 eV,) the Simple, New Theory of This Chapter Predicts an Energy-Independent Polarization.	66
3.1	The Compact Retarding Potential Mott Polarimeter. G Represents the Rate at which Electrons Arrive at the Front of the Polarimeter, a the Fraction of Those Electrons that Are Accepted into the Polarimeter, and H_i the Rate at which Electrons Are Scattered towards Channeltron i	83
3.2	A Channeltron	84
3.3	A Misaligned Incident Electron Beam. Based on a diagram by Gay & Dunning [5]	85

4.1	A Schematic Diagram of the Pumps and Pressure Measurement Apparatus Connected to the Ultra-High Vacuum (UHV) Chamber, inside Which the Experiments Were Conducted; Arrows Represent Flows of Gas, and Broken Lines Represent Pressure Measurements; Pirani Gauges Measure Total Pressure in a High-Pressure Range between 4×10^{-2} mbar and 5 mbar, the Penning Gauge Measures Total Pressure in an Intermediate Range, and the Ion Gauge Measures Total Pressure in a Low-Pressure Range between 8×10^{-11} mbar and 10^{-5} mbar; the Mass Spec Measures Total Pressure, and the Partial Pressures of Individual Gas Species.	92
4.2	A Schematic Diagram of the Equipment for Preparing the Sample, Contained in the UHV Chamber; Each Arrow Represents a Flow of Matter or Energy, Described alongside the Arrow, from an Item of Equipment to the Sample, Designed to Alter the Sample in a Manner Described Later in This Chapter.	93
4.3	A Schematic Diagram of the Equipment for Measuring or Observing Characteristics of the Sample; Arrows with Hollow Heads Represent Flows of Matter or Energy into the Sample, Used To Illuminate or Excite the Sample, To Render a Measurement Possible; Arrows with Filled Heads Represent Information-Carrying Flows of Matter out of The Sample; where the Arrow Is Solid, the Experiment It Represents Has Been Successfully Undertaken in This UHV Chamber; where the Arrow Is Broken, the Experiment Is a Future Possibility; Arrows of the Same Colour All Relate to the Same Illumination or Excitation of the Sample.	94
4.4	A Photograph of the UHV Chamber, inside Which the Experiments Were Conducted	95
4.5	The Sample Holder	96
4.6	Schematic Diagram of the Argon Ion Sputtering Gun	97
4.7	Schematic Diagram of the Manganese Evaporator	98
5.1	Measured Electron Arrival Rate (Points with Error-Bars) at Detectors against Incident Beam Energy for an Incident Beam Current of $(6 \pm 0.1) \mu\text{A}$, Both Sample Magnetization Directions, and substrate 9 with No Film, and Corresponding Predictions from the New, Classical-Field Theory of Chapter 2 (Lines.)	106

5.2	Measured Electron Arrival Rate (Points with Error-Bars) at Detectors against Incident Beam Energy for an Incident Beam Current of $(6 \pm 0.1) \mu\text{A}$, Both Sample Magnetization Directions, and Thickness 5 $((12.4 \pm 1.7) \text{ nm})$ on substrate 9, and Corresponding Predictions from the New, Classical-Field Theory of Chapter 2 (Lines.)	107
5.3	Deflection of an Electron Beam by a Stray Magnetic Field . .	112
5.4	The Distance along the Polarimeter Front that the Reflected Electron Beam Is Displaced, on Reversing the Stray Magnetic Field, against Stray Magnetic Flux Density	115
5.5	Traditional Estimator of Mott Asymmetry against Film Thickness and Incident Beam Energy, for Films on Substrate 9. The Thickness Axis Has a Fractional Calibration Error of $\pm 14\%$. The Lines Are a Guide to The Eye. No Error Bars Are Shown; the Dominant Random Errors Are Those in Mott Asymmetry, Which Are of the Order of 0.005.	117
5.6	Graph of spin-averaged scattering probability Γ against energy loss window W , from the calibration data for the compact retarding-potential Mott polarimeter, provided in “High-efficiency retarding-potential Mott polarization analyzer” [6]. The error bars represent the standard deviations associated with the quantization of the author’s readings from the published graph.	127
5.7	Graph of Sherman function S against energy loss window W , from the calibration data for the compact retarding-potential Mott polarimeter, provided in “High-efficiency retarding-potential Mott polarization analyzer” [6]. The error bars represent the sums in quadrature of the standard deviation associated with the quantization of the author’s readings from the published graph, and the error quoted on the published graph.	128
5.8	A Graph of the Inferred Electrostatic Potential in the Sample, in the Null Model, against Co Thickness. The Conversion factor between the Units of Thickness on the Horizontal Axis, and More Conventional Thickness Units, Is (appendix B) $(78 \pm 11) \mu\text{m A}^{-1} \text{ s}^{-1}$	130
5.9	A Graph of the Inferred Electrostatic Potential in the Sample, in the Main Model, against Co Thickness. The Conversion factor between the Units of Thickness on the Horizontal Axis, and More Conventional Thickness Units, Is (appendix B) $(78 \pm 11) \mu\text{m A}^{-1} \text{ s}^{-1}$	131

5.10	A Graph of the Inferred Magnetic Flux Density in the Sample, in the Main Model, against <i>Co</i> Thickness. The Conversion factor between the Units of Thickness on the Horizontal Axis, and More Conventional Thickness Units, Is (appendix B) $(78 \pm 11) \mu\text{m A}^{-1} \text{s}^{-1}$	132
5.11	The Convergence of the Electrostatic Potential with No Film, Displayed as a Graph of the Iteration Mean and Root Mean Square of the Potential, for Each Model, Against Iteration Number	148
5.12	The Convergence of the Electrostatic Potential with Film Thickness 5, Displayed as a Graph of the Iteration Mean and Root Mean Square of the Potential, for Each Model, Against Iteration Number	149
5.13	The Convergence of the Magnetic Flux Density with Film Thickness 5, Displayed as a Graph of the Iteration Mean and Root Mean Square of the Flux Density, for the Main Model, Against Iteration Number	150
5.14	Measured Current at Detectors against Incident Beam Energy for an Incident Beam Current of $(108.8 \pm 0.2) \mu\text{A}$, Both Sample Magnetization Directions, and Thickness 3 $((1800 \pm 260) \text{ pm})$ on Substrate 2.	152
5.15	Histogram Showing the Sum of the Likelihood Density Functions, for Multiple Detector Current Measurements, against Current at the Detectors, for an Incident Beam Energy of $(1000 \pm 0.29) \text{ eV}$, an Incident Beam Current of $(108.65 \pm 0.4) \mu\text{A}$, Both Sample Magnetization Directions, and Thickness 4 $((2540 \pm 360) \text{ pm})$ on Substrate 2.	153
5.16	Histogram Showing the Sum of the Likelihood Density Functions, for Multiple Detector Current Measurements, against Current at the Detectors, for an Incident Beam Energy of $(1000 \pm 0.29) \text{ eV}$, an Incident Beam Current of $(108.25 \pm 0.04) \mu\text{A}$, Both Sample Magnetization Directions, and Thickness 5 $((3250 \pm 510) \text{ pm})$ on Substrate 2.	154
5.17	Measured Electron Arrival Rate at Detectors against Incident Beam Energy for an Incident Beam Current of $(6 \pm 0.029) \mu\text{A}$, Both Sample Magnetization Directions, and Substrate 4 with No Film. These data have previously appeared in <i>Electron Spin Polarimetry Studies of Ultra-Thin Magnetic Films</i> [3]. . .	157

5.18 Measured Electron Arrival Rate at Detectors against Incident Beam Energy for an Incident Beam Current of $(6 \pm 0.029) \mu\text{A}$, Both Sample Magnetization Directions, and the Film $((8.4 \pm 1.6) \text{ nm})$ on Substrate 7. These data have previously appeared in <i>Electron Spin Polarimetry Studies of Ultra-Thin Magnetic Films</i> [3].	158
---	-----

List of Tables

5.1	Recorded Cobalt Growth Conditions for the Films on Substrate 8. Thicknesses in nm Are Based on the Calibration in Appendix B	104
5.2	The Best Fit Values of the Mott Asymmetry $SP = -\frac{4Se^2\hbar m_e V_1 B_1}{12e^2 m_e^2 V_1^2 + e^2 \hbar^2 B_1^2}$	105
5.3	Visually Estimated Directions, in Which the Electron Arrival Rates Change on Moving from Magnetization up to Magnetization down	108
5.4	The Effect of the Experimental Evidence on Beliefs about Parameters in the Null (Non-Magnetic Cobalt) Model. The Parameters Are Described in Tables 5.6 and 5.7	133
5.5	The Effect of the Experimental Evidence on Beliefs about Parameters in the Main (Magnetic Cobalt) Model. The Parameters Are Described in Tables 5.6 and 5.7	135
5.6	Parameters in the Null Model, with Their Prior Probability Distributions	137
5.7	Parameters in the Main Model, with Their Prior Probability Distributions	138
5.8	The Cobalt Thicknesses Used in the Intermediate Experiments Described in This Appendix	151
5.9	The Cobalt Thicknesses Used in the Intermediate Experiments Described in This Appendix	156
A.1	The Voltages, Relative to Earth, on the Electrodes of the Mott Polarimeter, During the Polarized Electron Reflection Experiment	166

Copyright Notice

Copyright © 2002–2004, 2020¹ D. C. Hatton. Permission is granted to copy, distribute and/or modify this document under the terms of the GNU Free Documentation License, Version 1.1 published by the Free Software Foundation; with no Invariant Sections, with no Front-Cover Texts, and with no Back-Cover Texts. A copy of the license is included in the appendix entitled “GNU Free Documentation License” (appendix C), or in the file `copying.data.tex`.

This document can be found at https://github.com/danielhatton/PER_CoCu/tree/master/web/, and in transparent form at https://github.com/danielhatton/PER_CoCu/.

¹Nothing substantive changed in 2020: the changes made in that year consisted of updating URLs to take account of changes in the locations where the author stores such documents.

Preface

This dissertation is the result of my own work and includes nothing which is the outcome of work done in collaboration except where specifically indicated in the text.

Statement of Length

This dissertation does not exceed the word limit for the Physics and Chemistry Degree Committee.

History

- 2020, September 24th: version 26.3 released. This does not differ in any substantive way from version 26.2: all that's changed is that URLs have been updated to account for a change in where the author stores documents like this, and Gnuplot scripts have been edited (without changing their function) to account for non-backwards-compatible changes in the syntax of Gnuplot's command language.
- 2004, November 30th: version 26.2 released. This differs from the post-viva version, which was approved for the Ph.D., only by virtue of having this History chapter restored, the copyright terms rendered more web-friendly, and an Endorsements chapter mentioning said approval added.
- 2003, August 25th: version 21.1 released, in transparent copy only. This differs from the version submitted to the University of Cambridge, for the degree of Doctor of Philosophy, only by virtue of having this History chapter added, and the Makefile altered to allow the compilation of a usable transparent copy.

Endorsements

This thesis is in the final form, which was approved for the degree of Doctor of Philosophy at the University of Cambridge.

Abstract

A theory of polarized electron reflection, at the surface of a magnetic material, is devised, predicting that the rate of electrons leaving the surface will be

$$G = \left(\frac{e^2 V^2}{16 E_b^2 \cos^4 I} + \frac{e^2 \hbar^2 B^2}{192 m_e^2 E_b^2 \cos^4 I} \right) \frac{F}{e}, \quad (1)$$

and that the reflected beam's polarization will be

$$P = - \frac{4 e^2 \hbar m_e V B}{12 e^2 m_e^2 V^2 + e^2 \hbar^2 B^2}. \quad (2)$$

V represents the electrostatic potential inside the material, B the Weiss field inside the material, I the angle of incidence of the electron beam, E_b each incident electron's kinetic energy, and F/e the rate of electron incidence. The equations represent a lowest order Taylor expansion in $\frac{1}{E_b}$, which, for cobalt samples, renders them applicable as long as $E_b \gg \sim 700$ meV. They also involve an assumption that the topmost layer of the sample has a thickness $\gg 1$ nm.

Measurements are presented of spin-correlated electron arrival rates at a Mott-polarimeter's two detectors, from the reflected electron beam from $Co/Cu(001)$, as a function of cobalt thickness, incident energy, and incident intensity. Example results are displayed graphically in chapter 5. They are analysed using three distinct methodologies.

1. Visual inspection of the data is used to make qualitative suggestions about future directions for modelling of electron reflection processes at magnetic surfaces. A magnetization-dependent systematic error is discovered in electron arrival rates at the polarimeter's detectors, and is tentatively attributed to the deflection of the electron beam by a stray magnetic field, from the sample, or from some part of the sample holder. This raises the possibility, for the future, of using a reflected electron beam's spatial deflection, rather than its spin polarization, to characterize magnetic samples.

2. A traditional estimator of the Mott asymmetry, associated with the reflected polarization, is calculated for each combination of film thickness, incident energy, and incident intensity. Results are displayed graphically in section 5.2. The polarizations of most reflected beams from cobalt films are clearly non-zero, indicating that the experiment has successfully detected the cobalt's Weiss field. Quantitative determination of this polarization is, however, rather imprecise, and there is a puzzling non-zero asymmetry from the bare copper surface.
3. It is argued that the accuracy of the traditional estimator may be compromised by its non-linearity in the electron arrival rates; therefore, Bayesian inference is used to estimate the parameters in two adaptive models, based on the above theory, and to estimate relative probabilities for these models, equipped with the data. One model has a non-zero Weiss field in the films, the other does not. Results of the parameter estimation are displayed graphically in sections 5.3.2 and 5.3.3; quantitative estimation of the sample properties is, as for the traditional estimator, rather imprecise. The data are found to rule out a null hypothesis, in which the cobalt's Weiss field is zero, very strongly, leaving it with a posterior probability of $0.34 \times 10^{-2014444631}$, indicating firmly that the experiment has successfully detected the cobalt's Weiss field.

These measurements were preceded by a process (sections 5.4, 5.5) of trial and error, in which attempted measurements of the spin polarization of reflected electron beams revealed sources of systematic error, which were addressed by adaptations to the polarimeter, and to the experimental technique.

Acknowledgements

I'd like to thank the following:

- the Engineering and Physical Sciences Research Council, in the UK, for financial support,
- Sally Hatton, for items of help too numerous to mention,
- Tony Bland, for tuition in the physics of thin magnetic films, for supervising this project with a pleasantly light hand on the rudder, for arranging funds for equipment, for suggesting the eventual possibility of conducting polarized electron measurements on semiconductor-ferromagnet systems (chapter 2.8,) to some resistance from me at the time, for providing a copy of “Electronic Structure Calculations of Low-Dimensional Transition-Metals” [7], and for other items of help too numerous to mention,
- David MacKay, for tuition in Bayesian statistics, and for many helpful discussions,
- Peter Bode, for tuition in the principles of ultra-high vacuum physics, of molecular beam epitaxy, and of structural and magnetic characterization of surfaces, and for collaboration in the maintenance of the manganese evaporator (section 4.3,) and in the early experiments described in *Mott Polarimetry at the Cavendish Laboratory* [8], which led directly to those described in this thesis (part III) and for other items of help too numerous to mention,
- Richard Saunders, for providing teaching work,
- Roger Halls, for assistance in electronics tasks relating to the experiments (part III)
- Tim Goldrein, for safety advice, without which this project might have ended in disaster,

- Jane Blunt, for safety advice, without which this project might have ended in disaster,
- Barry Dunning, for suggesting that anomalously low count rates might be the result of saturation of the channeltrons (appendix 2.11,)
- Pete Flaxman, for tuition in matters relating to the use of cryogenic fluids and of pressurized gases,
- Tony Charnley, for tuition in matters relating to the use of vacuum pumps and of pressurized gases,
- Rik Balsod, for tuition in the principles of ultra-high vacuum physics and of general laboratory maintenance, and for assistance in engineering and manufacturing tasks related to the experiments (part III,)
- Bob Butcher, for providing teaching work,
- Julia Riley, for providing teaching work, and for involving me a number of interesting projects related to physics education,
- Geeta Saran, for assistance in the purchase of electrical equipment related to improvements in the safety of the experimental setup,
- Paola Atkinson, for recommending *Ultrahigh Vacuum Practice* [9],
- Thanos Mitrelias, for collaboration in the intermediate experiments (sections 5.4, 5.5,) in the angle-dependence measurements, and in associated hardware upgrades, for immense indulgence and patience while I took research time to work on a project of my own [10], and for other items of help too numerous to mention,
- Klaus Peter Kopper, for collaboration in the intermediate experiments (sections 5.4, 5.5,) in the angle-dependence measurements, and in associated hardware upgrades, for immense indulgence and patience while I took research time to work on a project of my own [10], for arranging the polishing of the copper crystal (section 4.2,) for undertaking MOKE measurements (sections 2.9, 5.5) and for other items of help too numerous to mention,
- Christian Gürtler, for tuition in the use of Labview software, for the loan of the temporary replacement electron gun (chapter 3,) and for assistance in the installation of that electron gun,

- Dave Johnson, for assistance in engineering and manufacturing tasks related to the experiments (part III,)
- Suresh Mistry, for safety advice, without which this project might have ended in disaster,
- Dave Powell, for tuition in the use of several items of workshop equipment, and for assistance in engineering and manufacturing tasks related to the experiments (part III,)
- Terry Stubbings, for assistance in engineering and manufacturing tasks related to the experiments (part III,)
- Bill Egelhoff, for safety advice, without which this project might have ended in disaster,
- Mathias Kläui, for valuable advice on the oral presentation of theoretical results,
- Sam Gardiner, for recommending “Giant magnetoresistance and microstructural characteristics of epitaxial *Fe-Ag* and *Co-Ag* granular thin films,” [11], “Correlation between dynamic magnetic hysteresis loops and nanoscale roughness of ultrathin *Co* films” [12], and “Correlation between crystalline structure and soft magnetic properties in sputtered sendust films” [13], and providing copies thereof,
- Ian Farrer, for suggesting an adaptation to my Makefile for L^AT_EX documents, which improved the quality of the portable document format output.

I am certain to have forgotten some individuals who deserve an acknowledgement here; I hope that they will forgive my omission.

Chapter 1

Motivation

This chapter describes the motivations for undertaking the theoretical and experimental study, of polarized electron reflection from a *Co/Cu*(001) structure, presented in this thesis. The material in this chapter will be repeated in section 2.8, and much of it may seem more lucid there, after an introduction to the theoretical principles surrounding polarized electron reflection studies; it is reproduced here because some understanding of the motives for the study is likely to be helpful in reading that theoretical introduction.

Colleagues at the Cavendish Laboratory had earlier performed a series of measurements on the system formed by growing a 0.5 ML *Mn*/6 ML *Co/Cu*(001) multi-layer [14, 15, 16]. Low-energy electron diffraction (LEED) revealed, through the existence of $(\frac{1}{2}\frac{1}{2})$ order spots, a $c(2 \times 2)$ (chessboard-like) superstructure in the plane of the film.

Three possible explanations were advanced for the $c(2 \times 2)$ superstructure [14, 15, 16]:

- Inter-diffusion of copper atoms through the cobalt layer may have led to the formation of a *MnCu* surface alloy [17, 18]. However, these experiments were performed at room temperature, which is too cold to permit significant inter-diffusion through 6 ML *Co* [19]. This suggestion was therefore ruled out.
- The manganese may have had an internal $c(2 \times 2)$ anti-ferromagnetic configuration. However, the measured $(\frac{1}{2}\frac{1}{2})$ spot intensity was ~ 10 times that predicted for magnetic diffraction of this type by Tamura et al. [20]. This phenomenon is therefore incapable of providing a complete explanation of the observed superstructure.
- An ordered *MnCo* surface alloy may have been formed. Given the evidence against the other two models, the observed diffraction pattern

was attributed to $MnCo$ alloy formation.

Magneto-optical Kerr effect (MOKE) measurements were taken by colleagues at the Cavendish Laboratory as part of the same project [14, 15, 16]. The [110] direction Kerr signal was seen to increase with the addition of manganese, in the regime where the alloy exists. The immediate reaction to this is that the system's magnetic moment is increasing, i.e. that the manganese atoms that are being added are ferro-magnetically aligned, both with each other and with the cobalt. However, the simultaneous drop in [100] Kerr signal did not paint the same picture, and it may be that a change in magneto-optical response, rather than a genuine addition of magnetic moments, is responsible for the increased [110] signal. The possibilities are in particular need of investigation, given that a series [21, 22, 23] of numerical calculations, using different approximations, have produced widely differing predictions about the magnetic properties of this system.

The polarization of a reflected electron beam from the sample surface provides an alternative to MOKE, for measuring the magnetization, through the difference, for the two electron spins, in density of states at a particular energy created by the exchange splitting, and as such provides an experiment which is interesting by virtue of having an unpredictable result. The experiments presented in this thesis, using a $Co/Cu(001)$ structure, are intended as an intermediate stage on the way to similar measurements on $MnCo/Co/Cu(001)$, although they could equally well lead to similar measurements on other multi-layer structures of more direct industrial relevance, such as metal/ferromagnet or semiconductor/ferromagnet spin valves. This possibility may help to address the conclusions, concerning the motivation for experimental research projects, of statistical research the author has presented elsewhere [10].

In addition, the measurements for $Co/Cu(001)$, in themselves, allow a trial run of estimating the parameters in the new theory of this chapter, and comparing a version of that theory, in which no Weiss field affects the probing electrons, against another version, in which an adjustable Weiss field affects the probing electrons. This task is undertaken in section 5.3.

Part I

**Theory of Polarized Electron
Reflection**

Chapter 2

Review of Published Theories, a New, Classical-Field Theory of Electron Waves as a Polarized Radiation Probe of Magnetic Surfaces, Comparison of These Theories with Published Experimental Data, and Motivation for New Experiments Presented Later in This Thesis

Theories of elastic spin-polarized electron scattering from a surface can be classified by their underlying philosophy, which may be of either a band-structure calculation or an analytical type, or by their possession or otherwise of spatial variation of the scatterer, in the plane of the surface. This gives a total of four possible types of theory:

1. band-structure theories, with spatial variation of the scatterer; Feder [24] put forward a numerical method for undertaking calculations of this type, which would make quantitative predictions about the intensities and polarizations of reflected and diffracted beams, from a sample of

a precisely specified atomic-scale structure, which, along with similar methods, has been applied to particular samples by a variety of workers [1, 4, 25, 26],

2. band-structure theories, without spatial variation of the scatterer; the method of Feder [24] can be applied in this way, but, as far as the author is aware, has not been, perhaps because ignoring the in-plane variation of the scatterer eliminates any possibility of examining diffraction orders other than the specular reflection,
3. analytical theories, with spatial variation of the scatterer; Darwin [27] produced a classical-field theory, in which an electron wave impinged on a sinusoidal electrostatic potential and magnetic flux density, whose lack of a Fourier component of zero in-plane wave-vector eliminated any possibility of examining the specular reflection, and
4. analytical theories, without spatial variation of the scatterer; the author produces a theory of this form, later in this chapter. Its lack of any in-plane variation in the scatterer means that it is valid only for the specular reflection, not for other diffraction orders.

Theories, of course, are refined (in the sense of choosing an atomic configuration for a band-structure theory, or estimating the parameters in an analytical theory,) and compared for their correspondence to reality, by their ability to match experimental results. This is primarily an experimental thesis; in part III, some experimental polarized electron reflection results, along with the means used to obtain them, are presented, and in section 5.3, they are used to estimate the parameters in the new theory presented in this chapter, and to compare, for correspondence to reality, two versions of this theory, in one of which the ferromagnetic samples exert a (statistically significant) Weiss field on the incident electrons, and in the other of which, they do not.

The only other theories mentioned above, which can be used to examine a specular reflection, are that of Feder [24], and its close relatives, and some attention should be given to the match between these theories and the experimental results of part III, and indeed the new theory of this chapter. The author has been unable to find an application of these theories to specular reflection from a copper or cobalt surface, which would allow direct, quantitative comparison with the experimental results, although one might expect, in some rather ill-defined sense, qualitative features in the specular reflections from other materials to carry over to copper and cobalt. This does not, however, prevent direct comparison of Feder-type theories with the

new theory presented in this chapter, because the latter is not designed to be chemically specific.

An important link between the band-structure theories and the new theory presented in this chapter is that, in explaining the basis of the numerical band-structure calculation, Feder [24] appears to look forward to the day when the atomic-scale structure, which is fed to the numerical method, can instead be encoded in the continuous, adjustable parameters of an analytical theory, and suggests electrostatic potential and magnetic flux density as parameters for use in this fashion. Where, in a theory based on these parameters, the scatterer has mirror symmetry about the scattering plane, as does the scatterer assumed in the new theory of this chapter, this symmetry can [24] be combined with time-reversal symmetry, to show that the reflected beam polarization, for an unpolarized incident beam, is parallel to the magnetic flux density, when the latter is either in the scattering plane, or perpendicular to the scattering plane. This provides two important tests of the plausibility of any proposed emergent-phenomena theory; the new theory presented in this chapter passes both tests.

Another such link is that a band-structure calculation has been reviewed (figure 2.1) [1], which appears to agree, to approximately the same standard of precision that is possessed by relevant measurements, to be reviewed in section 2.10, with the new theory presented in this chapter, that at incident electron energies greater than ~ 60 eV, where the Taylor expansion allows the latter to make quantitative predictions, the reflected beam polarization from a nickel (001) surface is independent of incident electron energy and of angle of incidence. Several other band-structure theories for $Ni(001)$, with different atomic structures, have been reviewed [4], which have a lesser similarity to the new theory of this chapter, and a correspondingly less good fit to experimental data to be reviewed in section 2.10 [4].

Striking differences between band-structure theories and the new theory of this chapter are:

- A band-structure theory has been reviewed [1] that predicts significant polarization (at some angles of incidence, more than 0.4) of an 82 eV electron beam, by reflection from a tungsten (001) surface. Since tungsten is not ferro-magnetic, the new theory of this chapter, because it ignores spin-orbit effects, predicts no polarization, yet it claims that 82 eV is within the region, of energies much less than the electron rest mass energy, where it is reasonable to ignore spin-orbit effects. However, experiments to be reviewed in section 2.10 suggest a way for both theories to survive this apparent contradiction between them, which will be discussed there.

Third-party copyrighted figure
omitted from version for
public online distribution

Figure 2.1: A Figure Reproduced from “Elastic Spin-Polarized Low Energy Electron Diffraction from Non-Magnetic Surfaces” [1], Showing the Comparison between a Band-Structure Calculation (Lines) and Experimental Measurements (Vertical Bars,) on Graphs of Reflected Electron Beam Polarization, from $Ni(001)$, against Electron Energy, for a Variety of Angles of Incidence θ . For High Energies (above ~ 60 eV,) the Simpler New Theory of This Chapter Predicts an Energy-Independent Polarization. The Figure Mentions that $\phi = 0$. The Source Describes ϕ as the ‘Azimuthal Angle,’ and Explains That This Is the Angle Between Some Fixed Crystallographic Axis and the Normal to the Scattering Plane; Returning to the Source’s Source [2] Reveals That the Fixed Crystallographic Axis is $[110]$.

- The same band-structure calculation for tungsten predicts [1] a polarization, which changes its sign several times, as the angle of incidence I is varied from 0 to 30° . The new theory of this chapter predicts a polarization independent of I .
- A band-structure calculation has been reviewed [1] that predicts significant polarization (up to 0.8) of the reflected beam from tungsten (001) in a few narrow (~ 20 eV) energy bands, while the new theory of this chapter predicts no polarization; however, the band-structure calculation does predict near-zero polarizations outside these bands.
- A band-structure theory has been reviewed [1] that predicts significant polarization (at some scattering plane orientations, more than 0.8) of an 60 eV electron beam, by reflection from a platinum (111) surface. Since platinum is not ferro-magnetic, the new theory of this chapter, because it ignores spin-orbit effects, predicts no polarization, yet it claims that 60 eV is within the region, of energies much less than the electron rest mass energy, where it is reasonable to ignore spin-orbit effects. However, experiments to be reviewed in section 2.10 suggest a way for both theories to survive this apparent contradiction between them, which will be discussed there.
- A band-structure theory has been reviewed [4] that predicts a reflected polarization from an iron (110) surface, which oscillates as the incident electron energy is varied, with an amplitude of ~ 0.1 . This is rather different from the constant, possibly non-zero polarization predicted for this ferro-magnetic material by the new theory of this chapter.

2.1 A New, Classical-Field Theory of Polarized Electron Reflection: Introduction

Having reviewed a number of published theoretical perspectives on polarized electron reflection, and compared them against a promised, new theory, it is now time to present that theory.

2.1.1 Polarized Neutron Reflection

Polarized neutron reflection, or PNR, is [28, 29] an established experimental technique for the measurement of layer-dependent magnetization vector in magnetic multi-layers. A multi-layer structure is [28, 29] modelled as a series of steps in nuclear potential and magnetic flux density. The amplitude

reflection coefficient for neutron waves at each step is then calculated by applying the usual [30] boundary conditions to the spin-up and spin-down wave-functions at the step, given the change in wave-vector produced by the potential step. The change in wave-vector depends on the neutron's spin direction because of the torque exerted upon the neutron magnetic moment, by the magnetic field. Therefore, the spin polarization of the reflected neutron beam, as a function of incident beam energy, provides an indicator of the depth-resolved magnetization profile of the sample.

2.1.2 Polarized Electron Reflection

Polarized electron reflection and diffraction are [25, 26] also established experimental techniques, for the characterization of magnetic surfaces. The measurement is identical to PNR except for the substitution of electrons for neutrons, and the unavailability [31, 32] of the Stern-Gerlach experiment, either for controlling the incident polarization, or for measuring the reflected polarization. The Stern-Gerlach experiment is [25, 26] typically replaced by a Mott polarimeter [33, 5, 34], for measuring the reflected polarization. Electrons have significant advantages over neutrons for this purpose: an electron beam can be produced using a device roughly equivalent to a light-bulb filament, whereas a neutron beam is typically produced using a nuclear reactor. Also, the magnetic moment of the electron is nearly two thousand times that of the neutron.

Despite the long-standing use of polarized electron reflection as an experimental technique, as far as I'm aware, there has been no attempt to develop a theoretical model of the process, along the lines of that used for PNR, in order to interpret the results in terms of the depth profile of the magnetization in the sample. My intention here is to produce an analysis of polarized electron reflection similar to that of PNR by Blundell and Bland [28, 29]. Section 2.12 includes more details of the derivations of equations, which are only sketched here.

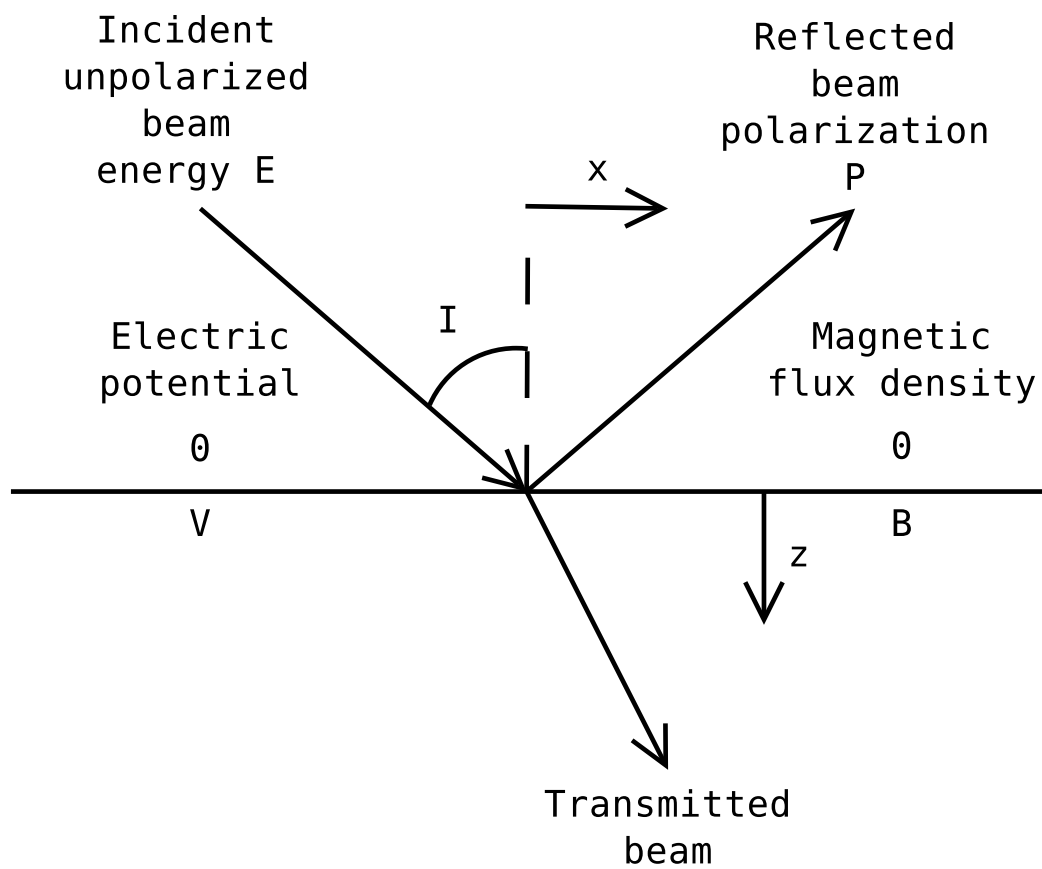


Figure 2.2: Surface of a Bulk Magnetic Sample

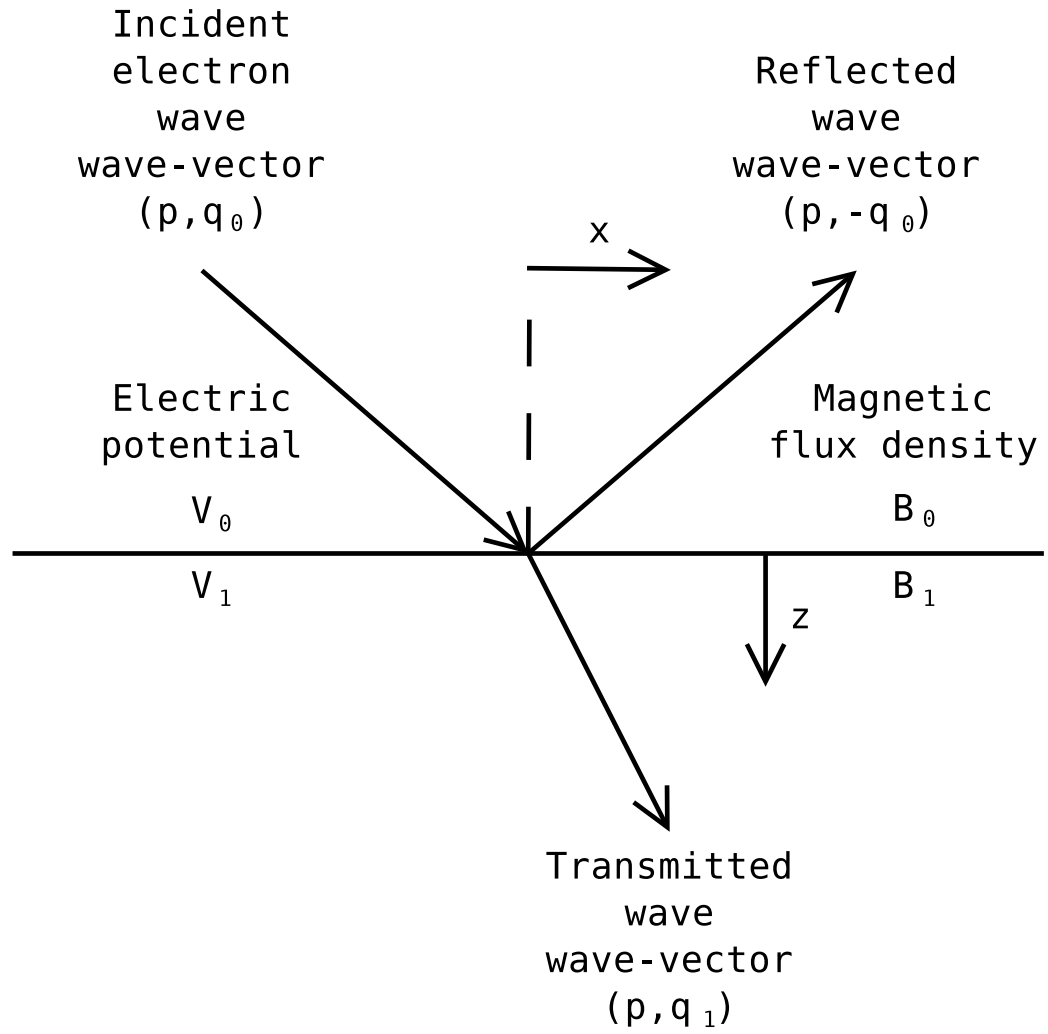


Figure 2.3: Reflection of an Electron Wave by a Single Step in Electric Potential and Magnetic Flux Density

2.2 A New, Classical-Field Theory of Polarized Electron Reflection: Amplitude Reflection Coefficient for an Electron Pure State, at a Single Step in Electric Potential and Magnetic Flux Density

The first step in the analysis of reflection is to build a potential-theory model of the sample, as a series of steps in electric potential and magnetic flux density (figures 2.2, 2.3.) The existence of sudden steps in magnetic flux density follows [35] from Maxwell's equations, for an in-plane magnetization. Shape anisotropy encourages [36, 37] the magnetizations of film structures to be in-plane, and experiments confirm [38, 39, 40, 41, 42] that the permanent magnetization in *Co/Cu*(001) is in-plane. The existence of sudden steps in electrostatic potential is supported by a comment in *Calculated Electronic Properties of Metals* [43], although this book is concerned primarily with bulk materials, and there is the possibility that steps, which are sudden on the scale of bulk materials, may be gradual on the scale of electron de Broglie wavelengths. I suspect that such a possibility would be easily detectable in the experiments, because there would be no reflection without a sudden potential step.

In reality, I expect the “magnetic flux density” part of the potential not to be a genuine magnetic flux density, but a Weiss field; in this paragraph, I will explain what the Weiss field is, and why I expect it, rather than a genuine magnetic flux density, to determine the behaviour of the electron beam. The Weiss field is a quantum-mechanical effect related to symmetry requirements on the joint wave-function of a pair of electrons. To illustrate the effect, following loosely arguments in *Solid State Physics* [44] and *Quantum Physics* [45], consider two electrons, labelled $i = 1$ and $i = 2$, occupying two spatial states $|\psi_i\rangle$ and $|\phi_i\rangle$, which are similar, atomic-orbital-like states, centred on two neighbouring atomic sites, in a solid, and which also have possible spin states $|\uparrow_i\rangle$ and $|\downarrow_i\rangle$. It is a requirement of quantum mechanics that the two electrons are indistinguishable from one another; therefore, their joint spatial state cannot be a simple state such as $|\psi_1\rangle |\phi_2\rangle$, which would identify a particular electron as being on each atomic site. To fulfil the indistinguishableness requirement, the state must be such that the only effect of exchanging the particle labels is to introduce a uniform phase shift in the wave-function, i.e. the joint spatial state must be $\frac{1}{\sqrt{2}}(|\psi_1\rangle |\phi_2\rangle + \exp(i\theta_A)|\psi_2\rangle |\phi_1\rangle)$, where θ_A is the uniform phase shift in question. Similarly, indistinguishableness limits the joint spin states to $|\uparrow_1\rangle |\uparrow_2\rangle$,

$|\downarrow_1\rangle |\downarrow_2\rangle$, or $\frac{1}{\sqrt{2}}(|\uparrow_1\rangle |\downarrow_2\rangle + \exp(i\theta_B)|\uparrow_2\rangle |\downarrow_1\rangle)$, where θ_B is the uniform phase shift involved in particle exchange due to the spin part of the wave-function alone. Given that electrons are fermions, quantum mechanics, further, demands that the total phase shift on particle exchange, $\theta_A + \theta_B$, or simply θ_A , where no θ_B is involved in the spin wave-function, is π . One can identify the concept of the two electrons' spins being parallel with the spin states where no θ_B is involved, or where $\theta_B = 0$; therefore, when the electrons' spins are parallel, $\theta_A = \pi$, and the joint spatial state is $\frac{1}{\sqrt{2}}(|\psi_1\rangle |\phi_2\rangle - |\psi_2\rangle |\phi_1\rangle)$; this is an odd function of the spatial displacement between the two electrons, and must, therefore, vanish when this displacement is zero, prohibiting the two electrons from being spatially coincident and, providing that the wave-function varies smoothly with this displacement, rendering the probability of them being very close together low. Given that there is an electrostatic repulsion between the electrons, this is a low-energy state. Similarly, one can identify the concept of the two electrons' spins being anti-parallel with the $\theta_B = \pi$ spin state, giving a joint spatial state $\frac{1}{\sqrt{2}}(|\psi_1\rangle |\phi_2\rangle + |\psi_2\rangle |\phi_1\rangle)$; this even function of the displacement between the two electrons does not prevent the electrons from being very close together, or even spatially coincident; their electrostatic repulsion, therefore, renders it a high-energy state. To summarize, the state in which the electrons' spins are anti-parallel has a higher energy, by some amount ΔV , than the state in which their spins are parallel; it is as if each electron's spin generates a magnetic flux density $B = \frac{m_e \Delta V}{eh}$, acting on the spin magnetic moment of the other electron. The Weiss field is this effective magnetic flux density, produced by quantum-mechanical symmetry considerations, scaled up to a situation where an electron interacts not just with one other electron, but with the whole population of other electrons in a solid. I expect the Weiss field, not the genuine magnetic flux density, to be the effect detected with the reflected electron beam, because the Weiss field in transition metals is [44] roughly a factor of 100 larger than the genuine magnetic flux density in the remnant state; however, some caution about this expectation is in order, because, as is clear from the argument above, the spatial states of the electrons are crucial in producing the Weiss field, and the spatial states of the unbound electrons being reflected are very similar neither to the single-site atomic orbitals described above, nor to the states of the transition metals' $3d$ electrons, for which the factor of 100 is known to hold good.

It will be noted that, in the model, both the electrostatic potential and the Weiss field are taken to be laterally homogeneous, i.e. not to vary with position in the plane of the film; this gives the appearance of being a rather strong assumption about the configuration of the magnetic film structure be-

ing studied. In particular, it gives the appearance of an implicit assumption of single-domain magnetization; this is an assumption that has been made in other workers' [46, 47, 41, 42] explanations of the behaviour of *Co/Cu*(001) film structures, and which has [39] some justification from Brillouin light scattering experiments; it is (section 2.9) also supported by magneto-optical Kerr effect measurements. In reality, the use of laterally homogeneous models does not imply any assumption about the configuration of the film structure or its domain structure; this study is concerned with the specular reflection, which is the scattered beam, the in-plane component of whose wave-vector is the same as the in-plane component of wave-vector of the incident beam. In the general theory of scattering of matter waves by a potential, a scattered beam whose in-plane wave-vector component differs from that of the incident beam by \mathbf{k} results from the Fourier component of the scattering potential with in-plane wave-vector \mathbf{k} : specifically, the specularly reflected beam results from the average value of the potential, over the area of the sample covered by the incident beam, and is unaffected by variations in the scattering potential, such as domain structure, which are encoded in the Fourier components of the scattering potential with non-zero in-plane wave vectors, the effects of which appear only in the diffraction orders. Of course, if there are domains of varying magnetization directions, within the region illuminated by the incident beam, then the average Weiss field detected by polarized electron reflection will be smaller than the saturation Weiss field within a single domain, but the situation is still within the capability of this theory to handle.

Next, I need to discover the amplitude reflection coefficient, for a pure, coherent, electron wave, at a single step (figure 2.3.) The incident and transmitted electron waves are modelled as plane waves, with well-defined wave-vector components p in the plane of the interface, and q_i perpendicular to the interface. p must be the same for all the waves, in order to satisfy the boundary condition of continuity of the wave-function at the interface. Strictly, the eigen-states of a Hamiltonian which includes a magnetic field are not plane waves; more about this later (section 2.5.) The amplitude reflection coefficient is [30] this:

$$r_{01} = \frac{q_0 - q_1}{q_0 + q_1}, \quad (2.1)$$

or, for a general interface, this one:

$$r_{ij} = \frac{q_i - q_j}{q_i + q_j}. \quad (2.2)$$

Next, I need to build an expression for the energy of the electrons. There will be kinetic energy terms, along with an electrostatic potential energy, and

a term due to the torque, on the electron magnetic moment, in a magnetic field [30]. The form used for this last term assumes a well-defined energy for all directions of the electron spin. Strictly, only certain spin directions are eigen-states of a Hamiltonian that includes a magnetic field; more about this later (section 2.5.) This leads to this expression

$$q_i = \left(\frac{2m_e E \cos^2 I}{\hbar^2} \right)^{1/2} (1 + x_i)^{1/2}, \quad (2.3)$$

for the perpendicular wave-vector component, where I represents an angle of incidence, and the potential energy terms are represented by these dimensionless numbers:

$$x_i = y_i + z_i \cos S_i, \quad (2.4)$$

$$y_i = \frac{eV_i}{E \cos^2 I}, \quad (2.5)$$

$$z_i = -\frac{e\hbar B_i}{2m_e E \cos^2 I}; \quad (2.6)$$

S_i is the angle between the electron spin direction and the magnetic flux density in region i , and E_b is the total energy of the incident electrons, and therefore, by conservation of energy, of all the electrons.

I now use a binomial expansion [48] for the case where the potential energy terms are much smaller than the total electron energy, where the dimensionless numbers I've just devised are small. The magnetic term associated with the Weiss field in a ferromagnet is [43] a few tenths of an electron-volt, and the electrostatic contact potentials in the metals which I study will [49, 50] not be more than a few volts, whereas, in my experimental set-up, the incident electron energies range from a few hundred to a few thousand electron volts, so this approximation seems reasonable. With this expansion, the amplitude reflection coefficient is this:

$$r_{ij} = \frac{1}{4}x_i - \frac{1}{4}x_j - \frac{1}{8}x_i^2 - \frac{1}{8}x_i x_j + \frac{1}{8}x_j^2 + O(\{x_i, x_j\}^3). \quad (2.7)$$

2.3 A New, Classical-Field Theory of Polarized Electron Reflection: Reflection of an Unpolarized Beam from the Surface of a Bulk Magnetic Sample

An unpolarized incident electron beam is [31, 32] an incoherent superposition of pure states representing all directions of the incident spin. The polarization of the reflected beam from any surface is, therefore, given by an average

of the polarization over all polarization directions, weighted according to the intensity reflection coefficient for each polarization. This incoherent averaging process (section 2.12.2) gives this reflected polarization from a bulk surface (figure 2.2)

$$\begin{aligned} P &= \frac{2y_1 z_1}{3y_1^2 + z_1^2} + O(\{y_1, z_1\}) \\ &= -\frac{4e^2 \hbar m_e V_1 B_1}{12e^2 m_e^2 V_1^2 + e^2 \hbar^2 B_1^2} + O(\{y_1, z_1\}). \end{aligned} \quad (2.8)$$

Both the term given explicitly, and the next term in the binomial expansion, are in the direction of the magnetic flux density in the bulk material. The polarization, predicted by this equation, is shown as a function of Weiss field B , for a fixed electrostatic potential $V = -0.9$ V, in figure 2.4.

The most salient qualitative feature of this polarization formula is that, at high incident electron energies, the reflected polarization is dominated by a non-zero term, which is independent of the incident electron energy, and controlled by the balance between the electrostatic potential and the magnetic flux density, in the sample. This polarization can be as large as $\frac{1}{\sqrt{3}}$ in either direction.

2.4 A New, Classical-Field Theory of Polarized Electron Reflection: Multi-Layer Structures

I propose the extension of this analysis to magnetic multi-layer structures, by using the theory of Fabry-Perot etalons, as is [28, 29] already the practice in PNR. There are infinitely many possible paths for reflection from a multi-layer structure, indexed by how many times the electron wave “bounces” within each layer. In the diagram (figure 2.5,) we can see paths with no bounces, with one bounce, and with two bounces. For a given, pure incident wave, the reflected waves from the various paths are superposed coherently to build the reflected wave, each term in the coherent superposition including an amplitude factor due to the amplitude reflection or transmission coefficient at each interface which it has encountered, and a phase factor due to the path length which it has traversed in the magnetic layers. This will result in a spin-dependent amplitude reflection coefficient for the whole multi-layer system, which will provide the weightings to go into the incoherent superposition over an unpolarized incident beam. This incoherent superposition, as for the

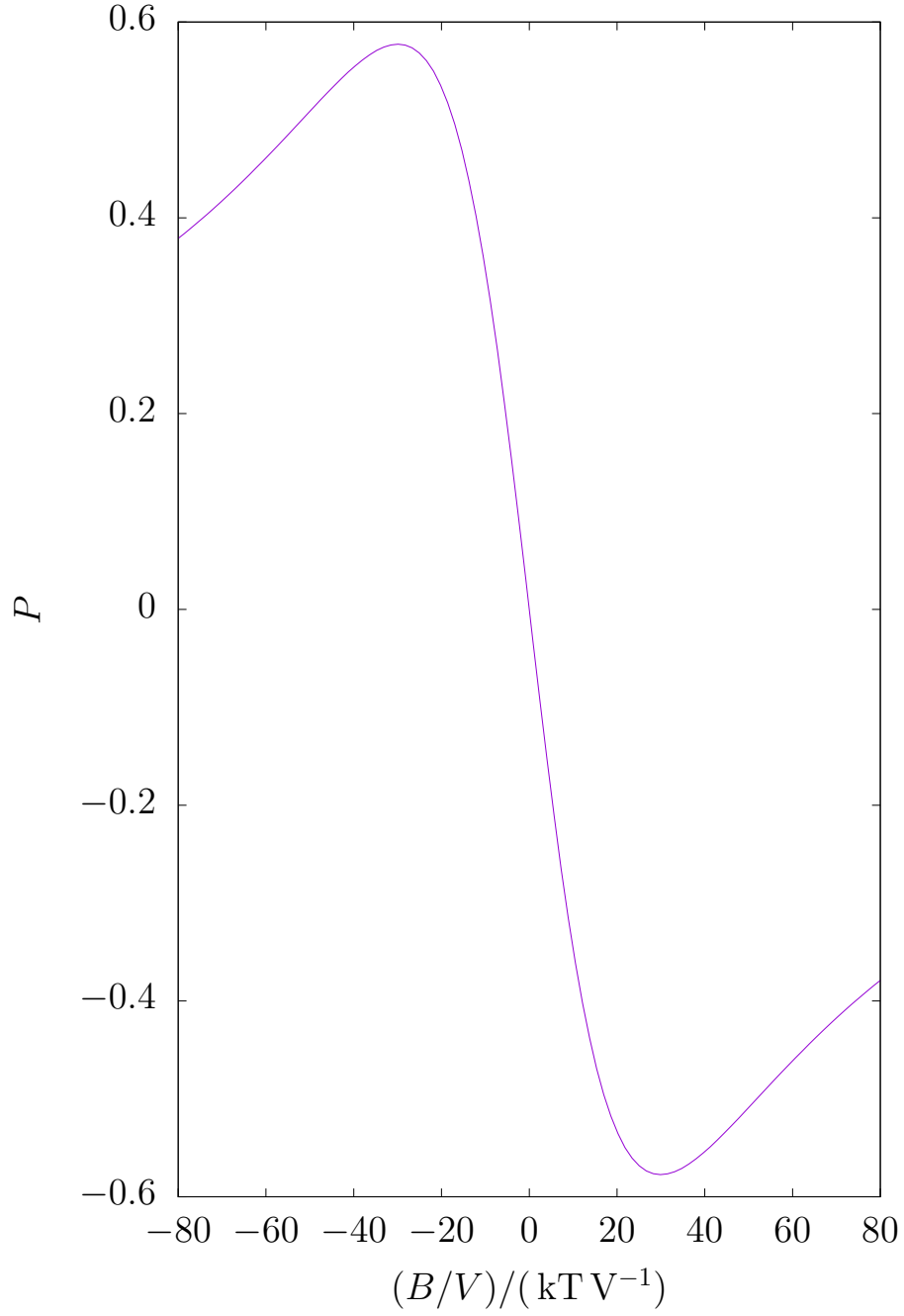


Figure 2.4: Predicted Reflected Beam Polarization against the Ratio of Weiss Field to Electric Potential, in the Sample

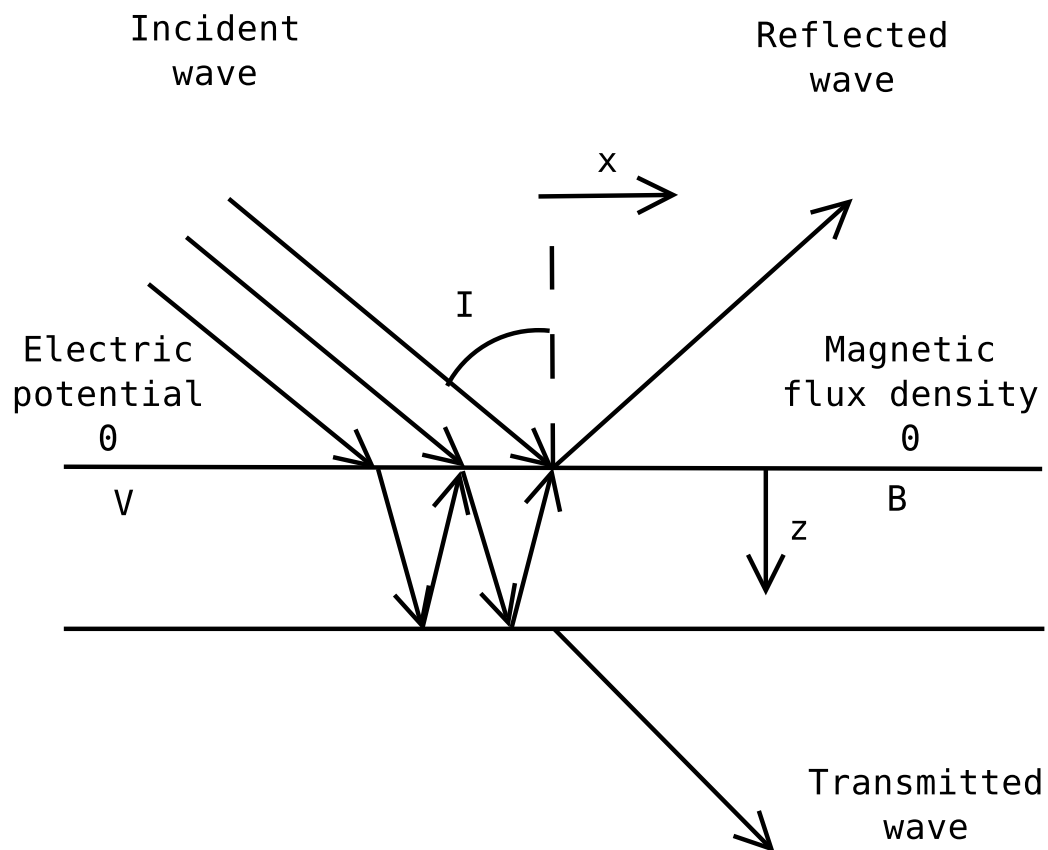


Figure 2.5: Reflection Paths for an Electron Wave in a Single Magnetic Layer

bulk sample, will give the reflected polarization. I expect working through the maths for this to be trivial, but time-consuming.

2.5 A New, Classical-Field Theory of Polarized Electron Reflection: Comments on This Analysis

There follow comments on some assumptions in this analysis. Firstly, there is the matter of modelling the electrons as a plane wave. This is equivalent to neglecting the deflection of the electrons by the Lorentz force, which means taking the limit of weak magnetic fields; this limit has, in any case, been taken in the binomial expansion. The same convention, of neglecting this deflection, was adopted by Weber et al. [51], when they analysed the spin polarization of transmitted electron waves.

Secondly, there is the issue of assuming that all electron spin directions are eigen-states of the Hamiltonian. In this, I depart from the tradition of analysis of PNR, where matrices are [28, 29] used to represent the Zeeman energy, and the reflection coefficient, without any need for this approximation. I also depart from the work of Weber et al. [51] on electron transmission: they regard the Larmor precession, which is a manifestation of the fact that not all spin directions are eigen-states of the Hamiltonian in a magnetic field, as crucial in determining the transmitted polarization. I propose the production of a more “first-principles” model, which will use the matrix representation of the reflection coefficients, and therefore capture the Larmor precession, and other spin-flip scattering effects. However, this model is not proposed as a replacement for the one presented here, but as a complement to it. What I suggest is to subject both models, along with a third, completely classical, reflection model (section 2.7,) to experimental data, and use the well-established [52] methods of Bayesian statistics, first to infer the parameters of magnetic flux density, electric potential, and layer thickness, for each model, then to judge the relative confidence that can be placed in each model.

One reason for not simply abandoning all but the most “first-principles” of the models is given by Anderson [53], who points out that any system, more complicated than a molecule of approximately four atoms, is almost never in an eigen-state of its Hamiltonian, with the result that the Schrödinger equation does not describe the state of the system. This is because the tunnelling-like processes, which would otherwise collapse the system into an eigen-state of its Hamiltonian, are very slow for complicated systems: often

very slow compared with the age of the universe, and certainly very slow compared with the rate of occurrence of measurement-like interactions with the outside world, which collapse the system into eigen-states of operators other than the Hamiltonian. Therefore, it can't be guaranteed that the model that implements a Schrödinger equation with the most realistic Hamiltonian will always be the most useful, in describing the real behaviour of the system.

In addition, I have devised a very different argument [10] for not always preferring the most first-principles model.

Thirdly, it is worthwhile to comment on the effect on the polarization of transmitted waves, due to spin-dependent loss of electrons to inelastic processes, which was noted by Weber et al. [51]. At first glance, the classical-field analysis above appears to be entirely elastic. However, it is capable of assimilating the effect of these processes, which would appear as imaginary parts in the electric potential and magnetic flux density.

2.6 A New, Classical-Field Theory of Polarized Electron Reflection: Conclusions

- The spin polarization of the reflected electron beam from a bulk magnetic surface, in the model described, is this:

$$\mathbf{P} = -\frac{4e^2\hbar m_e V_1 \mathbf{B}_1}{12e^2 m_e^2 V_1^2 + e^2 \hbar^2 B_1^2} + O(\{y_1, z_1\}). \quad (2.9)$$

- The rate of electrons leaving the sample, in the reflected beam (figure 3.1,) is, from integration of equation 2.26,

$$G = \left(\frac{e^2 V^2}{16E_b^2 \cos^4 I} + \frac{e^2 \hbar^2 B^2}{192m_e^2 E_b^2 \cos^4 I} \right) \frac{F}{e}, \quad (2.10)$$

where $\frac{F}{e}$ is the rate of electrons arriving at the sample, in the incident beam.

- The extension of the model to multi-layer systems is likely to be a trivial, but time-consuming, mathematical task.
- Two other, similar models are suggested, one of which differs from this by the use of a more “first-principles” treatment of the Zeeman energy, and the other, discussed in section 2.7, by a fully classical treatment of the reflection process, and

- there is a strong case for retaining all three models, and using Bayesian statistics to compare them in the light of experimental data, rather than discarding all but the most “first-principles” model.

Other workers have obtained theoretical predictions for reflected electron beam polarizations, from magnetic and non-magnetic surfaces. In chapter 2, several of these were discussed, and compared and contrasted with the theory of this chapter.

Before moving on to a completely classical version of this theory, an aside is in order, on the angle-dependence of the intensity G in this theory, which has a fascinating $\frac{1}{\cos^4 I}$ form, in terms of the angle of incidence I . I have access to measurements, of the currents¹ H_1 and H_2 arriving at the Mott polarimeter’s two channeltrons after reflection, as a function of the angle θ , by which the sample is rotated about the scattering plane normal, starting from an arbitrary (but permanently marked) origin, made in conjunction with colleagues at the Cavendish Laboratory, which I supposed may help to demonstrate this form. The incident electron beam energy and current, the potentials at the polarimeter electrodes, and the translational position of the sample were held constant throughout.

The original purpose of making these measurements was to find the θ value, equivalent to $I = \frac{\pi}{4}$, for which the centre of the reflected beam struck the centre of the polarimeter’s entrance hole. This value of θ was expected to maximize H_1 and H_2 . The details of the functional forms of H_1 and H_2 away from this maximum are unknown, but a sensible guess is a Gaussian,

$$H_i = H_i^{(0)} \exp \left(-\frac{M^2}{2\sigma_i^2} \right) + D_i, \quad (2.11)$$

of which $H_i^{(0)}$, σ_i and D_i are adjustable parameters representing the height and width of the maximum, and any additive systematic error in the ammeter, respectively. M is the distance, measured perpendicular to the ray direction of the reflected beam, by which the centre of the reflected beam misses the centre of the polarimeter’s entrance hole. $M \propto \tan \left(I - \frac{\pi}{4} \right)$, so

$$\begin{aligned} H_i &= H_i^{(0)} \exp \left(-\frac{\tan^2 \left(I - \frac{\pi}{4} \right)}{2w_i^2} \right) + D_i \\ &= H_i^{(0)} \exp \left(-\frac{\tan^2 \left(\theta_i^{(0)} - \theta - \frac{\pi}{4} \right)}{2w_i^2} \right) + D_i, \end{aligned} \quad (2.12)$$

¹Strictly, being composed of electrons, these currents are negative, but they are here presented as positive, for greater ease of discussion; all the theoretical analysis has a sign convention to match this.

where w_i is a re-scaled version of the width parameter σ_i , $\theta_i^{(0)}$ is another adjustable parameter, representing the arbitrary origin of the angle measurements, and the sign convention is representative of the fact that the angles are measured in such a way that increasing θ reduces I . This is how one might expect the system to behave, if the reflection coefficient is independent of the angle of incidence.

If, on the other hand, the reflection coefficient depends on the angle of incidence, in the way predicted by the theory presented above, one obtains

$$H_i = \frac{H_i^{(0)} \exp \left(-\frac{\tan^2 \left(\theta_i^{(0)} - \theta - \frac{\pi}{4} \right)}{2w_i^2} \right)}{\cos^4(\theta_i^{(0)} - \theta)} + D_i. \quad (2.13)$$

In figures 2.6 and 2.7, the experimental data are presented, along with best-fit versions, obtained by a least-squares method, of both theories.

The predictions of the two models are almost indistinguishable from one another, and both are, therefore, about equally good fits to the experimental data. This is because the function $\frac{1}{\cos^4 I}$ is characterized by sharp singularities at the most extreme possible angles of incidence, the grazing incidence angles $I = -\frac{\pi}{2}$ and $I = \frac{\pi}{2}$, with a broad, flat intervening region. Within this flat region where the experiments were undertaken, the classical-field theory's reflection coefficient is, to a very good approximation, independent of angle of incidence; therefore, it is unsurprising that the predictions are indistinguishable from those of a model with a reflection coefficient exactly independent of angle of incidence. There would be little point in attempting to extend the experiment into the grazing angles of incidence, because, in this region, the component of the electron motion perpendicular to the sample surface is tiny, nullifying the classical-field theory's fundamental assumption that the kinetic energy associated with this component of the electron motion is much larger than the potential energy step at the surface. This also absolves us of the need to worry about the "un-physical" singularities; they are, in any case, outside the domain of validity of the theory.

The aside over, it is time to turn to a fully classical theory of polarized electron reflection.

2.7 A Completely Classical Polarized Electron Reflection Theory

Above, (section 2.6,) I suggested that it might be enlightening to develop a completely classical theory of polarized electron reflection; this will be done

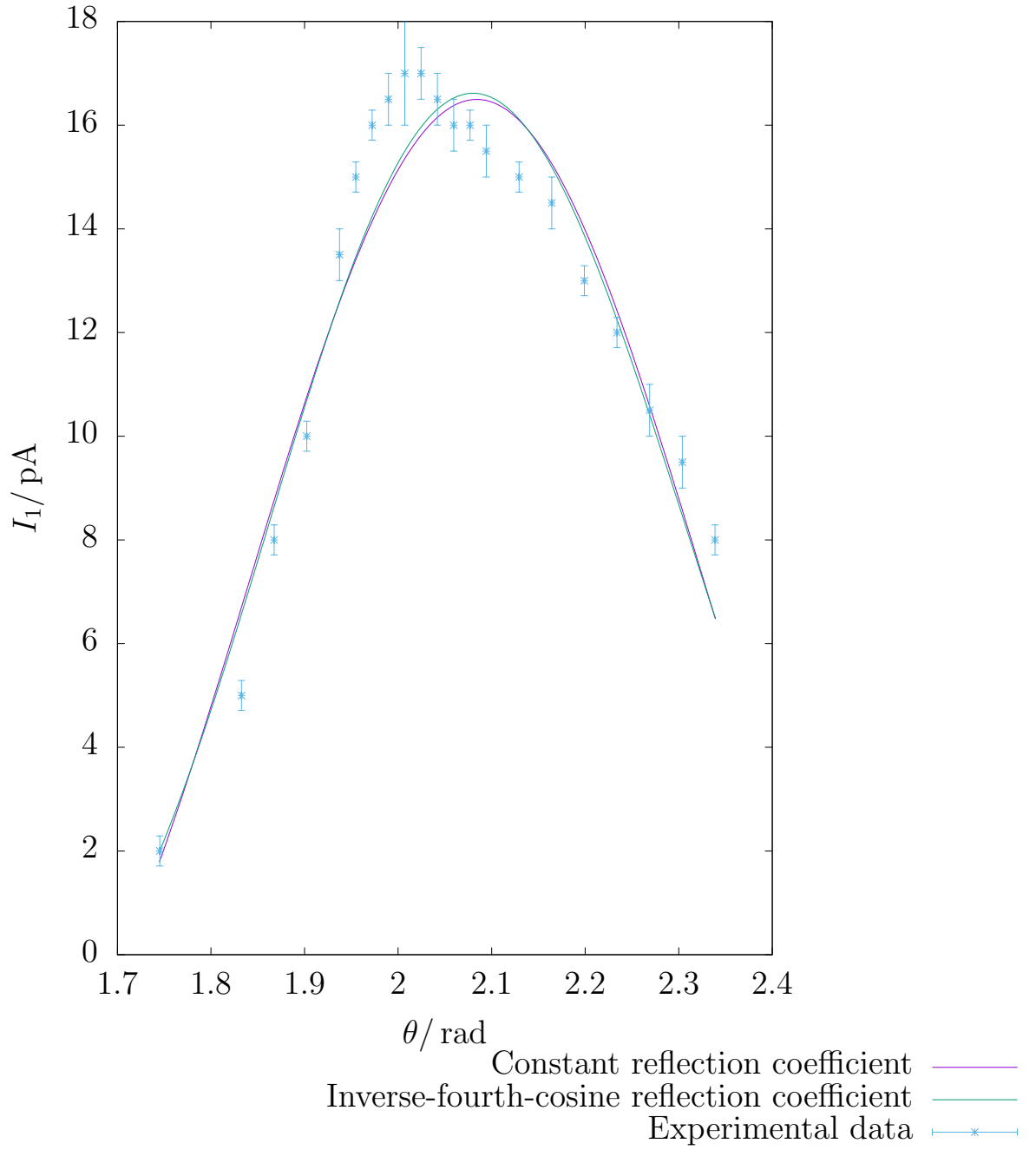


Figure 2.6: Current Arriving at Channeltron 1, against Rotation Angle of Sample; Points with Error Bars Show Experimental Results, and Lines Show the Predictions of Best-Fit Versions of Two Models, One with a Reflection Coefficient Independent of Angle of Incidence I , and One with a Reflection Coefficient Proportional to $\frac{1}{\cos^4 I}$.

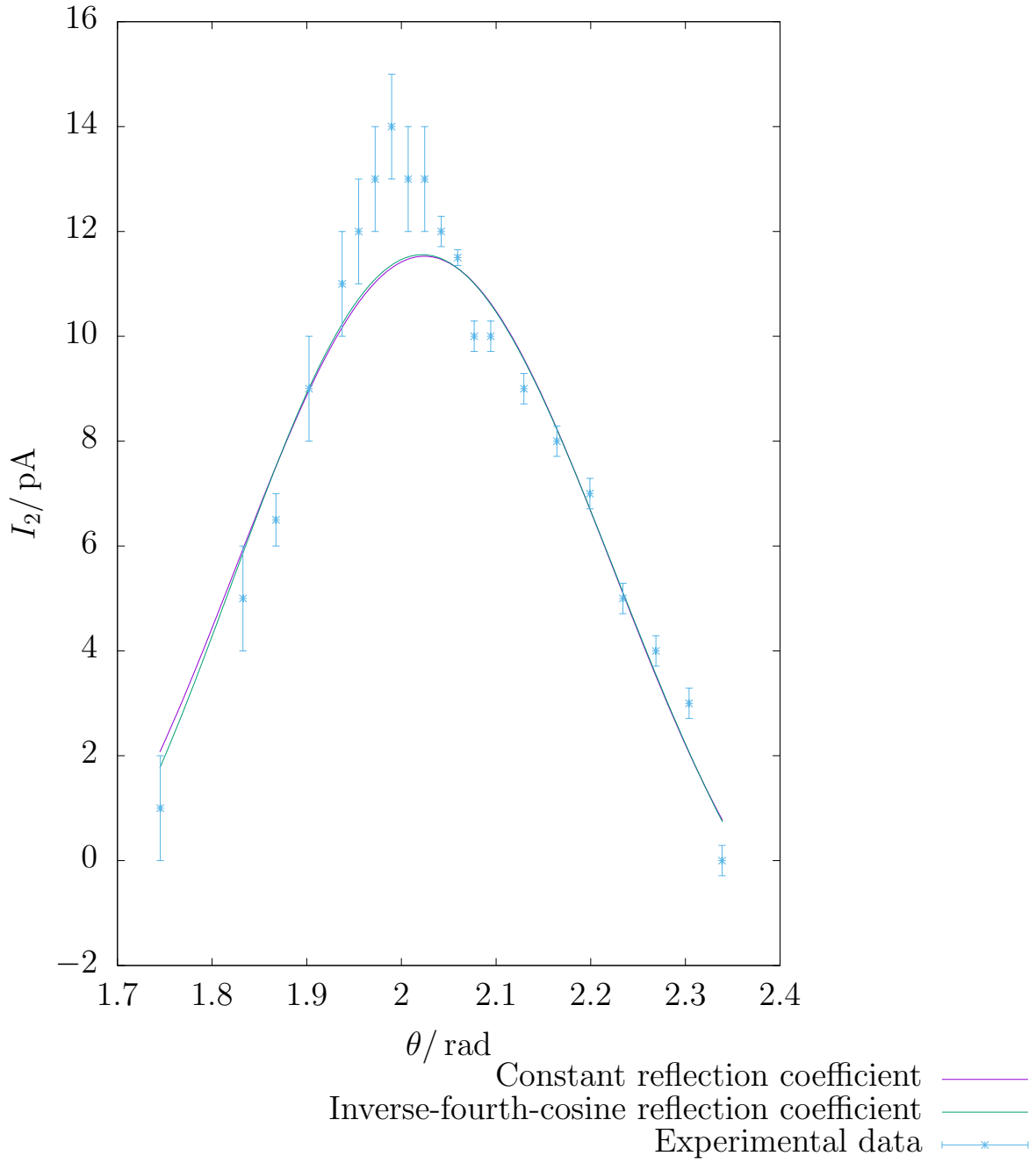


Figure 2.7: Current Arriving at Channeltron 2, against Rotation Angle of Sample; Points with Error Bars Show Experimental Results, and Lines Show the Predictions of Best-Fit Versions of Two Models, One with a Reflection Coefficient Independent of Angle of Incidence I , and One with a Reflection Coefficient Proportional to $\frac{1}{\cos^4 I}$.

in this section. The classical condition for reflection from a bulk sample is rather simple. In terms of the dimensionless numbers defined in equations 2.4, 2.5, and 2.6, an electron is reflected if

$$x_1 \geq 1, \quad (2.14)$$

and is not reflected if

$$x_1 < 1. \quad (2.15)$$

This thesis is (section 2.2) concerned with circumstances where $|x_1| \ll 1$. In this case, classical theory predicts a zero intensity reflection coefficient. Therefore, the measured reflections presented in chapter 5, and those reviewed in section 2.10, are purely quantum effects.

This does not imply that the classical theory is of no interest; an important test of the plausibility of the quantum theory presented earlier in this chapter is its obedience to Ehrenfest's theorem, which states [45] that, when the wave-function varies in space much more rapidly than the potential, the predictions of classical mechanics and quantum mechanics are the same.

In this case, the potential includes a step. Therefore, the wave-function varies in space much more rapidly than the potential only as the energy of the incident electrons tends to infinity. In this case, both classical theory, and the quantum theory presented earlier in this chapter, predict a zero reflection coefficient, and Ehrenfest's theorem is obeyed.

2.8 Motivation for Experiments

Above, some theoretical perspectives have been presented, on polarized electron reflection measurements of magnetic materials. This section details the motivation for undertaking the polarized electron reflection measurements on a *Co/Cu*(001) structure, described in part III.

Colleagues at the Cavendish Laboratory had earlier performed a series of measurements on the system formed by growing a 0.5 ML *Mn*/6 ML *Co/Cu*(001) multi-layer [14, 15, 16]. Low-energy electron diffraction (LEED) revealed, through the existence of $(\frac{1}{2}\frac{1}{2})$ order spots, a $c(2 \times 2)$ (chessboard-like) superstructure in the plane of the film.

Three possible explanations were advanced for the $c(2 \times 2)$ superstructure [14, 15, 16]:

- Inter-diffusion of copper atoms through the cobalt layer may have led to the formation of a *MnCu* surface alloy [17, 18]. However, these experiments were performed at room temperature, which is too cold to

permit significant inter-diffusion through 6ML *Co* [19]. This suggestion was therefore ruled out.

- The manganese may have had an internal $c(2 \times 2)$ anti-ferromagnetic configuration. However, the measured $(\frac{1}{2} \frac{1}{2})$ spot intensity was ~ 10 times that predicted for magnetic diffraction of this type by Tamura et al. [20]. This phenomenon is therefore incapable of providing a complete explanation of the observed superstructure.
- An ordered *MnCo* surface alloy may have been formed. Given the evidence against the other two models, the observed diffraction pattern was attributed to *MnCo* alloy formation.

Magneto-optical Kerr effect (MOKE) measurements were taken by colleagues at the Cavendish Laboratory as part of the same project [14, 15, 16]. The [110] direction Kerr signal was seen to increase with the addition of manganese, in the regime where the alloy exists. The immediate reaction to this is that the system's magnetic moment is increasing, i.e. that the manganese atoms that are being added are ferro-magnetically aligned, both with each other and with the cobalt. However, the simultaneous drop in [100] Kerr signal did not paint the same picture, and it may be that a change in magneto-optical response, rather than a genuine addition of magnetic moments, is responsible for the increased [110] signal. The possibilities are in particular need of investigation, given that a series [21, 22, 23] of numerical calculations, using different approximations, have produced widely differing predictions about the magnetic properties of this system.

The polarization of a reflected electron beam from the sample surface provides an alternative to MOKE, for measuring the magnetization, through the difference, for the two electron spins, in density of states at a particular energy created by the exchange splitting, and as such provides an experiment which is interesting by virtue of having an unpredictable result. The experiments presented in this thesis, using a *Co/Cu*(001) structure, are intended as an intermediate stage on the way to similar measurements on *MnCo/Co/Cu*(001), although they could equally well lead to similar measurements on other multi-layer structures of more direct industrial relevance, such as metal/ferromagnet or semiconductor/ferromagnet spin valves. This possibility may help to address the conclusions, concerning the motivation for experimental research projects, of statistical research the author has presented elsewhere [10].

In addition, the measurements for *Co/Cu*(001), in themselves, allow a trial run of estimating the parameters in the new theory of this chapter, and comparing a version of that theory, in which no Weiss field affects the probing

electrons, against another version, in which an adjustable Weiss field affects the probing electrons. This task is undertaken in section 5.3.

$Co/Cu(001)$ is a much-studied system. Before discussing previously published experimental polarized electron reflection results, and presenting the new, polarized electron reflection experiment, which is at the heart of this thesis, it will be as well to review other workers' published results on the structure and magnetic properties of this system.

2.9 Review of Published Information on the Structure and Magnetic Properties of $Co/Cu(001)$

Although bulk cobalt is [54] a hexagonal close packed metal at room temperature and pressure, thin cobalt films, grown by molecular beam epitaxy on $Cu(001)$, adopt [55, 56, 46] the face-centred cubic structure of the copper; this epitaxial structure requires [57] some elastic strain in the cobalt, and breaks down [57, 42] for large thicknesses², as it becomes energetically favourable to form dislocations to relieve the strain; the boundary of “large thicknesses” is [40] not thinner than 10 ML, and has been found [57] to vary between 10 ML and 20 ML, depending on the temperature at which the film is deposited, although, at room temperature, substantial strain remains [57] up to at least 40 ML, and the method used to measure the lattice parameter, and therefore the strain, [57] suggests that the cobalt remains face-centred cubic throughout; therefore, one would expect all but the thinnest of the Co films studied in this thesis, and possibly the thinnest one as well, to be in the régime where epitaxial growth has begun to break down, in the sense of the lattice parameter departing from that of copper. For thicknesses greater than 1 ML [38, 55, 46] or 2 ML [40, 47, 41, 42], and less than 10 ML [55], the cobalt wets [38, 55, 56, 40, 46, 47, 41, 42] the surface, growing layer-by-layer, although this is not [46] the case for (1 1 17) mis-cut substrates. The surface roughness of the cobalt film, therefore, oscillates [47] as a function of film thickness, with period 1 ML.

Thin cobalt films on copper (001) have a ferro-magnetic phase, for (relatively) large thicknesses; the transition thickness d_C has been variously reported as being 1.75 ML at room temperature [38], as having a lower limit of 0.7 ML and an upper limit of (0.96 ± 0.1) ML [55], as being (1.6 ± 0.3) ML at

²In this section, the common convention of giving thicknesses in mono-layers is followed, whereas elsewhere in this thesis, thicknesses are given in units related to the metre. From comments in “Magnetic Anisotropies of Ultrathin $Co(001)$ Films on $Cu(001)$ ” [39], one can calculate that, for $Co/Cu(001)$, 1 ML = (166 ± 36) pm, whereas other workers [47, 58, 57] state that 1 ML \approx 180 pm.

room temperature [39]. as being (1.3 ± 0.3) ML [59], as being approximately 1.5 ML [47], as being (1.35 ± 0.35) ML [41], and as having a lower limit of 1 ML and an upper limit of 1.7 ML [60]. Where the films are thin enough to be regarded as two-dimensional, the ferro-magnetism cannot [39] be rendered stable by the Weiss field alone, and some other effect, perhaps due to dipole-dipole interactions or magnetic anisotropy, must [39] be invoked to explain the ferro-magnetism. For thicknesses slightly greater than the critical thickness, the Curie temperature is [38] much lower than that for bulk cobalt, and exhibits [38] a strong dependence on the film thickness, varying [38] approximately linearly from 125 K at 1.5 ML thickness to 575 K at 3 ML thickness, compared with a bulk Curie temperature reported as 1388 K [38] or 1392 K [61]; imperfections in the film can [38] further suppress the Curie temperature. The magnetic susceptibility as a function of thickness obeys [42] a power law consistent with ferro-magnetism arising through a two-dimensional percolation transition; that is to say, the susceptibility χ , for thicknesses $d < d_C$, is [59] proportional to $\left(1 - \frac{d}{d_C}\right)^{-\gamma}$: two separate experiments found [59] $\gamma = 2.41 \pm 0.07$ and $\gamma = 2.38 \pm 0.07$, which are [59] consistent with the theoretical prediction of $\gamma = 2.389$, for a two-dimensional percolation phase transition, but rather less consistent with the prediction of $\gamma = 1.66$, for a three-dimensional percolation phase transition. A percolation phase transition occurs [59], as material (cobalt) is added, when the concentration of atoms becomes sufficient for the (short-range) exchange interaction to be transmitted throughout the sample.

The magnetic anisotropy energy of *Co/Cu*(001) films combines a uni-axial term, which includes [40] an important (but controversial [39]) contribution from epitaxial strain, and which constrains [38, 39, 40, 41, 42] the magnetization to be in the plane of the film, i.e. which renders in-plane magnetization energetically favourable by [39] $(920 \pm 180) \mu\text{J m}^{-2}$ of film surface area, with a term of fourfold symmetry within the plane, favouring [38, 40, 46, 47, 41] magnetization along $\langle 110 \rangle$ axes within the plane of the film, over magnetization along $\langle 100 \rangle$ axes within the plane of the film, by $(55 \pm 3.75) \text{ kJ m}^{-3}$ of cobalt volume, less $(15.5 \pm 1.5) \mu\text{J m}^{-2}$ of film surface area; however, the fact that the remnant magnetization along [110] is [41, 42] smaller than the saturation magnetization has been interpreted [47, 58, 41], on the assumption, which is [39] supported by Brillouin light scattering measurements, of single-domain magnetization during the reversal process (Stoner-Wohlfarth reversal,) along with other features [47] of the shape of the *M-H* loops, to mean that the overall easy axes of the film depart [46, 41] from $\langle 110 \rangle$ due to an additional term, of twofold symmetry within the plane of the film; this departure has [46, 47, 41, 42] been attributed to the effect of atomic

steps on the *Co* surfaces, inherited from the pre-deposition *Cu* surface³; the 1 ML-period oscillation in the surface roughness, as a function of film thickness, is [47, 57, 42] matched by an oscillation of the same period in this twofold-symmetric anisotropy within the plane, as revealed [47] by the variation of the coercive field with thickness; the oscillation of the coercive field with thickness is [47] superimposed on a general increase in coercive field with increasing thickness, which undergoes [47] a sudden change of slope at thickness 2 ML. However, other workers [39] have questioned the existence of the twofold-symmetric anisotropy within the plane. Any corresponding oscillation in the fourfold-symmetric anisotropy within the plane is [47] smaller than 5% of the average anisotropy. Others [38] have also noted modification of the coercivity and other features of the in-plane anisotropy, due to imperfections of the film. However, the possibility has also been acknowledged [42] that the step edges suppress the remnant magnetization along [110] not by altering the film's magnetic anisotropy, but by acting as domain-wall pinning sites, in a multi-domain structure, and scanning tunnelling microscopy has revealed a surface topography around the steps, whose shape anisotropy is [47] not sufficient, of itself, to explain the observed anisotropy oscillations, requiring the invocation of either lattice distortion at the step edges and magnetostriction, or anisotropic diffusion of cobalt atoms at the steps; the former is [47, 57] supported by electron diffraction measurements. It could [47, 58], alternatively, be that the oscillation of magnetic anisotropy with thickness results from an oscillation, with thickness, in the spin-orbit interactions of the discrete states, forced on electrons by confinement in a square potential well, formed by the cobalt film's lower and upper surfaces; however, unlike the surface-topography-based explanation, there is [47] no independent evidence that this spin-orbit coupling varies with the same, 1 ML, period as the magnetic anisotropy. As film thickness is reduced to very small values, the magnetic anisotropy vanishes [39], at the same thickness where the film ceases to be ferro-magnetic, supporting the idea that it is magnetic anisotropy that stabilizes the ferro-magnetic state. There is [42] also a change in magnetic anisotropy when the epitaxial structure starts to break down at large thicknesses; to be more specific, when the epitaxial strain starts to be relieved with increasing thickness, at [57] ~ 16 ML, the easy axes of the twofold-symmetric, in-plane anisotropy suddenly rotate [57] through ninety degrees, and its magnitude sharply increases [57], while, simultaneously, the magnitude of the coercive field sharply increases [57], although this has been

³It is important to distinguish between this residual roughness of an annealed substrate surface, and the much greater roughness of as-sputtered substrates, which has been cited [38] as responsible for un-reproducible magnetic properties in epitaxial films.

interpreted [57] as the effect of dislocations acting as domain wall pinning sites, in a multi-domain structure, rather than as a corresponding, sharp increase in the magnitude of the fourfold-symmetric, in-plane anisotropy. The amplitude of the magnetic anisotropy energy is manifested in the coercive field, which has been given [39] as $(6.4 \pm 1.1) \text{ kA m}^{-1}$; this depends [38, 42, 60] on temperature, in a way which is attributed [38, 42, 60] to diffusion of copper atoms through the cobalt film at elevated temperatures. The twofold-symmetric anisotropy within the plane can [47] also be altered by growing the film in an applied magnetic field.

The saturation magnetizations of *Co/Cu*(001) films, of all thicknesses where the films are ferro-magnetic, are [39, 57] within 5% of the 1.424 MA m^{-1} [39, 57] saturation magnetization of bulk cobalt. The saturation magnetization increases [47] with increasing film thickness.

It will be enlightening to recapitulate what this literature review has revealed about two key questions. Firstly, are the relatively thick (between $(2.57 \pm 0.36) \text{ nm}$ and $(17.1 \pm 2.4) \text{ nm}$, i.e. between $\sim 15 \text{ ML}$ and $\sim 100 \text{ ML}$) cobalt films used for the new experimental study, presented in this thesis, really epitaxial? The literature [57] reveals that only the thinnest one of these seven films has the possibility of being perfectly epitaxial, in the sense of adopting both the face-centred cubic structure of the copper substrate and the copper lattice parameter; the same paper reveals that the one further film with a thickness below 40 ML (6.6 nm) will still be epitaxial in the sense of having a face-centred cubic structure, but will have a lattice parameter somewhere between the strain-free lattice parameters of copper and cobalt. The literature does not provide any direct information on the structure of the five thicker films, but the intuitive extrapolation is that the trend of remaining face-centred cubic, but having a lattice parameter that gradually approaches the strain-free lattice parameter of cobalt, will continue as the thickness increases beyond 40 ML. Certainly, all the low-energy electron diffraction patterns from *Co/Cu*(001), which the present author (sometimes alone, sometimes in conjunction with colleagues) has observed, have been characteristic of a face-centred cubic structure, but the thickest of the films we examined in this way was $(1.5 \pm 0.26) \text{ nm} \approx 9 \text{ ML}$, and therefore sheds little light on this discussion.

Secondly, what is the magnetic easy axis of the films? It seems [38, 39, 40, 41, 42] certain to be in-plane, but where within the plane? Other workers [46, 47, 58, 41, 42] have found the easy axis to depart from the $\langle 110 \rangle$ directions favoured by the fourfold-symmetric anisotropy, in a way that is controlled by the detailed surface topography of the substrate, and which, therefore, varies from sample to sample. The copper substrate crystal used in the experiments herein presented was the same one that was used in “Variations

in the magnetic properties of ultrathin *Co* films due to the adsorption of non-magnetic metal atoms at the *Co*/vacuum interface” [41], where the easy axis of the cobalt films was found to be [100]. For this reason, the sample was magnetized, and the reflected electron beam polarization measured, along [100], in the experiments herein presented. However, there is some cause for caution: the substrate crystal has been polished since the published results on its easy axis were obtained, and those published results were obtained at rather smaller cobalt thicknesses than those used herein, whereas it is [57, 42] possible for the easy axis direction to vary with thickness. Therefore, the most useful guide to the easy axis direction is likely to be provided by *B-H* loops for films in the relevant thickness range, measured using the magneto-optical Kerr effect (MOKE,) by one of the author’s colleagues, using a rig developed jointly by the author and colleagues, during a polarized electron reflection experiment (section 5.5,) conducted jointly by the author and the colleague in question. These loops are shown in figure 2.8. Two features of the loops for non-zero thicknesses are crucial. Firstly, the remnant magnetization along [100] is almost as large as the saturation magnetization, confirming both that there is a minimum of the magnetic anisotropy energy, with respect to magnetization direction, when the magnetization is along [100], and that the remnant state of the cobalt film is almost single-domain. Secondly, the magnetization appears to reverse all at once, rather than in multiple steps, suggesting that this energy minimum is the global minimum, i.e. [100] is *the* easy axis.

Having summarized the present state of knowledge concerning *Co/Cu*(001), it is time to review some published polarized electron reflection studies.

2.10 Other Workers’ Published Experimental Data on the Spin Polarization of Reflected Electron Beams

Although the author is familiar with several examples [1, 4, 62, 63, 64, 25, 65, 26, 55, 51] of published data, obtained using Mott polarimeters, on the spin polarization of reflected, diffracted, transmitted, inelastic, and secondary electron beams, from magnetic and non-magnetic materials, rather few of them [1, 4, 62, 55] concern specular reflection. Unfortunately, these include only one [55] of the publications, in which copper [25, 65, 26, 55] or cobalt [55, 51] samples are used. Nevertheless, other workers’ specular reflection experiments on metallic surfaces can be compared, at least qualitatively, with the new theory of this chapter, and with the published theories reviewed in

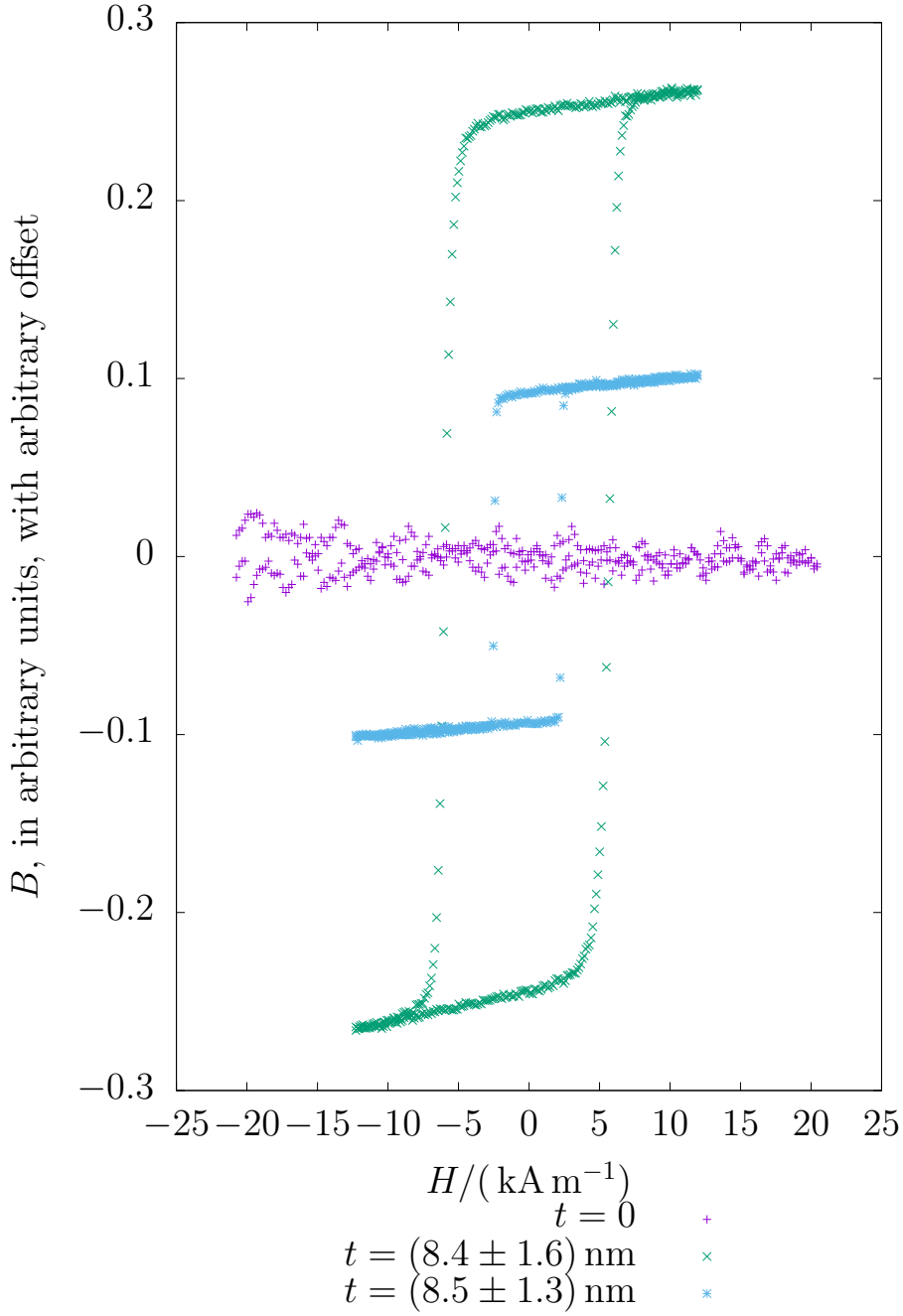


Figure 2.8: A Graph of the [100] Component of the Magnetic Flux Density B , Inside the Surface Layers of $\text{Co/Cu}(001)$ Samples, as Measured Using MOKE, against the [100]-Direction Applied Magnetic Field Strength H ; the Thickness of the Cobalt Layer in Any Individual Sample Is Denoted by t , and the Thicknesses Overlap with the Domain of Thicknesses Used for the Main Polarized Electron Reflection Experiments, Presented in this Thesis. These data have previously appeared in *Electron Spin Polarimetry Studies of Ultra-Thin Magnetic Films* [3].

this chapter.

Measurements of reflected beam polarization from a tungsten (001) surface, as a function of incident electron energy and angle of incidence, have been reviewed [1]. No error estimates are given⁴, rendering it impossible to judge the relative merits of theories quantitatively, by these measurements. However, it is easy to imagine that the random errors are large enough that, except in some narrow (~ 20 eV,) resonance-like energy bands, the measurements are consistent with the energy-independent, angle-independent, zero polarization predicted in the new theory of this chapter. One of the narrow energy bands includes 82 eV, allowing the measurements to be simultaneously consistent with the band-structure calculation for tungsten, mentioned earlier in this chapter. It could be conjectured that the narrow energy bands correspond to changes in wave-vector on reflection, which, in some sense, match the repeat distance of those parts of the atomic cores, which are of sufficiently deep potential to render the electrons' kinetic energy comparable with their rest mass energy, allowing spin-orbit polarizing effects to become significant, and removing these narrow energy bands from the domain of validity of the new theory in this chapter. Some of the published band-structure calculations, reviewed earlier in this chapter, appear to have captured phenomena of this type.

Also reviewed [1] are measurements of reflected beam polarization from a Cu_3Au (001) surface, as a function of incident beam energy, at an angle of incidence of 13° . In the energy region above ~ 60 eV, where the Taylor expansion allows the new theory of this chapter to make quantitative predictions, the measurements appear to tend rapidly with increasing incident energy, to the constant, zero polarization of this theory.

The same paper [1] goes on to review measurements of reflected beam polarization from a nickel (001) surface, as a function of incident beam energy and angle of incidence, as does another paper [4] in the same collection. For the former data set, in the energy region above ~ 60 eV, where the Taylor expansion allows the new theory of chapter 2 to make quantitative predictions, the measurements provide a very good match to the constant polarization this theory. However, they provide an approximately equally good match to the relevant, published band-structure calculation, reviewed earlier in this chapter. For philosophical reasons explained elsewhere [10], the author is inclined to assign a higher prior probability to the new theory of this chapter than to the band-structure theory, leading to the former being preferred in this case of roughly equal goodness of fit. However, prior

⁴However, some idea can be obtained from the level of reproducibility between different laboratories.

probabilities are [10] subjective, and readers are, therefore, fully entitled to disagree. The latter data set, which uses an estimator of the polarization designed to reveal only exchange effects, not spin-orbit effects, is a rather better match to the constant polarization, predicted by the new theory of this chapter, than to any of several band-structure theories, reviewed in that chapter.

Measurements of reflected beam polarization from an iron (110) surface, as a function of incident electron energy and angle of incidence, have been reviewed [4]. No error estimates are given⁵, rendering it impossible to judge the relative merits of theories quantitatively, by these measurements. However, it is easy to imagine that the random errors are large enough that the measurements are consistent with the energy-independent, angle-independent, possibly non-zero polarization predicted in the new theory of this chapter. However, the relevant band-structure theories, reviewed earlier in this chapter, provide approximately an equally good fit.

Also reviewed [1] are measurements of reflected beam polarization from a platinum (111) surface, as a function of the orientation of the scattering plane, relative to the crystal axes, at an incident electron energy of 60 eV, and an angle of incidence of 43.5° . Again, no error estimates are given, rendering it impossible to judge the relative merits of theories quantitatively, by these measurements. However, visually, the results appear to provide a superb match to the predictions of a band-structure calculation for this material, reviewed earlier in this chapter [1], and a very dubious match to the zero polarization predicted by the new theory of this chapter. Because the measurements were all taken at the same beam energy, the conjecture above, regarding narrow energy bands that are outside the domain of validity of the new theory in this chapter, might apply.

Also reviewed [1] are measurements of reflected beam polarization from a gold (110) surface, as a function of angle of incidence and temperature, at an incident electron energy of 50 eV. Once again, no error estimates are given, rendering it impossible to judge the relative merits of theories quantitatively, by these measurements. However, it does appear that there are substantial polarizations (up to 0.6,) which vary with angle of incidence. At energies as low as 50 eV, the lowest-order Taylor expansion in the inverse energy, which is used in the new theory of this chapter, is becoming dubious, and it is therefore not clear what this theory predicts, but if the Taylor expansion were valid, it would predict zero polarizations for all angles of incidence. Because the measurements were all taken at the same beam energy, the conjecture above,

⁵However, some idea can be obtained from the level of reproducibility between different laboratories.

Third-party copyrighted figure
omitted from version for
public online distribution

Figure 2.9: A Figure Reproduced from “Elastic Spin-Polarized Low-Energy Electron Scattering from Magnetic Surfaces” [4], Showing Experimental Measurements on a Graph of Reflected Electron Beam Polarization, Due to Exchange Effects, from $Fe(110)$, as a Percentage, against Electron Energy. For High Energies (above ~ 60 eV,) the Simple, New Theory of This Chapter Predicts an Energy-Independent Polarization.

regarding narrow energy bands that are outside the domain of validity of the new theory in this chapter, might apply.

Since the bulk of this thesis was completed, the author has also become aware of published experimental data [55] on the spin polarization of a reflected electron beam from a *Co/Cu*(001) film; the experiment was undertaken at a incident electron energy of 17 eV, and for a range of thicknesses up to ~ 2.5 ML; the intention was to detect the onset of ferro-magnetism with increasing thickness. Both the thicknesses and the beam energy are considerably lower than those studied in the new experiments presented in this thesis; therefore, the results are not directly comparable. At the onset of ferro-magnetism, a jump was observed from a spin polarization of zero to an “asymmetry” of ~ 0.19 . It is not clear whether this “asymmetry” represents an absolute polarization, or whether it requires calibration with something akin to a detector Sherman function.

2.11 List of Adaptations to the Polarimeter, and to the Measurement Technique, from *Mott Polarimetry at the Cavendish Laboratory* [8]

Mott polarimetry involves substantial technical difficulties. There follows a list of difficulties that were encountered with the Cavendish polarimeter, and measures that were taken to overcome them, in order to allow the experiments described in this thesis to proceed.

- Significant cross-talk was discovered between the signal output cables on the two channeltrons; this was largely eliminated by the installation of improved shielding within the polarimeter.
- The high voltage supply used to accelerate the electrons toward the thorium target was found to be unreliable; there was a considerable delay in the diagnosis of this fault due to the difficulty of finding a reasonably safe means of measuring the required potential difference of many kV. Once the supply had been discovered to be producing only 750 V, replacement of the offending control potentiometer was rapidly effected.
- The channeltrons are [66] designed as single-electron counting devices, intended to function by using an electrostatic field to accelerate an incoming electron into a collision, which liberates further electrons from

the channeltron walls, which are in turn accelerated to produce further collisions. This process amplifies a single electron into a current pulse containing $\sim 10^8$ electrons, which is readily detectable using a digital counter. However, the count rates measured by this method were found to be anomalously low. This is believed to be because the rate, at which electrons were arriving at the channeltrons, was substantially above the saturation rate ($\sim 10^4$ Hz,) at which the channeltrons' detection efficiency begins to drop rapidly with increasing electron arrival rate. This was the case with specularly reflected beams of energies between ~ 2 keV and ~ 3 keV from magnetic and non-magnetic surfaces, even for the smallest incident beam currents available. Therefore, it was necessary to make adaptations to allow the use of the front ends of the channeltrons as Faraday cups, the current collected at which could be measured as a continuous flow, rather than as discrete electron arrival events. To this end, an ammeter of sufficient sensitivity to measure the currents involved (of order 1pA) was procured, and a wire which connected the front ends of the two channeltrons, possibly allowing flow of current between them, was removed.

- With the high voltage supply to the thorium foil in operation, continuous current measurement revealed current spikes, occurring at a frequency of ~ 3 Hz, peaking at what later transpired to be approximately the steady current, which was obtained in successful measurements. The spikes were set against a background of substantially lower current, and were also detected as pulses in single electron counting mode, whether or not an accelerating potential difference was applied across the channeltrons. This is now believed to have been a consequence of the electrical connection to the thorium foil and surrounding assembly from outside the vacuum chamber having some freedom of movement inside its insulating casing, leading to a situation in which there was good electrical contact only for brief periods, occurring at ~ 3 Hz, producing the spikes that represented the current in the intended operating condition. The effect has disappeared since the mechanical security of the connection was improved.
- Calculation of raw asymmetries

$$A_{\text{raw},+} = \frac{f_{+,1} - f_{+,2}}{f_{+,1} + f_{+,2}}, \quad (2.16)$$

and

$$A_{\text{raw},-} = \frac{f_{-,1} - f_{-,2}}{f_{-,1} + f_{-,2}}, \quad (2.17)$$

from the measurements [8] on the reflected beam from $Cu/Mn/Co/Cu(001)$ shows larger uncertainties, and slightly poorer consistency between the two runs of the experiment than the results from the use of the formula (equation 5.16) for the elimination of multiplicative systematic errors, suggesting that the multiplicative errors do exist, and were subject to drift over the period between the two runs of the experiment, and that the use of the formula, with the polarization reversal achieved using opposite remanent magnetization directions of the film structure, was a necessary measure.

- The difficulty of adjusting the zero on the ammeter used for continuous current measurements, given its slow response both to the zeroing control and to changes in the current which it was measuring, led to a suspicion that there might be additive offsets which would require a fitting procedure of the kind introduced in *Mott Polarimetry at the Cavendish Laboratory* [8]. The non-zero and variable values obtained for the channeltron currents at zero incident beam current, using this procedure, indicate that such offsets do exist, and are subject to drift; therefore, both the fitting procedure and the time ordering of the experiments were necessary precautions.

Earlier, when this chapter's new, classical-field theory of polarized electron reflection was outlined, it was promised that the full algebraic details of that theory would follow. These are presented in the next section.

2.12 Theory of Polarized Electron Reflection: Full Algebraic Details

2.12.1 Amplitude Reflection Coefficient for an Electron Pure State, at a Single Step in Electric Potential and Magnetic Flux Density

The incident and transmitted electron waves are modelled (figure 2.3) as plane waves, allowing the well-defined wave-vector components p in the plane of the interface, and q_i perpendicular to the interface. p must be the same for all the waves, in order to satisfy the boundary condition of continuity of the wave-function at the interface. The amplitude reflection coefficient is [30]

$$r_{01} = \frac{q_0 - q_1}{q_0 + q_1}, \quad (2.18)$$

or, for a general interface,

$$r_{ij} = \frac{q_i - q_j}{q_i + q_j}. \quad (2.19)$$

Next, I need to build an expression for the energy of the electrons. There will be kinetic energy terms, which, in the non-relativistic limit, are

$$\frac{\hbar^2 p^2}{2m_e},$$

and

$$\frac{\hbar^2 q_i^2}{2m_e},$$

along with an electrostatic potential energy

$$-eV_i,$$

and a term due to the torque, on the electron magnetic moment, in a magnetic field [30]

$$\frac{e\hbar B_i \cos S_i}{2m_e},$$

where S_i is the angle between the electron spin and the magnetic flux density. The form of this last term assumes a well-defined energy for all values of S_i . Strictly, only certain S_i values are eigen-states of a Hamiltonian which includes a magnetic field; more about this later (section 2.5.) The total energy is

$$E = \frac{\hbar^2 p^2}{2m_e} + \frac{\hbar^2 q_i^2}{2m_e} - eV_i + \frac{e\hbar B_i \cos S_i}{2m_e}, \quad (2.20)$$

or, where p is expressed as a fraction $\sin I$ of the total wave-number in the absence of any potential, I being an angle of incidence like that in figure 2.2,

$$E = E \sin^2 I + \frac{\hbar^2 q_i^2}{2m_e} - eV_i + \frac{e\hbar B_i \cos S_i}{2m_e} \quad (2.21)$$

$$\begin{aligned} \Rightarrow q_i &= \left(\frac{2m_e E \cos^2 I}{\hbar^2} \right)^{1/2} \left(1 + \frac{eV_i}{E \cos^2 I} - \frac{e\hbar B_i \cos S_i}{2m_e E \cos^2 I} \right)^{1/2} \\ &= \left(\frac{2m_e E \cos^2 I}{\hbar^2} \right)^{1/2} (1 + x_i)^{1/2}, \end{aligned} \quad (2.22)$$

where $x_i = y_i + z_i \cos S_i$, $y_i = \frac{eV_i}{E \cos^2 I}$, and $z_i = -\frac{e\hbar B_i}{2m_e E \cos^2 I}$.

I now use a binomial expansion [48] for the case where the potential energy terms are much smaller than the total electron energy, where the dimensionless numbers I've just devised are small. The magnetic term associated with

the Weiss field in a ferromagnet is [43] a few tenths of an electron-volt, and the electrostatic contact potentials in the metals which I study will not be more than a few volts, whereas, in my experimental set-up, the incident electron energies range from a few hundred to a few thousand electron volts, so this approximation seems reasonable.

$$q_i = \left(\frac{2m_e E \cos^2 I}{\hbar^2} \right)^{1/2} \left(1 + \frac{1}{2}x_i - \frac{1}{8}x_i^2 + O(x_i^3) \right). \quad (2.23)$$

The amplitude reflection coefficient is, therefore,

$$\begin{aligned} r_{ij} &= \frac{1}{2} \left(\frac{1}{2}x_i - \frac{1}{2}x_j + \frac{1}{8}x_j^2 - \frac{1}{8}x_i^2 + O(\{x_i, x_j\}^3) \right) \\ &\quad \times \left(1 + \frac{1}{4}x_i + \frac{1}{4}x_j - \frac{1}{16}x_i^2 - \frac{1}{16}x_j^2 + O(\{x_i, x_j\}^3) \right)^{-1} \\ &= \frac{1}{2} \left(\frac{1}{2}x_i - \frac{1}{2}x_j + \frac{1}{8}x_j^2 - \frac{1}{8}x_i^2 + O(\{x_i, x_j\}^3) \right) \\ &\quad \times \left(1 - \frac{1}{4}x_i - \frac{1}{4}x_j + \frac{1}{8}x_i^2 + \frac{1}{8}x_i x_j + \frac{1}{8}x_j^2 + O(\{x_i, x_j\}^3) \right) \\ &= \frac{1}{2} \left(\frac{1}{2}x_i - \frac{1}{2}x_j - \frac{1}{4}x_i^2 - \frac{1}{4}x_i x_j + \frac{1}{4}x_j^2 + O(\{x_i, x_j\}^3) \right) \\ &= \frac{1}{4}x_i - \frac{1}{4}x_j - \frac{1}{8}x_i^2 - \frac{1}{8}x_i x_j + \frac{1}{8}x_j^2 + O(\{x_i, x_j\}^3). \end{aligned} \quad (2.24)$$

2.12.2 Reflection of an Unpolarized Beam from the Surface of a Bulk Magnetic Sample

An unpolarized incident electron beam is [31, 32] an incoherent superposition of pure states representing all directions of the incident spin. Each such direction can be represented by its spherical polar angle co-ordinates (θ, ϕ) . That is to say, the incident beam contains a flux of electrons

$$F_1 d\theta d\phi = A \sin \theta d\theta d\phi \quad (2.25)$$

with polarization direction between θ and $\theta + d\theta$, and between ϕ and $\phi + d\phi$. The flux of such electrons in the reflected beam will, therefore, be

$$F_2 d\theta d\phi = |r_{ij}|^2 F_1 d\theta d\phi. \quad (2.26)$$

The reflection from the surface of a bulk sample is to be modelled as a single reflection, of amplitude reflection coefficient r_{01} , in a situation where

V_0 , B_0 , and therefore x_0 , are all zero. In this case,

$$r_{01} = -\frac{1}{4}x_1 + \frac{1}{8}x_1^2 + O(x_1^3), \quad (2.27)$$

and

$$|r_{01}|^2 = \frac{1}{16}x_1^2 - \frac{1}{16}x_1^3 + O(x_1^4), \quad (2.28)$$

assuming that r_{01} is real.

If the spherical polar representation (θ_i, ϕ_i) is used for the direction of the magnetic flux density in region i , then

$$\cos S_i = \sin \theta_i \cos \phi_i \sin \theta \cos \phi + \sin \theta_i \sin \phi_i \sin \theta \sin \phi + \cos \theta_i \cos \theta. \quad (2.29)$$

Therefore,

$$x_i = y_i + z_i(\sin \theta_i \cos \phi_i \sin \theta \cos \phi + \sin \theta_i \sin \phi_i \sin \theta \sin \phi + \cos \theta_i \cos \theta). \quad (2.30)$$

The polarization of the pure state represented by (θ, ϕ) , in the Cartesian co-ordinate system associated with this spherical polar system, is

$$\mathbf{P}(\theta, \phi) = (\sin \theta \cos \phi, \sin \theta \sin \phi, \cos \theta), \quad (2.31)$$

and the average polarization of the reflected beam is

$$\begin{aligned} \mathbf{P} &= \frac{\int_{\theta=0}^{\pi} \int_{\phi=0}^{2\pi} \mathbf{P}(\theta, \phi) F_2 d\theta d\phi}{\int_{\theta=0}^{\pi} \int_{\phi=0}^{2\pi} F_2 d\theta d\phi} \\ &= \frac{\int_{\theta=0}^{\pi} \int_{\phi=0}^{2\pi} (\sin \theta \cos \phi, \sin \theta \sin \phi, \cos \theta) |r_{01}|^2 F_1 d\theta d\phi}{\int_{\theta=0}^{\pi} \int_{\phi=0}^{2\pi} |r_{01}|^2 F_1 d\theta d\phi} \\ &= \frac{\int_{\theta=0}^{\pi} \int_{\phi=0}^{2\pi} (\sin \theta \cos \phi, \sin \theta \sin \phi, \cos \theta) \left(\frac{1}{16}x_1^2 - \frac{1}{16}x_1^3 + O(x_1^4) \right) \sin \theta d\theta d\phi}{\int_{\theta=0}^{\pi} \int_{\phi=0}^{2\pi} \left(\frac{1}{16}x_1^2 - \frac{1}{16}x_1^3 + O(x_1^4) \right) \sin \theta d\theta d\phi} \\ &= \frac{(I_2 - I_6, I_3 - I_7, I_4 - I_8) + O(\{y_1, z_1\}^4)}{I_1 - I_5 + O(\{y_1, z_1\}^4)}. \end{aligned} \quad (2.32)$$

The crucial integrals are

$$\begin{aligned} I_1 &= \int_{\theta=0}^{\pi} \int_{\phi=0}^{2\pi} x_1^2 \sin \theta d\theta d\phi \\ &= \int_{\theta=0}^{\pi} \int_{\phi=0}^{2\pi} (y_1 + z_1(\sin \theta_1 \cos \phi_1 \sin \theta \cos \phi + \sin \theta_1 \sin \phi_1 \sin \theta \sin \phi \\ &\quad + \cos \theta_1 \cos \theta))^2 \sin \theta d\theta d\phi \end{aligned}$$

$$\begin{aligned}
&= \int_{\theta=0}^{\pi} \int_{\phi=0}^{2\pi} (y_1^2 \sin \theta \\
&\quad + 2y_1 z_1 (\sin \theta_1 \cos \phi_1 \sin^2 \theta \cos \phi + \sin \theta_1 \sin \phi_1 \sin^2 \theta \sin \phi + \cos \theta_1 \sin \theta \cos \theta) \\
&\quad + z_1^2 (\sin^2 \theta_1 \cos^2 \phi_1 \sin^3 \theta \cos^2 \phi + 2 \sin^2 \theta_1 \sin \phi_1 \cos \phi_1 \sin^3 \theta \sin \phi \cos \phi \\
&\quad + 2 \sin \theta_1 \cos \theta_1 \cos \phi_1 \sin^2 \theta \cos \theta \cos \phi + \sin^2 \theta_1 \sin^2 \phi_1 \sin^3 \theta \sin^2 \phi \\
&\quad + 2 \sin \theta_1 \cos \theta_1 \sin \phi_1 \sin^2 \theta \cos \theta \sin \phi + \cos^2 \theta_1 \sin \theta \cos^2 \theta)) d\theta d\phi \\
&= 4\pi y_1^2 + \frac{4\pi z_1^2}{3}, \tag{2.33}
\end{aligned}$$

$$\begin{aligned}
I_2 &= \int_{\theta=0}^{\pi} \int_{\phi=0}^{2\pi} x_1^2 \sin^2 \theta \cos \phi d\theta d\phi \\
&= \int_{\theta=0}^{\pi} \int_{\phi=0}^{2\pi} (y_1 + z_1 (\sin \theta_1 \cos \phi_1 \sin \theta \cos \phi + \sin \theta_1 \sin \phi_1 \sin \theta \sin \phi \\
&\quad + \cos \theta_1 \cos \theta))^2 \sin^2 \theta \cos \phi d\theta d\phi \\
&= \int_{\theta=0}^{\pi} \int_{\phi=0}^{2\pi} (y_1^2 \sin^2 \theta \cos \phi \\
&\quad + 2y_1 z_1 (\sin \theta_1 \cos \phi_1 \sin^3 \theta \cos^2 \phi + \sin \theta_1 \sin \phi_1 \sin^3 \theta \sin \phi \cos \phi \\
&\quad + \cos \theta_1 \sin^2 \theta \cos \theta \cos \phi) \\
&\quad + z_1^2 (\sin^2 \theta_1 \cos^2 \phi_1 \sin^4 \theta \cos^3 \phi + 2 \sin^2 \theta_1 \sin \phi_1 \cos \phi_1 \sin^4 \theta \sin \phi \cos^2 \phi \\
&\quad + 2 \sin \theta_1 \cos \theta_1 \cos \phi_1 \sin^3 \theta \cos \theta \cos^2 \phi + \sin^2 \theta_1 \sin^2 \phi_1 \sin^4 \theta \sin^2 \phi \cos \phi \\
&\quad + 2 \sin \theta_1 \cos \theta_1 \sin \phi_1 \sin^3 \theta \cos \theta \sin \phi \cos \phi + \cos^2 \theta_1 \sin^2 \theta \cos^2 \theta \cos \phi)) d\theta d\phi \\
&= \frac{8\pi y_1 z_1 \sin \theta_1 \cos \phi_1}{3}, \tag{2.34}
\end{aligned}$$

$$\begin{aligned}
I_3 &= \int_{\theta=0}^{\pi} \int_{\phi=0}^{2\pi} x_1^2 \sin^2 \theta \sin \phi d\theta d\phi \\
&= \int_{\theta=0}^{\pi} \int_{\phi=0}^{2\pi} (y_1 + z_1 (\sin \theta_1 \cos \phi_1 \sin \theta \cos \phi + \sin \theta_1 \sin \phi_1 \sin \theta \sin \phi \\
&\quad + \cos \theta_1 \cos \theta))^2 \sin^2 \theta \sin \phi d\theta d\phi \\
&= \int_{\theta=0}^{\pi} \int_{\phi=0}^{2\pi} (y_1^2 \sin^2 \theta \sin \phi \\
&\quad + 2y_1 z_1 (\sin \theta_1 \cos \phi_1 \sin^3 \theta \sin \phi \cos \phi + \sin \theta_1 \sin \phi_1 \sin^3 \theta \sin^2 \phi \\
&\quad + \cos \theta_1 \sin^2 \theta \cos \theta \sin \phi) \\
&\quad + z_1^2 (\sin^2 \theta_1 \cos^2 \phi_1 \sin^4 \theta \sin \phi \cos^2 \phi + 2 \sin^2 \theta_1 \sin \phi_1 \cos \phi_1 \sin^4 \theta \sin^2 \phi \cos \phi \\
&\quad + 2 \sin \theta_1 \cos \theta_1 \cos \phi_1 \sin^3 \theta \cos \theta \sin \phi \cos \phi + \sin^2 \theta_1 \sin^2 \phi_1 \sin^4 \theta \sin^3 \phi) \\
&\quad + \cos^2 \theta_1 \sin^2 \theta \cos^2 \theta \sin \phi)) d\theta d\phi
\end{aligned}$$

$$\begin{aligned}
& +2 \sin \theta_1 \cos \theta_1 \sin \phi_1 \sin^3 \theta \cos \theta \sin^2 \phi + \cos^2 \theta_1 \sin^2 \theta \cos^2 \theta \sin \phi)) d\theta d\phi \\
= & \frac{8\pi y_1 z_1 \sin \theta_1 \sin \phi_1}{3}, \tag{2.35}
\end{aligned}$$

$$\begin{aligned}
I_4 &= \int_{\theta=0}^{\pi} \int_{\phi=0}^{2\pi} x_1^2 \sin \theta \cos \theta d\theta d\phi \\
&= \int_{\theta=0}^{\pi} \int_{\phi=0}^{2\pi} (y_1 + z_1(\sin \theta_1 \cos \phi_1 \sin \theta \cos \phi + \sin \theta_1 \sin \phi_1 \sin \theta \sin \phi \\
&\quad + \cos \theta_1 \cos \theta))^2 \sin \theta \cos \theta d\theta d\phi \\
&= \int_{\theta=0}^{\pi} \int_{\phi=0}^{2\pi} (y_1^2 \sin \theta \cos \theta \\
&\quad + 2y_1 z_1(\sin \theta_1 \cos \phi_1 \sin^2 \theta \cos \theta \cos \phi + \sin \theta_1 \sin \phi_1 \sin^2 \theta \cos \theta \sin \phi + \cos \theta_1 \sin \theta \cos^2 \theta) \\
&\quad + z_1^2(\sin^2 \theta_1 \cos^2 \phi_1 \sin^3 \theta \cos \theta \cos^2 \phi + 2 \sin^2 \theta_1 \sin \phi_1 \cos \phi_1 \sin^3 \theta \cos \theta \sin \phi \cos \phi \\
&\quad + 2 \sin \theta_1 \cos \theta_1 \cos \phi_1 \sin^2 \theta \cos^2 \theta \cos \phi + \sin^2 \theta_1 \sin^2 \phi_1 \sin^3 \theta \cos \theta \sin^2 \phi \\
&\quad + 2 \sin \theta_1 \cos \theta_1 \sin \phi_1 \sin^2 \theta \cos^2 \theta \sin \phi + \cos^2 \theta_1 \sin \theta \cos^3 \theta)) d\theta d\phi \\
&= \frac{8\pi y_1 z_1 \cos \theta_1}{3}, \tag{2.36}
\end{aligned}$$

$$\begin{aligned}
I_5 &= \int_{\theta=0}^{\pi} \int_{\phi=0}^{2\pi} x_1^3 \sin \theta d\theta d\phi \\
&= \int_{\theta=0}^{\pi} \int_{\phi=0}^{2\pi} (y_1 + z_1(\sin \theta_1 \cos \phi_1 \sin \theta \cos \phi + \sin \theta_1 \sin \phi_1 \sin \theta \sin \phi \\
&\quad + \cos \theta_1 \cos \theta))^3 \sin \theta d\theta d\phi \\
&= \int_{\theta=0}^{\pi} \int_{\phi=0}^{2\pi} (y_1^3 \sin \theta \\
&\quad + 3y_1^2 z_1(\sin \theta_1 \cos \phi_1 \sin^2 \theta \cos \phi + \sin \theta_1 \sin \phi_1 \sin^2 \theta \sin \phi + \cos \theta_1 \sin \theta \cos \theta) \\
&\quad + 3y_1 z_1^2(\sin^2 \theta_1 \cos^2 \phi_1 \sin^3 \theta \cos^2 \phi + 2 \sin^2 \theta_1 \sin \phi_1 \cos \phi_1 \sin^3 \theta \sin \phi \cos \phi \\
&\quad + 2 \sin \theta_1 \cos \theta_1 \cos \phi_1 \sin^2 \theta \cos \theta \cos \phi + \sin^2 \theta_1 \sin^2 \phi_1 \sin^3 \theta \sin^2 \phi \\
&\quad + 2 \sin \theta_1 \cos \theta_1 \sin \phi_1 \sin^2 \theta \cos \theta \sin \phi + \cos^2 \theta_1 \sin \theta \cos^2 \theta) \\
&\quad + z_1^3(\sin^3 \theta_1 \cos^3 \phi_1 \sin^4 \theta \cos^3 \phi + 3 \sin^3 \theta_1 \sin \phi_1 \cos^2 \phi_1 \sin^4 \theta \sin \phi \cos^2 \phi \\
&\quad + 3 \sin^2 \theta_1 \cos \theta_1 \cos^2 \phi_1 \sin^3 \theta \cos \theta \cos^2 \phi + 3 \sin^3 \theta_1 \sin^2 \phi_1 \cos \phi_1 \sin^4 \theta \sin^2 \phi \cos \phi \\
&\quad + 6 \sin^2 \theta_1 \cos \theta_1 \sin \phi_1 \cos \phi_1 \sin^3 \theta \cos \theta \sin \phi \cos \phi + 3 \sin \theta_1 \cos^2 \theta_1 \cos \phi_1 \sin^2 \theta \cos^2 \theta \cos \phi \\
&\quad + \sin^3 \theta_1 \sin^3 \phi_1 \sin^4 \theta \sin^3 \phi + 3 \sin^2 \theta_1 \cos \theta_1 \sin^2 \phi_1 \sin^3 \theta \cos \theta \sin^2 \phi \\
&\quad + 3 \sin \theta_1 \cos^2 \theta_1 \sin \phi_1 \sin^2 \theta \cos^2 \theta \sin \phi + \cos^3 \theta_1 \sin \theta \cos^3 \theta)) d\theta d\phi \\
&= 4\pi y_1 z_1^2, \tag{2.37}
\end{aligned}$$

$$\begin{aligned}
I_6 &= \int_{\theta=0}^{\pi} \int_{\phi=0}^{2\pi} x_1^3 \sin^2 \theta \cos \phi d\theta d\phi \\
&= \int_{\theta=0}^{\pi} \int_{\phi=0}^{2\pi} (y_1^3 \sin^2 \theta \cos \phi \\
&\quad + 3y_1^2 z_1 (\sin \theta_1 \cos \phi_1 \sin^3 \theta \cos^2 \phi + \sin \theta_1 \sin \phi_1 \sin^3 \theta \sin \phi \cos \phi \\
&\quad + \cos \theta_1 \sin^2 \theta \cos \theta \cos \phi) \\
&\quad + 3y_1 z_1^2 (\sin^2 \theta_1 \cos^2 \phi_1 \sin^4 \theta \cos^3 \phi + 2 \sin^2 \theta_1 \sin \phi_1 \cos \phi_1 \sin^4 \theta \sin \phi \cos^2 \phi \\
&\quad + 2 \sin \theta_1 \cos \theta_1 \cos \phi_1 \sin^3 \theta \cos \theta \cos^2 \phi + \sin^2 \theta_1 \sin^2 \phi_1 \sin^4 \theta \sin^2 \phi \cos \phi \\
&\quad + 2 \sin \theta_1 \cos \theta_1 \sin \phi_1 \sin^3 \theta \cos \theta \sin \phi \cos \phi + \cos^2 \theta_1 \sin^2 \theta \cos^2 \theta \cos \phi) \\
&\quad + z_1^3 (\sin^3 \theta_1 \cos^3 \phi_1 \sin^5 \theta \cos^4 \phi + 3 \sin^3 \theta_1 \sin \phi_1 \cos^2 \phi_1 \sin^5 \theta \sin \phi \cos^3 \phi \\
&\quad + 3 \sin^2 \theta_1 \cos \theta_1 \cos^2 \phi_1 \sin^4 \theta \cos \theta \cos^3 \phi \\
&\quad + 3 \sin^3 \theta_1 \sin^2 \phi_1 \cos \phi_1 \sin^5 \theta \sin^2 \phi \cos^2 \phi \\
&\quad + 6 \sin^2 \theta_1 \cos \theta_1 \sin \phi_1 \cos \phi_1 \sin^4 \theta \cos \theta \sin \phi \cos^2 \phi + 3 \sin \theta_1 \cos^2 \theta_1 \cos \phi_1 \sin^3 \theta \cos^2 \theta \cos^2 \phi \\
&\quad + \sin^3 \theta_1 \sin^3 \phi_1 \sin^5 \theta \sin^3 \phi \cos \phi + 3 \sin^2 \theta_1 \cos \theta_1 \sin^2 \phi_1 \sin^4 \theta \cos \theta \sin^2 \phi \cos \phi \\
&\quad + 3 \sin \theta_1 \cos^2 \theta_1 \sin \phi_1 \sin^3 \theta \cos^2 \theta \sin \phi \cos \phi + \cos^3 \theta_1 \sin^2 \theta \cos^3 \theta \cos \phi)) d\theta d\phi \\
&= \left(4\pi y_1^2 z_1 + \frac{4\pi z_1^3}{5} \right) \sin \theta_1 \cos \phi_1, \tag{2.38}
\end{aligned}$$

$$\begin{aligned}
I_7 &= \int_{\theta=0}^{\pi} \int_{\phi=0}^{2\pi} x_1^3 \sin^2 \theta \sin \phi d\theta d\phi \\
&= \int_{\theta=0}^{\pi} \int_{\phi=0}^{2\pi} (y_1^3 \sin^2 \theta \sin \phi \\
&\quad + 3y_1^2 z_1 (\sin \theta_1 \cos \phi_1 \sin^3 \theta \sin \phi \cos \phi + \sin \theta_1 \sin \phi_1 \sin^3 \theta \sin^2 \phi \\
&\quad + \cos \theta_1 \sin^2 \theta \cos \theta \sin \phi) \\
&\quad + 3y_1 z_1^2 (\sin^2 \theta_1 \cos^2 \phi_1 \sin^4 \theta \sin \phi \cos^2 \phi + 2 \sin^2 \theta_1 \sin \phi_1 \cos \phi_1 \sin^4 \theta \sin^2 \phi \cos \phi \\
&\quad + 2 \sin \theta_1 \cos \theta_1 \cos \phi_1 \sin^3 \theta \cos \theta \sin \phi \cos \phi + \sin^2 \theta_1 \sin^2 \phi_1 \sin^4 \theta \sin^3 \phi \\
&\quad + 2 \sin \theta_1 \cos \theta_1 \sin \phi_1 \sin^3 \theta \cos \theta \sin^2 \phi + \cos^2 \theta_1 \sin^2 \theta \cos^2 \theta \sin \phi) \\
&\quad + z_1^3 (\sin^3 \theta_1 \cos^3 \phi_1 \sin^5 \theta \sin \phi \cos^3 \phi + 3 \sin^3 \theta_1 \sin \phi_1 \cos^2 \phi_1 \sin^5 \theta \sin^2 \phi \cos^2 \phi \\
&\quad + 3 \sin^2 \theta_1 \cos \theta_1 \cos^2 \phi_1 \sin^4 \theta \cos \theta \sin \phi \cos^2 \phi + 3 \sin^3 \theta_1 \sin^2 \phi_1 \cos \phi_1 \sin^5 \theta \sin^3 \phi \cos \phi \\
&\quad + 6 \sin^2 \theta_1 \cos \theta_1 \sin \phi_1 \cos \phi_1 \sin^4 \theta \cos \theta \sin^2 \phi \cos \phi \\
&\quad + 3 \sin \theta_1 \cos^2 \theta_1 \cos \phi_1 \sin^3 \theta \cos^2 \theta \sin \phi \cos \phi \\
&\quad + \sin^3 \theta_1 \sin^3 \phi_1 \sin^5 \theta \sin^4 \phi + 3 \sin^2 \theta_1 \cos \theta_1 \sin^2 \phi_1 \sin^4 \theta \cos \theta \sin^3 \phi \\
&\quad + 3 \sin \theta_1 \cos^2 \theta_1 \sin \phi_1 \sin^3 \theta \cos^2 \theta \sin^2 \phi + \cos^3 \theta_1 \sin^2 \theta \cos^3 \theta \sin \phi)) d\theta d\phi \\
&= \left(4\pi y_1^2 z_1 + \frac{4\pi z_1^3}{5} \right) \sin \theta_1 \sin \phi_1, \tag{2.39}
\end{aligned}$$

and

$$\begin{aligned}
I_8 &= \int_{\theta=0}^{\pi} \int_{\phi=0}^{2\pi} x_1^3 \sin \theta \cos \theta d\theta d\phi \\
&= \int_{\theta=0}^{\pi} \int_{\phi=0}^{2\pi} (y_1^3 \sin \theta \cos \theta \\
&\quad + 3y_1^2 z_1 (\sin \theta_1 \cos \phi_1 \sin^2 \theta \cos \theta \cos \phi + \sin \theta_1 \sin \phi_1 \sin^2 \theta \cos \theta \sin \phi + \cos \theta_1 \sin \theta \cos^2 \theta) \\
&\quad + 3y_1 z_1^2 (\sin^2 \theta_1 \cos^2 \phi_1 \sin^3 \theta \cos \theta \cos^2 \phi + 2 \sin^2 \theta_1 \sin \phi_1 \cos \phi_1 \sin^3 \theta \cos \theta \sin \phi \cos \phi \\
&\quad + 2 \sin \theta_1 \cos \theta_1 \cos \phi_1 \sin^2 \theta \cos^2 \theta \cos \phi + \sin^2 \theta_1 \sin^2 \phi_1 \sin^3 \theta \cos \theta \sin^2 \phi \\
&\quad + 2 \sin \theta_1 \cos \theta_1 \sin \phi_1 \sin^2 \theta \cos^2 \theta \sin \phi + \cos^2 \theta_1 \sin \theta \cos^3 \theta) \\
&\quad + z_1^3 (\sin^3 \theta_1 \cos^3 \phi_1 \sin^4 \theta \cos \theta \cos^3 \phi + 3 \sin^3 \theta_1 \sin \phi_1 \cos^2 \phi_1 \sin^4 \theta \cos \theta \sin \phi \cos^2 \phi \\
&\quad + 3 \sin^2 \theta_1 \cos \theta_1 \cos^2 \phi_1 \sin^3 \theta \cos^2 \theta \cos^2 \phi + 3 \sin^3 \theta_1 \sin^2 \phi_1 \cos \phi_1 \sin^4 \theta \cos \theta \sin^2 \phi \cos \phi \\
&\quad + 6 \sin^2 \theta_1 \cos \theta_1 \sin \phi_1 \cos \phi_1 \sin^3 \theta \cos^2 \theta \sin \phi \cos \phi \\
&\quad + 3 \sin \theta_1 \cos^2 \theta_1 \cos \phi_1 \sin^2 \theta \cos^3 \theta \cos \phi \\
&\quad + \sin^3 \theta_1 \sin^3 \phi_1 \sin^4 \theta \cos \theta \sin^3 \phi + 3 \sin^2 \theta_1 \cos \theta_1 \sin^2 \phi_1 \sin^3 \theta \cos^2 \theta \sin^2 \phi \\
&\quad + 3 \sin \theta_1 \cos^2 \theta_1 \sin \phi_1 \sin^2 \theta \cos^3 \theta \sin \phi + \cos^3 \theta_1 \sin \theta \cos^4 \theta)) d\theta d\phi \\
&= \left(4\pi y_1^2 z_1 + \frac{4\pi z_1^3}{5} \right) \cos \theta_1. \tag{2.40}
\end{aligned}$$

This gives a polarization

$$\begin{aligned}
\mathbf{P} &= \frac{(I_2 - I_6, I_3 - I_7, I_4 - I_8) + O(\{y_1, z_1\}^4)}{I_1 - I_5 + O(\{y_1, z_1\}^4)} \\
&= \frac{(10y_1 z_1 - 15y_1^2 z_1 - 3z_1^3)(\sin \theta_1 \cos \phi_1, \sin \theta_1 \sin \phi_1, \cos \theta_1) + O(\{y_1, z_1\}^4)}{15y_1^2 + 5z_1^2 - 15y_1 z_1^2 + O(\{y_1, z_1\}^4)} \\
&= \frac{(10y_1 z_1 - 15y_1^2 z_1 - 3z_1^3)\hat{\mathbf{B}}_1 + O(\{y_1, z_1\}^4)}{15y_1^2 + 5z_1^2} \left(1 - \frac{5y_1 z_1^2}{3y_1^2 + z_1^2} + O(\{y_1, z_1\}^2) \right)^{-1} \\
&= \frac{2y_1 z_1 \hat{\mathbf{B}}_1}{3y_1^2 + z_1^2} + \frac{(36y_1^2 z_1^3 - 45y_1^4 z_1 - 3z_1^5)\hat{\mathbf{B}}_1}{45y_1^4 + 30y_1^2 z_1^2 + 5z_1^4} + O(\{y_1, z_1\}^2), \tag{2.41}
\end{aligned}$$

where $\hat{\mathbf{B}}_1$ is a unit vector, in the direction of the magnetic flux density in region 1.

Part II

The Experimental Apparatus

Chapter 3

Mott Polarimetry and The Compact Retarding-Potential Mott Polarimeter

3.1 Theoretical Physics of Mott Polarimetry

Mott polarimetry is a means of measuring the spin polarization of an electron beam, and finds its most frequent application in photo-emission spectroscopy [67] and the study of surfaces, thin films and multi-layers [68]. The latter is the application with which this thesis is primarily concerned. Mott polarimeters are based on the left-right asymmetry in the scattering of polarized electrons by atoms, i.e. the relative difference in scattering cross-section between scattering events through the same angle in opposite senses (equation 3.2,) and its use as an indicator of the incident beam's spin polarization [34]. Common choices of scatterer for Mott polarimeters are gold, thorium and uranium foils [5, 34]. All of these have high proton numbers Z , leading to a large spin-dependent potential correction (equation 3.1.) Thorium and uranium provide a value of total scattering cross-section σ_0 (equation 3.2) which is around 15% greater than that for gold [5, 34] and an analysing power S (equation 3.2) which is improved by between 10% and 20% [34] or even as much as 30% [5]. On the other hand, thorium and uranium have the disadvantage that their chemical reactivity renders them more sensitive than gold to atmospheric contaminants, which may reduce both overall cross-section and Sherman function (section 3.1.2) [5, 34]. For the polarimeter used in this project, a thorium foil has been chosen (figure 3.1.)

3.1.1 The Spin-Dependence of the Scattering Potential

The differential cross-section as a function of scattering angle in Mott scattering, i.e. the scattering of electrons by nuclei at small impact parameters, exhibits a dependence on the electron spin direction [5, 34]. As Kessler [31, 32] points out, in addition to simplifying the potential calculation, the use of small impact parameters, i.e. high energies and large scattering angles, increases the analysing power of the polarimeter, as a result of the $\frac{1}{|\mathbf{r}|^3}$ dependence of the spin-orbit correction (equation 3.1.) The mechanism for this can be understood classically, as the additional, position-dependent term in the scattering potential, resulting from the torque exerted on the electron's spin magnetic moment, by the magnetic field due to the presence of a moving, charged nucleus in the electron's rest frame [5, 34]. Gay & Dunning [5] and Dunning [34] have developed a quantitative version of this model for a single scattering nucleus, which results in the expression for the spin-dependent potential contribution

$$V'_{so} = \frac{Ze\mu_B \mathbf{L} \cdot \mathbf{S}}{8\pi\epsilon_0 \hbar m_e c^2 |\mathbf{r}|^3}, \quad (3.1)$$

where Z is the proton number of the nucleus, μ_B is the Bohr magneton, \mathbf{L} is the orbital and \mathbf{S} the spin angular momentum of the electron, in the rest frame of the nucleus, and \mathbf{r} is the displacement of the electron from the nucleus. This potential form is equivalent to the fine splitting by the spin-orbit interaction familiar from the analysis of bound electronic states in atomic physics [45]. Kessler [31, 32] also makes some helpful comments on this model.

3.1.2 Spin-Dependence of the Scattering Cross-Section

By subjecting the general solution of the Dirac equation for a central potential to the condition that the electron wave-function is a superposition of a plane incident wave with a spherical (in wavefront geometry, not necessarily in the symmetry of the scattered amplitude) scattered wave, Kessler [31, 32] finds it possible to express the effect of a spin-dependent potential correction on the scattering cross-section σ (whether differential or integrated over a particular solid angle) as

$$\sigma = \sigma_0(1 + SP), \quad (3.2)$$

where σ_0 and S are functions of the incident electron energy E_b , and of the scattering angle θ , and P is the component of the spin polarization of the incident beam along the normal to the scattering plane; that is to say, if the electrons were forced to collapse into states of well-defined spin component

along this direction, the fractions with spin up f_u and spin down f_d would be such that

$$P = f_u - f_d. \quad (3.3)$$

S is known as the asymmetry function [69, 5, 34], the Sherman function [31, 32, 5, 34] or the analysing power [34, 70]. The only assumption about the form of the potential that was required to obtain this result was its separability in spherical polar co-ordinates. All the finer details of the potential, be it that of a single atom (section 3.1.1) or that of a metal foil of the kind found in a real polarimeter (figure 3.1,) are contained in the functional forms of σ_0 and S . In particular, if there were no mechanism, of the kind described in equation 3.1, for spin-dependence in the scattering potential, then S would vanish.

Equation 3.2 leads directly to the left-right asymmetry in scattering of a polarized electron beam. Two detectors are so placed as to collect scattered electron beams with scattering angles of the same magnitude, but in opposite senses (figure 3.1.) The scattering plane normals for the two detectors are therefore in opposite directions, i.e. the polarization component P is of the same magnitude but opposite sign at the two detectors. For a scatterer of even quite low symmetry, S will be the same for both detectors, with the result that the rates of electron arrival at the two detectors, R_1 and R_2 , will be [5, 34], from equation 3.2

$$R_1 = R_0(1 + SP), \quad (3.4)$$

and

$$R_2 = R_0(1 - SP). \quad (3.5)$$

In the case of the compact retarding-potential polarimeter (figure 3.1, chapter 3,) it is possible to obtain S for some values of the energy of the incident electrons at the target and the energy window defined by the retarding potential from look-up tables [6]. Combining equations 3.4 and 3.5, the polarization is

$$P = \frac{R_1 - R_2}{S(R_1 + R_2)}. \quad (3.6)$$

3.2 The Instrument at the Cavendish Laboratory

A Mott polarimeter has been available at the Cavendish Laboratory for some time. The main purpose of the polarimetry project to date has been to increase its reliability as a measuring device to the point where it can be used

to determine the polarization of a reflected, diffracted or secondary electron beam from an ultra-thin magnetic film structure. The latter has now been achieved using a specularly reflected electron beam from a film structure that previous research has suggested is of interest (chapter 2.8.) This has required the finding of technical solutions to a variety of instrumental difficulties [8] (sections 5.4, 5.5.)

The polarimeter now in use at the Cavendish Laboratory is of the compact, retarding-potential type (figure 3.1) [71, 34]. The detector position is chosen because there is a broad maximum in the Sherman function S , defined above, for metal foils at a scattering angle of around 120° [34]. Electrons are focused onto the thorium target by the electrostatic grids and lenses at the front of the device (figure 3.1,) and are accelerated to energies between 20 keV and 25 keV, suitable for the required low impact parameter scattering, by an electrostatic potential applied at the thorium foil [34]. An electrostatic potential applied at the retarding grids (figure 3.1) turns back electrons which have lost more than some specified amount of energy, chosen by setting the retarding grid potential, during the scattering process [34]. This eliminates a large proportion of multiply scattered electrons, for which the Sherman function S is reduced, without the reduction in the total cross-section σ_0 , which is brought about by using a thin film target to reduce multiple scattering [72].

The use of a retarding potential also means that the external electrodes can all be kept grounded, with the obviation of the need for bulky shielding on the detector as well as the direct safety benefits [34]. This, coupled with the relatively small target potential of ~ 22 kV, which restricts the inter-electrode distances needed to avoid electrical breakdown, keeps the instrument small (the distance between the two channeltrons is ~ 10 cm) [34], which is convenient for its attachment to a vacuum chamber (chapter 4) for experiments and for development and maintenance. In addition, the closeness of the channeltrons to the target, and the large solid angle which they therefore subtend, allows for a high total scattering cross-section σ_0 (equation 3.2) [34]. The relatively low energy of electrons incident on the thorium foil (figure 3.1) also increases σ_0 .

3.2.1 The Channeltron

The nature of the channeltron is presented in figure 3.2. The functioning of the device in electron-counting mode is described in detail in its manual [66]. It can also be operated in a continuous current measurement mode, with a small, positive collector voltage and a sensitive ammeter connected to its front end.

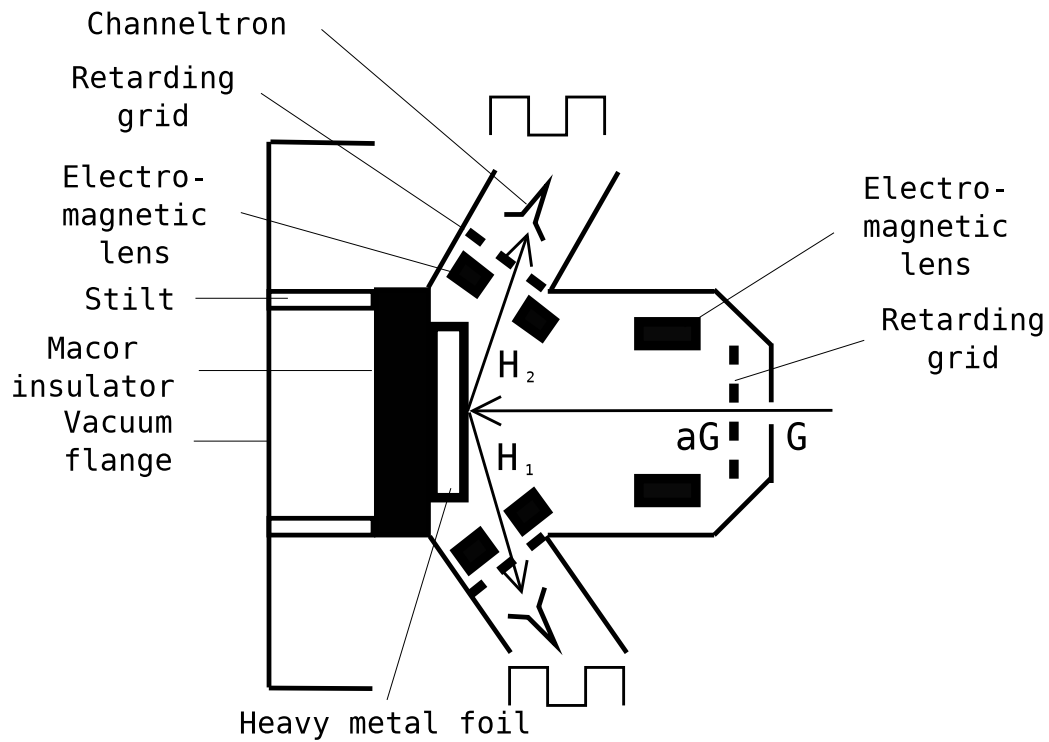


Figure 3.1: The Compact Retarding Potential Mott Polarimeter. G Represents the Rate at which Electrons Arrive at the Front of the Polarimeter, a the Fraction of Those Electrons that Are Accepted into the Polarimeter, and H_i the Rate at which Electrons Are Scattered towards Channeltron i .

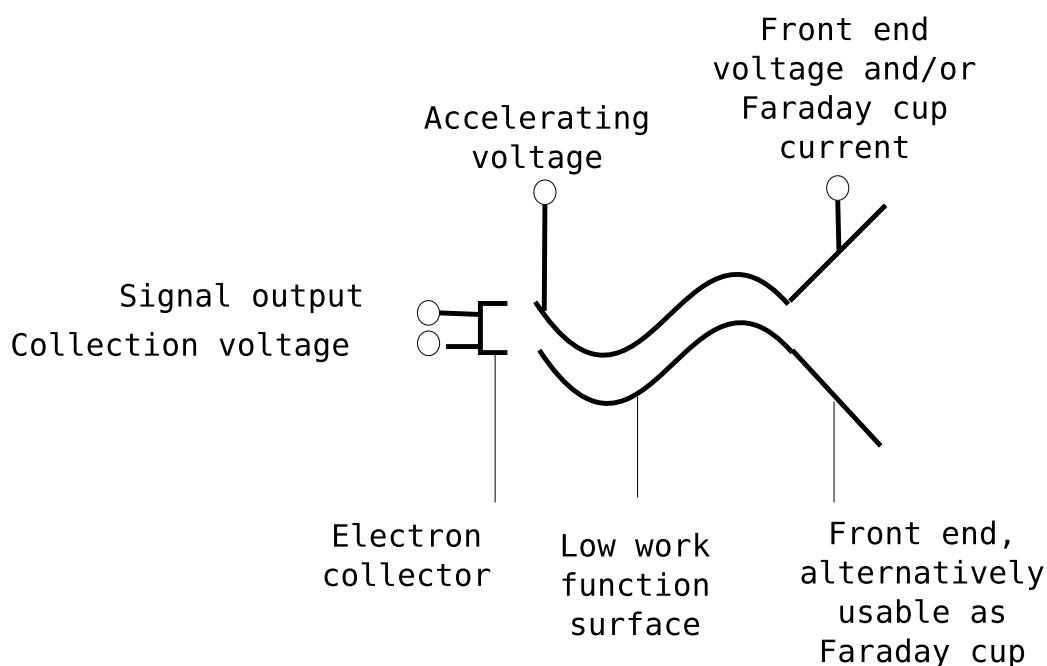


Figure 3.2: A Channeltron

An electron source is also needed for the experiments; for this, a commercial electron gun is used. The experiments in section 4.4 and section 5.5 used a temporary replacement electron gun, since the gun that had been used for the experiments in section 5.4 had malfunctioned. An unfortunate consequence of a slight geometrical incompatibility, between the temporary replacement electron gun and the vacuum chamber (chapter 4,) was that low-energy electron diffraction and Auger electron spectroscopy measurements were not possible, while the temporary gun was in place; it was therefore necessary to rely on previous calibrations (sections 5.4, B,) for the kind of information that these techniques would have produced.

Both the temporary replacement electron gun, and the gun procured by the author's predecessors, are described in detail in their respective manuals [73, 74].

The Mott polarimeter is an unusual, and relatively novel, instrument, and with its measurements are associated particular systematic errors; there follow descriptions of these, and of some established experimental and mathematical techniques for eliminating them.

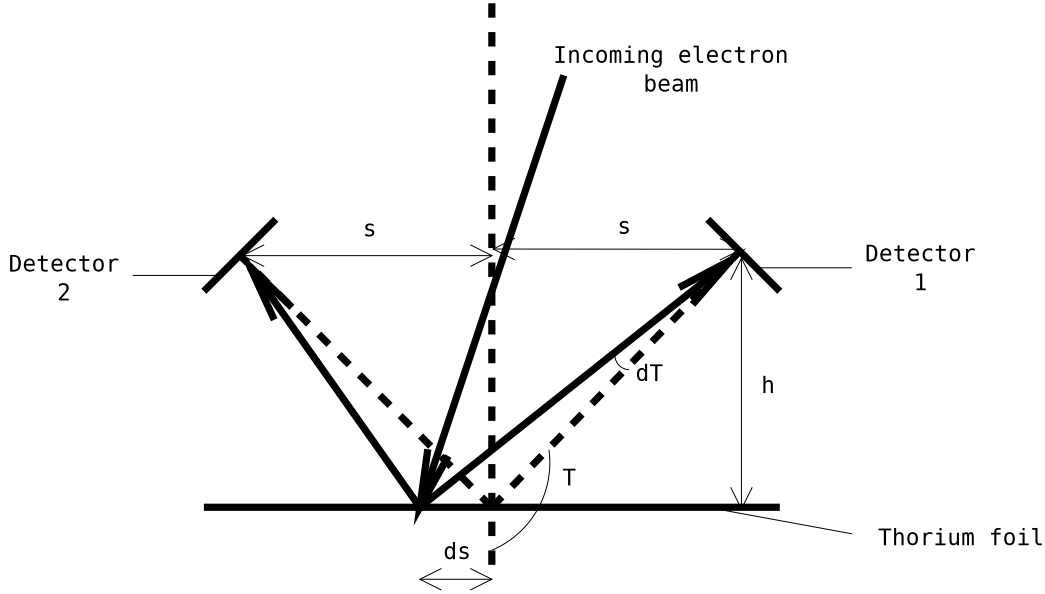


Figure 3.3: A Misaligned Incident Electron Beam. Based on a diagram by Gay & Dunning [5]

3.3 Systematic Errors Specific to Mott Polarimetry

Gay and Dunning [5] identify two sources of systematic error unique to Mott polarimeters:

- The incoming electron beam may be misaligned (figure 3.3.)
- The two detectors may have efficiencies η_1 and η_2 , which are less than unity. More crucially for asymmetry measurements (equation 3.6,) it may be that $\eta_1 \neq \eta_2$.

Gay & Dunning [5] show that each of these effects introduces a multiplicative relative systematic error in the electron arrival rate at one channeltron compared with that at the other, which invalidates the use of the raw asymmetry as a polarization indicator (equation 3.6.) A technique has been developed [5, 34] which allows the elimination of a systematic error of this nature. In this scenario, the rates of electron arrival R_{ij} on channeltrons $i = 1$ and $i = 2$ for beams of polarizations of equal magnitude $|P|$, in opposite

directions $j = \uparrow$ and $j = \downarrow$. The polarization is then given¹ by [5, 34]

$$P = \frac{\sqrt{R_{1\uparrow}R_{2\downarrow}} - \sqrt{R_{1\downarrow}R_{2\uparrow}}}{S(\sqrt{R_{1\uparrow}R_{2\downarrow}} + \sqrt{R_{1\downarrow}R_{2\uparrow}})}. \quad (3.7)$$

3.3.1 Derivation and Explanation of Equation 3.7

Why would one expect this formula to work? The underlying principle is the time-honoured one of making two measurements, in which the systematic error is of the same magnitude, but in opposite senses, then taking an average of the two measurements, to obtain a result free of systematic error. However, because the systematic errors under consideration here are multiplicative, rather than additive, “average” indicates geometric mean, rather than arithmetic mean. The application of this principle in the present case will now be examined in greater detail.

Let η_i be the sensitivity (quantum efficiency) of detector i . The two sources of multiplicative systematic error mentioned above can be defined as conditions where $\eta_1 \neq \eta_2$, and where $ds \neq 0$, where the misalignment ds is as defined in figure 3.3. The measured electron arrival rate at detector i , with incident polarization direction j , R_{ij} , is

$$R_{ij} = \eta_i Q_{ij}, \quad (3.8)$$

where Q_{ij} is the actual rate at which electrons arrive at the detector.

Let Θ_i be the solid angle subtended by detector i at the point where the electron beam strikes the thorium foil. The scattering probability per unit solid angle in the region of detector 1 is (equation 3.4) $\sigma_0(1 + SP_{\text{true}})$ for polarization direction \uparrow , and $\sigma_0(1 - SP_{\text{true}})$ for polarization direction \downarrow , and vice versa (equation 3.5) in the region of detector 2, i.e., if Q_0 is the rate at which electrons are incident on the thorium foil,

$$Q_{1\uparrow} = Q_0 \sigma_0 (1 + SP_{\text{true}}) \Theta_1, \quad (3.9)$$

¹In real experiments, the values of $R_{1\uparrow}$, $R_{1\downarrow}$, $R_{2\uparrow}$, and $R_{2\downarrow}$ are not perfectly specified, but are subject to significant random errors. In this case, the polarization obtained from equation 3.7 becomes an estimator; a given measurement will provide a polarization value, via the formula, which will not always be equal to the true value of the polarization, but whose value will be drawn from some probability distribution $P(P_{\text{formula}}|P_{\text{true}})$ about the true value. Frequentist statisticians might wish to ask whether it is an unbiased estimator, i.e. whether the expectation of this probability distribution is equal to P_{true} . An answer could be particularly difficult to derive, given the non-linearity of P_{formula} in the directly measured electron arrival rates. Bayesian statisticians might prefer to abandon the estimator, and think in terms of the simpler forward probability distribution $P(R_{1\uparrow}, R_{1\downarrow}, R_{2\uparrow}, R_{2\downarrow}|R_0, P_{\text{true}})$, using Bayes’ theorem to invert it to $P(R_0, P_{\text{true}}|R_{1\uparrow}, R_{1\downarrow}, R_{2\uparrow}, R_{2\downarrow})$

3.3. SYSTEMATIC ERRORS SPECIFIC TO MOTT POLARIMETRY 87

$$Q_{1\downarrow} = Q_0\sigma_0(1 - SP_{\text{true}})\Theta_1, \quad (3.10)$$

$$Q_{2\uparrow} = Q_0\sigma_0(1 - SP_{\text{true}})\Theta_2, \quad (3.11)$$

and

$$Q_{2\downarrow} = Q_0\sigma_0(1 + SP_{\text{true}})\Theta_2. \quad (3.12)$$

Therefore,

$$R_{1\uparrow} = Q_0\sigma_0(1 + SP_{\text{true}})\Theta_1\eta_1, \quad (3.13)$$

$$R_{1\downarrow} = Q_0\sigma_0(1 - SP_{\text{true}})\Theta_1\eta_1, \quad (3.14)$$

$$R_{2\uparrow} = Q_0\sigma_0(1 - SP_{\text{true}})\Theta_2\eta_2, \quad (3.15)$$

and

$$R_{2\downarrow} = Q_0\sigma_0(1 + SP_{\text{true}})\Theta_2\eta_2. \quad (3.16)$$

If A is the cross-sectional area of a detector,

$$\begin{aligned} \Theta_1 &= \frac{A}{r_1^2} \\ &= \frac{A}{(s + ds)^2 + h^2} \\ &= \frac{A}{s^2 + h^2} \left(1 + \frac{2sds + ds^2}{s^2 + h^2} \right)^{-1} \\ &\approx \frac{A}{s^2 + h^2} \left(1 - \frac{2sds}{s^2 + h^2} \right), \end{aligned} \quad (3.17)$$

where $|ds| \ll \frac{1}{2s(s^2+h^2)}$. Similarly,

$$\Theta_2 \approx \frac{A}{s^2 + h^2} \left(1 + \frac{2sds}{s^2 + h^2} \right). \quad (3.18)$$

Some cumbersome notation can be avoided by defining $\Theta_0 = \frac{A}{s^2+h^2}$ and $d\Theta = \frac{2s\Theta_0 ds}{s^2+h^2}$. Then

$$\Theta_1 = \Theta_0 - d\Theta, \quad (3.19)$$

and

$$\Theta_2 = \Theta_0 + d\Theta. \quad (3.20)$$

The polarization obtained from equation 3.7, in the absence of random errors, is therefore,

$$P_{\text{formula}} = \frac{\sqrt{R_{1\uparrow}R_{2\downarrow}} - \sqrt{R_{1\downarrow}R_{2\uparrow}}}{S(\sqrt{R_{1\uparrow}R_{2\downarrow}} + \sqrt{R_{1\downarrow}R_{2\uparrow}})}$$

$$\begin{aligned}
&= \left(\sqrt{Q_0^2 \sigma_0^2 (1 + SP_{\text{true}})^2 \eta_1 \eta_2 (\Theta_0 + d\Theta)(\Theta_0 - d\Theta)} \right. \\
&\quad \left. - \sqrt{Q_0^2 \sigma_0^2 (1 - SP_{\text{true}})^2 \eta_1 \eta_2 (\Theta_0 + d\Theta)(\Theta_0 - d\Theta)} \right) \\
&\quad / \left(\sqrt{Q_0^2 \sigma_0^2 (1 + SP_{\text{true}})^2 \eta_1 \eta_2 (\Theta_0 + d\Theta)(\Theta_0 - d\Theta)} \right. \\
&\quad \left. + \sqrt{Q_0^2 \sigma_0^2 (1 - SP_{\text{true}})^2 \eta_1 \eta_2 (\Theta_0 + d\Theta)(\Theta_0 - d\Theta)} \right) \\
&= P_{\text{true}}. \tag{3.21}
\end{aligned}$$

3.4 Additive Offsets

Some systematic errors, instead of taking the form of a constant ratio of measurements to true values, take the form of a constant difference between measurements and true values; these systematic errors are additive, not multiplicative. During the experiments presented in this thesis, the apparent electron arrival rates (chapter 5) at the detectors, with the electron gun switched off, and the conditions otherwise the same as in the real experiments, were occasionally checked. These rates should indicate the size of any additive systematic error. They were found to be of the order of 1 Hz, which is much smaller than the measured rates with the electron gun on. Additive systematic errors are, therefore, not believed to be significant here.

3.5 Drift Effects

An empirically-based discussion of the possible effects of drift, in the experiments presented in this thesis, can be found in section 5.5. The measures taken to counter these effects are discussed in section 4.4.3, and appendices A.2.1, and A.2.2.

Part III

Polarized Electron Reflection Study of $Co/Cu(001)$

Chapter 4

The Vacuum Chamber, Attached Equipment for Vacuum Maintenance and Sample Production, and Experimental Method

All of the experiments described in this thesis took place within a vacuum chamber (figures 4.1, 4.2, 4.4.) The technological principles of the vacuum maintenance equipment are described in detail in *Ultrahigh Vacuum Practice* [9], with useful additional information in “vacuum technology” [75]. The central portion of the vacuum chamber, in which the sample holder (figure 4.5) is situated, is [37] constructed from μ -metal, in order to screen out external magnetic fields, while most of the peripheral portions are constructed from stainless steel. During the experiment described in part III, the chamber, and associated equipment, maintained the gas pressure to which the sample was exposed, at all times other than during argon ion sputtering, below $(22 \pm 0.29) \times 10^{-9}$ mbar, with a base pressure of $(140 \pm 2.9) \times 10^{-12}$ mbar.

There follow more detailed descriptions of the apparatus for sample preparation, attached to the vacuum chamber.

4.1 Sample Holder

The copper crystal, which forms the basis of the samples, is held in the vacuum chamber (figures 4.1, 4.2) on a sample holder (figure 4.5.) This sample holder provides the facility for moving the sample, with two rotational de-

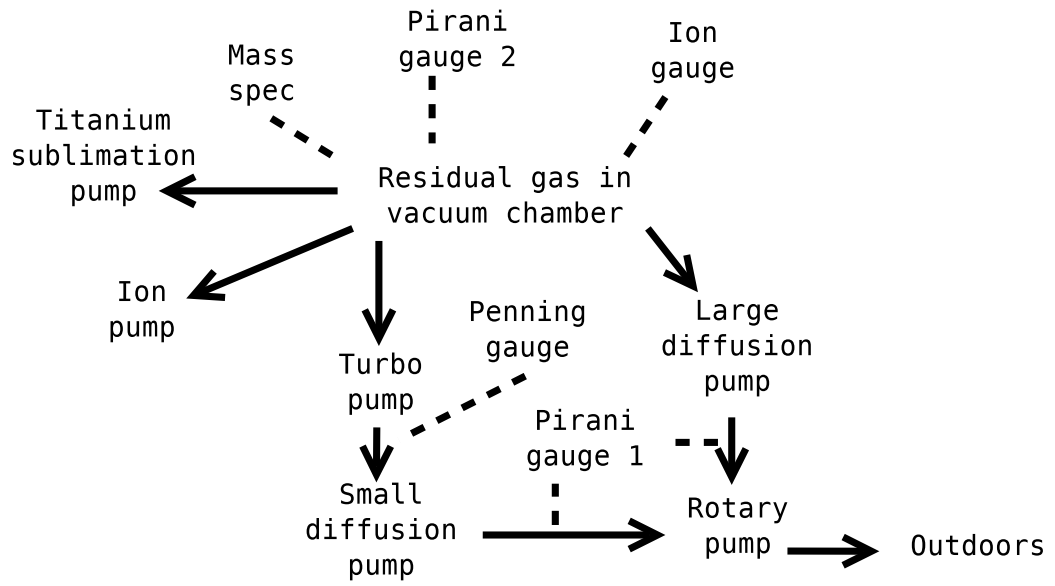


Figure 4.1: A Schematic Diagram of the Pumps and Pressure Measurement Apparatus Connected to the Ultra-High Vacuum (UHV) Chamber, inside Which the Experiments Were Conducted; Arrows Represent Flows of Gas, and Broken Lines Represent Pressure Measurements; Pirani Gauges Measure Total Pressure in a High-Pressure Range between 4×10^{-2} mbar and 5 mbar, the Penning Gauge Measures Total Pressure in an Intermediate Range, and the Ion Gauge Measures Total Pressure in a Low-Pressure Range between 8×10^{-11} mbar and 10^{-5} mbar; the Mass Spec Measures Total Pressure, and the Partial Pressures of Individual Gas Species.

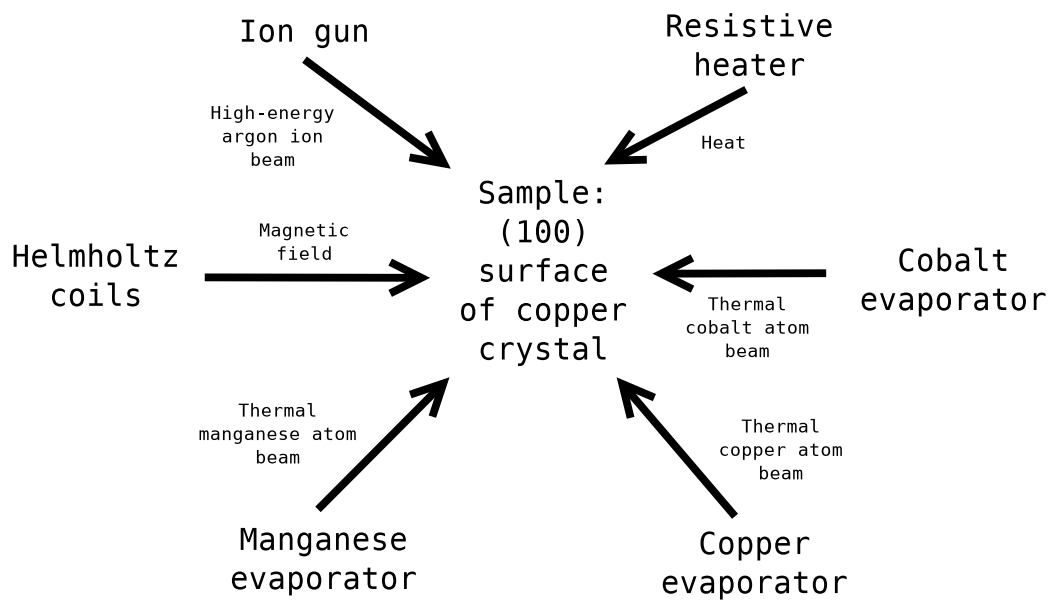


Figure 4.2: A Schematic Diagram of the Equipment for Preparing the Sample, Contained in the UHV Chamber; Each Arrow Represents a Flow of Matter or Energy, Described alongside the Arrow, from an Item of Equipment to the Sample, Designed to Alter the Sample in a Manner Described Later in This Chapter.

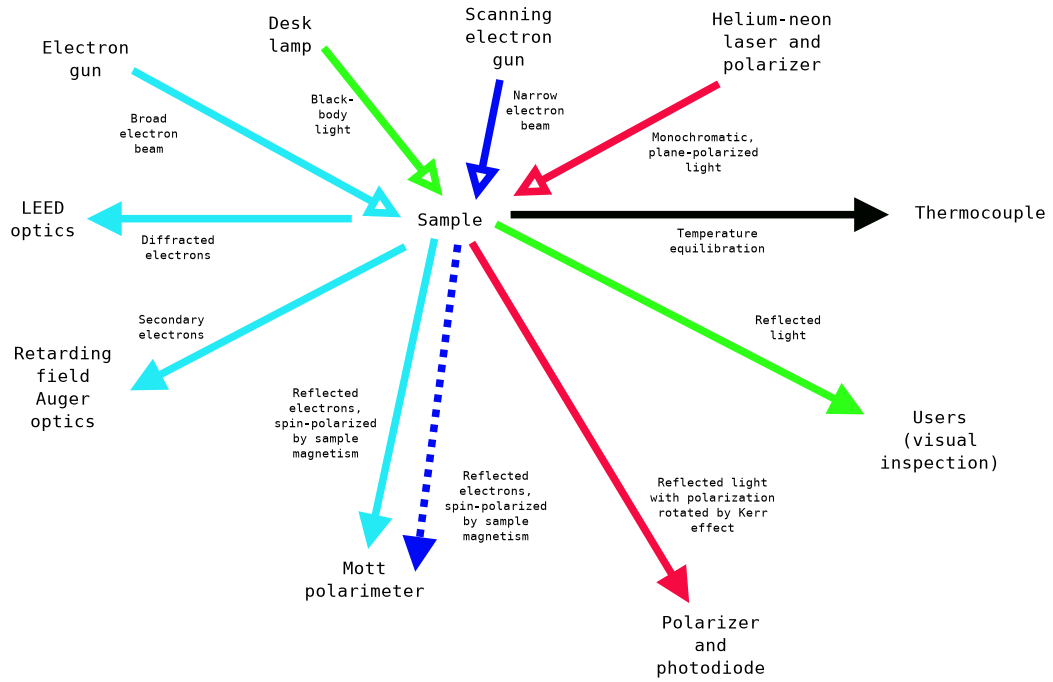


Figure 4.3: A Schematic Diagram of the Equipment for Measuring or Observing Characteristics of the Sample; Arrows with Hollow Heads Represent Flows of Matter or Energy into the Sample, Used To Illuminate or Excite the Sample, To Render a Measurement Possible; Arrows with Filled Heads Represent Information-Carrying Flows of Matter out of The Sample; where the Arrow Is Solid, the Experiment It Represents Has Been Successfully Undertaken in This UHV Chamber; where the Arrow Is Broken, the Experiment Is a Future Possibility; Arrows of the Same Colour All Relate to the Same Illumination or Excitation of the Sample.

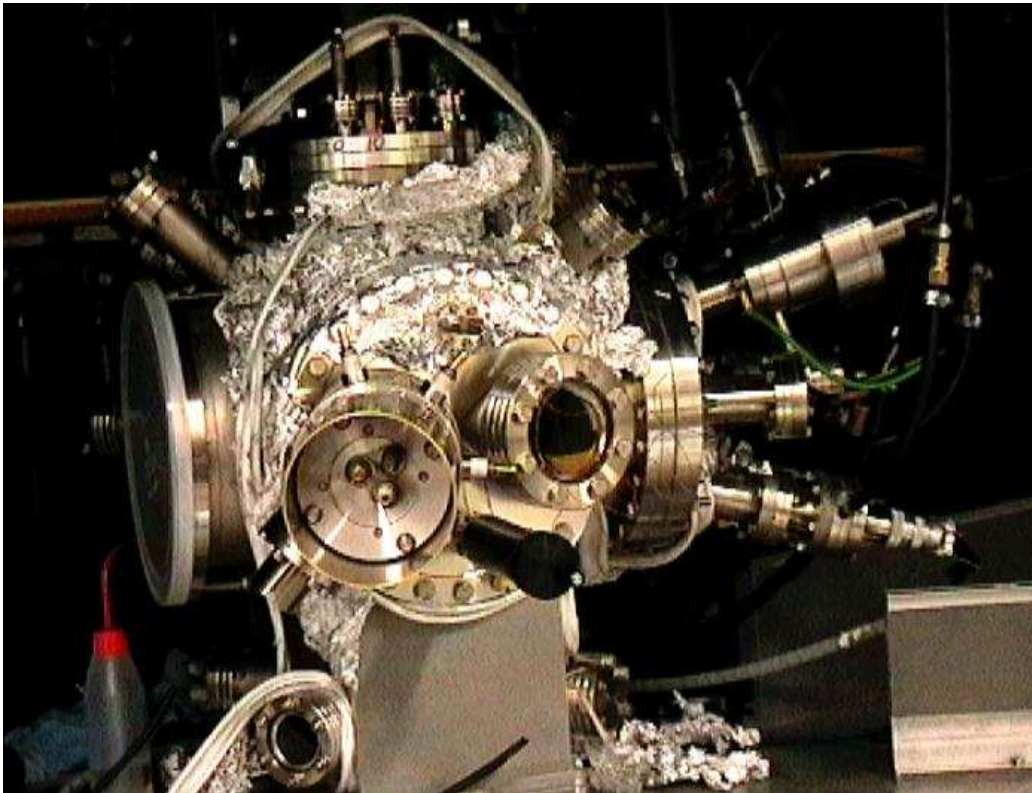


Figure 4.4: A Photograph of the UHV Chamber, inside Which the Experiments Were Conducted

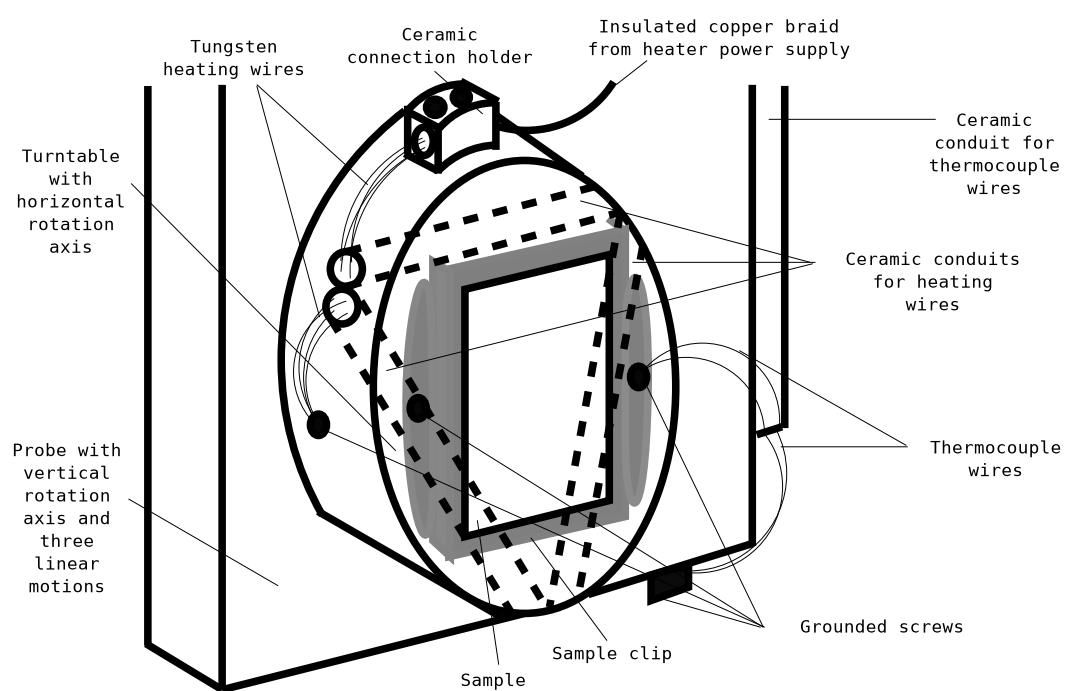


Figure 4.5: The Sample Holder

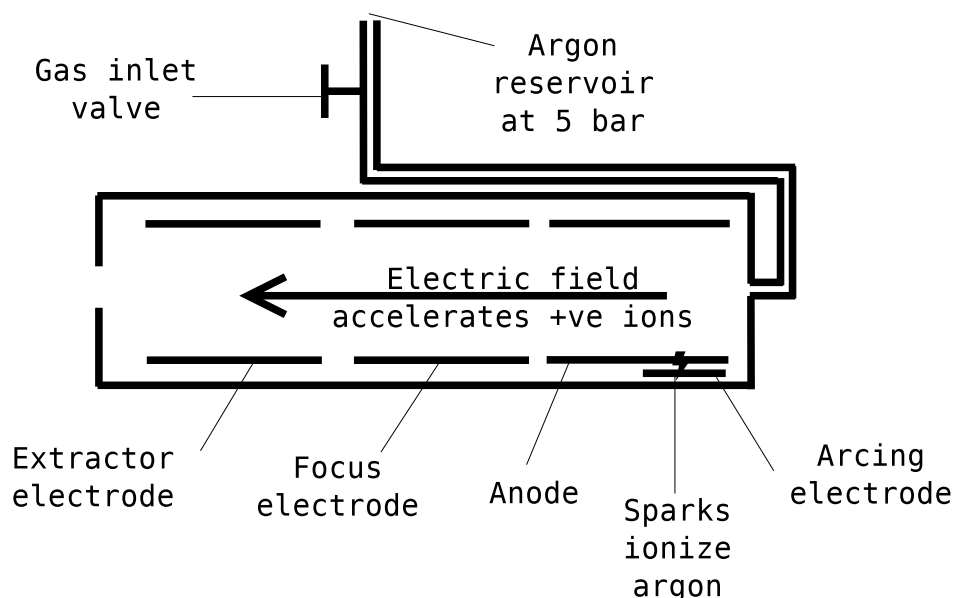


Figure 4.6: Schematic Diagram of the Argon Ion Sputtering Gun

degrees of freedom, and three translational degrees of freedom. It also provides heating for the sample, by means of the power developed when a current is passed through the finite Ohmic resistance of the heating wires, and measurement of the temperature of the sample, and of a point slightly removed in space from the sample, by means of the two thermocouples.

4.2 Argon Ion Sputtering Gun

The chamber (figure 4.2) contains an argon ion sputtering gun, for use in cleaning the surface of the copper crystal. The principles of this device are shown in figure 4.6. The argon ion beam has a cleaning effect on the sample surface by removing a surface layer. The surface layer removal proceeds [76] by surface atoms and molecules, which are struck by argon ions, recoiling into the bulk of the sample. The elastic response of the bulk of the sample then expels the surface atoms and molecules.

As well as removing surface impurities, the author expects the sputtering process to have removed the surface layer of amorphous copper, which is [77] likely to have formed during the polishing of the surface that took place, when the copper crystal was temporarily removed from the vacuum chamber, between the experiments in section 5.4 and those in section 5.5.

The gun was purchased commercially by the author's predecessors, and

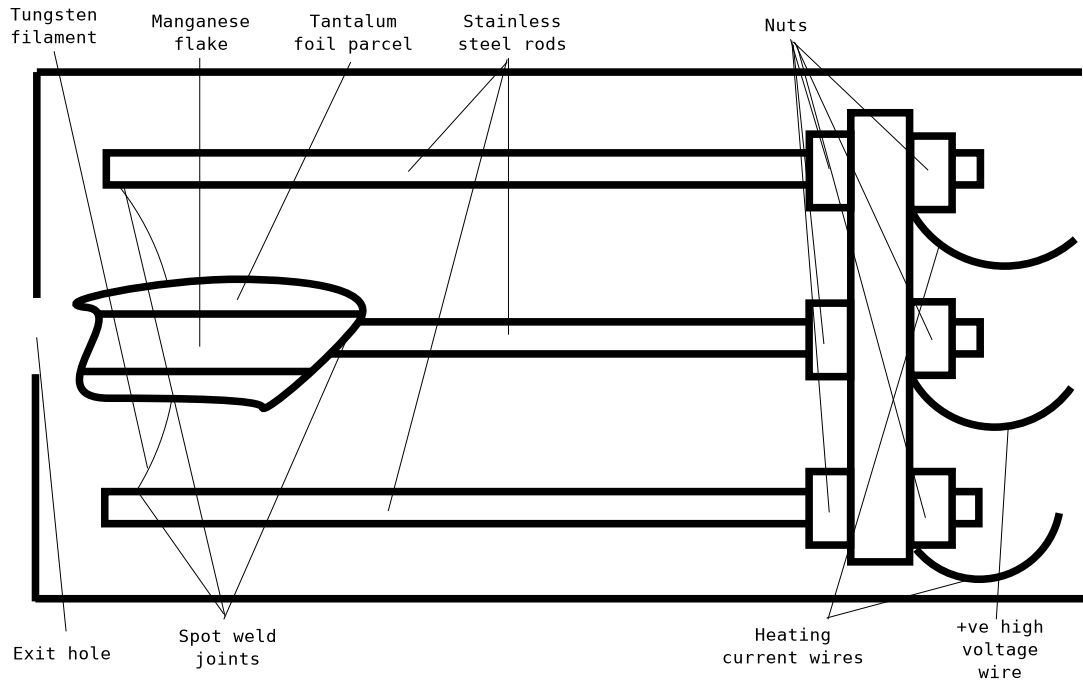


Figure 4.7: Schematic Diagram of the Manganese Evaporator

is described in more detail in its manual [78].

4.3 Electron-Beam Evaporators

Three electron-beam evaporators, for depositing cobalt, manganese, and copper on the sample, are present in the vacuum chamber (figure 4.2.) Figure 4.7 shows the manganese evaporator. This was chosen as the example evaporator, because the author is more familiar with it than with the other two, having dismantled it to replace the manganese charge and the cathode filament.

The heat generated by the current flowing in the cathode filament excites electrons to leave the filament. These are accelerated, by the electric field, into the manganese (or cobalt or copper) charge, where their kinetic energy is deposited as heat. This evaporates some of the manganese, producing a gas of manganese atoms and ions. Those that effuse from the exit hole are all travelling in roughly the same direction, and therefore form an atom beam, which, if it strikes the sample surface, deposits [79] a film of manganese on that surface.

The manganese and copper evaporators were both constructed by the author's predecessors, and are of very similar design. The cobalt evaporator, while working on the same principle, was purchased commercially by the author's predecessors, and has the important addition of a current collector, near its exit hole, which measures the flux of ions, and therefore of atoms, leaving the exit hole. This is taken to be a measurement of the rate of cobalt deposition on the sample.

The cobalt evaporator is described in more detail in its manual [80].

Having described the vacuum chamber, and associated sample preparation equipment, it is now time to present the methods by which this equipment was used, in the experiments whose results are presented later in this thesis.

4.4 Method

The purpose of this procedure is to measure the intensity and polarization of the specularly reflected electron beam from $Co/Cu(001)$, as a function of cobalt thickness, incident electron energy, and incident electron beam current. This description of the procedure has been constructed in a modular way, in the sense that a broad-brush view of the procedure is given, with references to later sections, which give finer details of each step; there are several levels of detail. This section has been constructed in this unusual fashion, because the author, aware of the general view that best practice in computer programming is to arrange the instructions, which describe what is to be done, in this fashion, is keen to investigate whether the same principle applies to natural-language descriptions of what has been done. Some of the very fine details are to be found in an appendix (appendix A.)

1. The one of the two rotational motion drivers (section 4.1,) which had a horizontal axis of rotation, perpendicular to the surface of the (001) copper crystal, was used to orient the [100] axis of the crystal vertically within 5° , using visual inspection and a previous identification, by low-energy electron diffraction, of the orientation of the crystalline axes relative to the crystal's cut faces.
2. The (001) copper crystal (section 4.1,) was cleaned in an ultra-high vacuum chamber (figure 4.2,) according to the procedure in section 4.4.1, eight times. The reasons for choosing eight as the number of cycles are discussed in section 5.4. The resulting clean, well-ordered copper surface was named "substrate 9," to continue the numbering sequence used in preliminary experiments (sections 5.4, 5.5.)

3. Polarized electron reflection measurements were conducted, according to the procedure in section 4.4.3.
4. Cobalt was added to the sample, and the resulting film subjected to a series of polarized electron reflection measurements, according to the procedure in section 4.4.2, seven times.

4.4.1 Procedure for Cleaning the $Cu(001)$ Surface

The purpose of this procedure is to produce a sample surface which is free of contaminants, and has a well-ordered crystalline structure.

1. The vacuum chamber's ion pump (figure 4.1) was isolated from the chamber using a gate valve, and switched off, to protect the pump from saturation with argon.
2. The sample was placed, according to the procedure in appendix A.1, in a position which had previously been determined as being in the path of the ion beam from a commercial argon ion sputtering gun (section 4.2,) with the sample's exposed (001) face toward the gun.
3. The ion energy from the ion gun was set to (2.8 ± 0.029) keV.
4. The gas inlet valve of the ion gun was opened until the pressure in the chamber, as revealed by the ion gauge (figure 4.1,) was (875 ± 110) pbar.
5. On some occasions, a visual check was made for a blue glow at the sample surface, which would confirm that the ion beam was reaching the surface.
6. The sputtering process was allowed to continue for (59 ± 9) minutes.
7. The gas inlet valve of the ion gun was closed.
8. The power supply that provided the ion energy was switched off.
9. When the pressure in the chamber, as revealed by the ion gauge (figure 4.1,) had dropped to less than 1 pbar, the ion pump was switched on.
10. The valve between the ion pump and the chamber was opened, and the ion pump was switched on.
11. A current of (8.75 ± 0.04) A, through the sample heating filament (figure 4.5,) was switched on.

12. When the sample temperature, as revealed by the sample thermocouple, exceeded 773 K, the current through the sample heating filament was switched off.

4.4.2 Procedure for Adding Cobalt to the Sample Surface and Conducting Polarized Electron Reflection Measurements

1. The sample was placed, according to the procedure in appendix A.1, in a position that had previously been determined, by observation of the resulting film with Auger electron spectroscopy [81, 82, 83] (sections 5.4, B), to lead to cobalt adsorption from a commercial electron-beam evaporator (section 4.3), with respect to the translational dimensions, and 180° from that position, with respect to rotation about a vertical axis.
2. The cobalt evaporator was switched on, and adjusted to give a flux monitor current I_{mon} of ~ 30 nA; a value of I_{mon} with a quantitative precision estimate was recorded.
3. The sample was placed, according to the procedure in appendix A.1, into the position for cobalt adsorption, with respect to all degrees of freedom.
4. The shutter at the front of the evaporator was opened.
5. Cobalt was allowed to be adsorbed for a time T of ~ 1 ks; a value of T with a precision estimate was recorded.
6. The shutter at the front of the evaporator was closed.
7. The evaporator was switched off.
8. Polarized electron reflection measurements were conducted, according to the procedure in section 4.4.3.

4.4.3 Procedure for Conducting Polarized Electron Reflection Measurements on One Film

The purpose of this procedure is to examine the sample's magnetic properties with each of two opposite magnetization directions, with the order in which the magnetizations are examined varying, to protect against drift effects.

1. The vacuum chamber's ion pump (figure 4.1) was isolated from the chamber using a gate valve, and switched off, to protect the polarimeter from noise from the ion pump.
2. The vacuum chamber's ion gauge (figure 4.1) was switched off, to protect the polarimeter from noise from the ion gauge.
3. The sample was magnetized, according to the procedure in appendix A.2. If the procedure being described here had been performed previously, then the direction chosen for the magnetization was opposite to that chosen, at the same stage, in the preceding performance of this procedure. Otherwise, a direction was chosen at random.
4. Polarized electron reflection measurements, as a function of incident electron energy and incident beam current, were taken, according to the procedure in appendix A.2.1.
5. The sample was magnetized, according to the procedure in appendix A.2, in the opposite direction from that chosen at the earlier stage in this procedure.
6. Polarized electron reflection measurements were taken, according to the procedure in appendix A.2.1.
7. The ion gauge was switched on.
8. The ion pump was switched on.
9. The valve between the ion pump and the chamber was opened.

Chapter 5

Results and Discussion

There follow measurements, using a reflected electron beam from several cobalt thicknesses, of the electron arrival rates at the two detectors of the Mott polarimeter. The measurement run for each cobalt thickness took place over a period of approximately 2 hours, the total duration of the experiments being 5 days. The measurements were made at room temperature.

The recorded ion fluxes and durations of the cobalt growth sessions are presented in table 5.1.

Examples of the recorded electron detection rates at the channeltrons are presented in figures 5.1 and 5.2. Each point in the graphs represents a rate taken as the quotient of the number of electrons counted in the time period 256τ , in the relevant conditions, and 256τ . The quoted uncertainty in the detection rate is the standard deviation of the Poisson distribution [84]. In addition to these points, theoretical curves are shown. These represent the new theory of chapter 2, as expanded to take account of instrumental characteristics, by the main model of section 5.3. For the purposes of the curves in this chapter, the parameters are chosen, using the Marquardt-Levenberg algorithm, for the best possible fit to the data. The parameters affect the goodness of fit, through three parameter combinations, each of which includes a mixture of characteristics of the sample and of the instrument. The most interesting of these combinations, by virtue of being free of un-calibrated instrumental characteristics, is the Mott asymmetry $SP = -\frac{4Se^2\hbar m_e V_1 B_1}{12e^2 m_e^2 V_1^2 + e^2 \hbar^2 B_1^2}$, which represents the balance between the electric potential V_1 and the Weiss field B_1 , inside the sample. The best-fit values of the Mott asymmetry, for each film thickness, are set out in table 5.2. From a visual inspection of published calibration data (figure 5.7,) the Sherman function is $S \approx -0.23$.

The full data set consists of twenty-four graphs like the two shown, representing three incident beam currents, at each of eight film thicknesses. Readers who would prefer to see the full data set, rather than just examples,

Thickness index j	I_{mon}/nA	T/s	Added thickness $t'/\mu\text{A s}$	Cumulative thickness $t/\mu\text{A s}$	t/nm
0	0	0	0	0	0
1	30 ± 2	1097.2 ± 3	32.9 ± 2.2	32.9 ± 2.2	2.57 ± 0.36
2	30 ± 0.5	958.3 ± 3	28.75 ± 0.49	61.7 ± 2.2	4.81 ± 0.68
3	32.5 ± 2.5	1012.6 ± 3	32.9 ± 2.5	94.6 ± 3.4	7.4 ± 1
4	32 ± 1.5	1022.4 ± 3	32.7 ± 1.5	127.3 ± 3.7	9.9 ± 1.4
5	30.5 ± 2	1023.9 ± 3	31.2 ± 2	158.5 ± 4.2	12.4 ± 1.7
6	28.3 ± 2	1085.2 ± 3	30.7 ± 2.2	189.2 ± 4.8	14.8 ± 2.1
7	29 ± 0.29	1022.2 ± 3	29.64 ± 0.31	218.8 ± 4.8	17.1 ± 2.4

Table 5.1: Recorded Cobalt Growth Conditions for the Films on Substrate 8. Thicknesses in nm Are Based on the Calibration in Appendix B

Film Thickness Index	Film Thickness t / nm	Best-Fit Mott Asymmetry
1	2.57 ± 0.36	0.014
2	4.81 ± 0.68	-0.004
3	7.4 ± 1	-0.0044
4	9.9 ± 1.4	0.011
5	12.4 ± 1.7	0.014
6	14.8 ± 2.1	0.003
7	17.1 ± 2.4	0.024

Table 5.2: The Best Fit Values of the Mott Asymmetry $SP = -\frac{4Se^2\hbar m_e V_1 B_1}{12e^2 m_e^2 V_1^2 + e^2 \hbar^2 B_1^2}$

might like to down-load the transparent copy of this thesis, and check out RCS version 18.1.

Having presented the data in raw form, it is time to analyse and process it in a variety of ways. There follow comments on a visual inspection of the data, and estimates of the Mott asymmetries (and therefore of the reflected beam spin polarizations) obtained in the experiments.

5.1 Visual Inspection of the Data

For any given film thickness, incident beam current, and channeltron, I find that the most salient visual feature of the data (chapter 5) is the sign of the gradient of each electron arrival rate against beam energy curve: the electron arrival rate decreases with increasing energy. The second most salient feature is the sign of the curvature of each curve: the graph is convex \cup . This shape is as one would expect from equation 2.10, which is derived from the new theory in chapter 2.

The third most salient visual feature of the data is the direction, in which the electron arrival rate, for the majority of beam energies, changes on moving from magnetization up to magnetization down¹. My visual estimates of this direction are presented in table 5.3.

This distribution of changes in electron arrival rate is interesting, because, from the new theory in chapter 2, and indeed from any theory, in which the process of changing the magnetization direction affects the arrival rates at the channeltrons only through the reflected electron beam's spin polarization, one would expect the changes in the two channeltrons' arrival rates, on reversing the magnetization direction, to be opposite. This has (table 5.3) been the

¹This, of course, may be a move either forward or backward in time

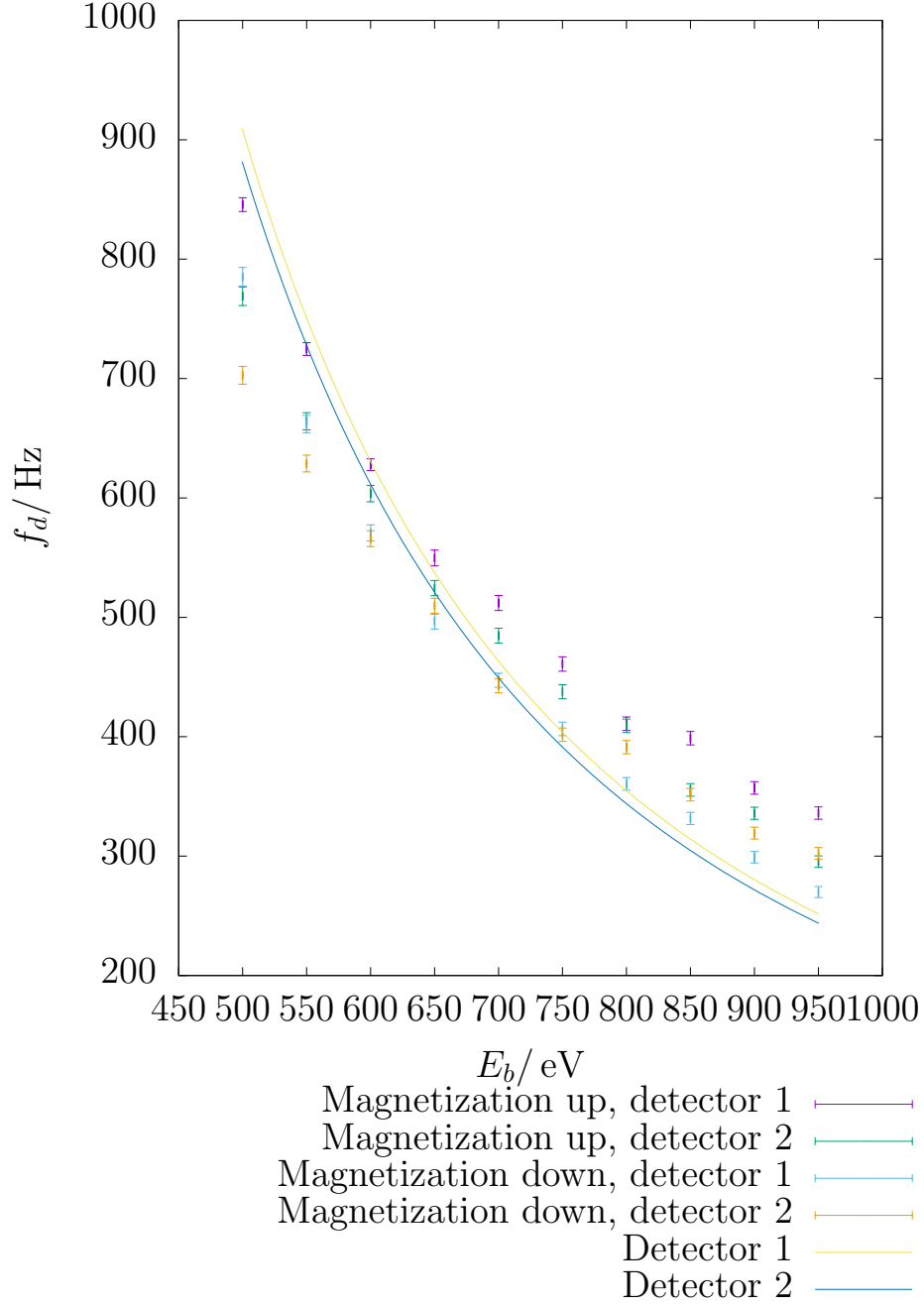


Figure 5.1: Measured Electron Arrival Rate (Points with Error-Bars) at Detectors against Incident Beam Energy for an Incident Beam Current of $(6 \pm 0.1) \mu\text{A}$, Both Sample Magnetization Directions, and substrate 9 with No Film, and Corresponding Predictions from the New, Classical-Field Theory of Chapter 2 (Lines.)

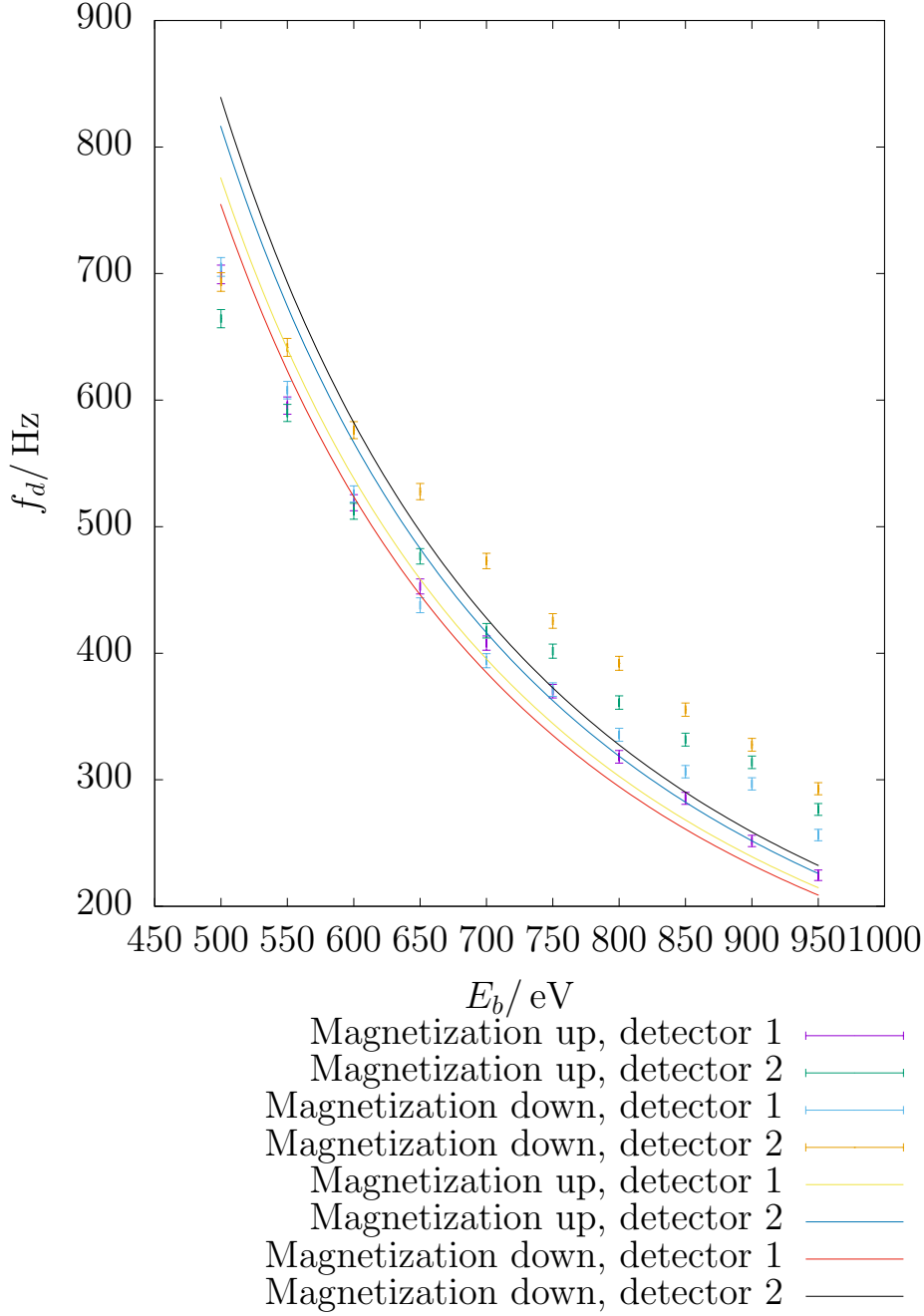


Figure 5.2: Measured Electron Arrival Rate (Points with Error-Bars) at Detectors against Incident Beam Energy for an Incident Beam Current of $(6 \pm 0.1) \mu\text{A}$, Both Sample Magnetization Directions, and Thickness 5 $((12.4 \pm 1.7) \text{ nm})$ on substrate 9, and Corresponding Predictions from the New, Classical-Field Theory of Chapter 2 (Lines.)

Film thickness	$I_b/\mu\text{A}$	Channeltron 1 Direction	Channeltron 2 Direction
0	2 ± 0.1	Down	Down
0	4 ± 0.1	Down	Down
0	6 ± 0.1	Down	Down
1	2 ± 0.1	Down	Down
1	4 ± 0.1	Down	Down
1	6 ± 0.1	Down	Down
2	2 ± 0.1	Up	Up
2	4 ± 0.1	Up	Up
2	6 ± 0.1	Up	Up
3	2 ± 0.1	Down	Down
3	4 ± 0.1	Down	Down
3	6 ± 0.1	Down	Down
4	2 ± 0.1	Down	Down
4	4 ± 0.1	Down	Down
4	6 ± 0.1	Down	Down
5	2 ± 0.1	Down	Up
5	4 ± 0.1	Up	Up
5	6 ± 0.1	Up	Up
6	2 ± 0.1	Down	Down
6	4 ± 0.1	Down	Down
6	6 ± 0.1	Down	Down
7	2 ± 0.1	Up	Up
7	4 ± 0.1	Up	Up
7	6 ± 0.1	Up	Up

Table 5.3: Visually Estimated Directions, in Which the Electron Arrival Rates Change on Moving from Magnetization up to Magnetization down

case in only one of the twenty-four sets of conditions of film thickness and beam current measured.

It is suggested that, in terms of the diagrammatic view of the scientific method presented in “Bayesian Interpolation” [85], and in “Bayesian Methods for Adaptive Models” [52], this section, unlike the rest of this chapter, belongs to the ‘decide whether to create new models,’ stage, rather than to the ‘assign preferences to the alternative models’ stage². Only some qualitative pointers to theories that *might* better match the contents of table 5.3 will be provided; the construction of enough quantitative detail to permit testing of new theories, in the light of data, will be left as an exercise for any reader who wishes to undertake it.

The author suggests three possible forms for new theories, in the light of table 5.3.

1. The precision of the positioning of the sample may be insufficient to prevent variation, of the kind observed in section 5.4, in the acceptance probability at the front of the polarimeter (the a of appendix 5.3.2.) In support of this explanation, it is noted that, since the position of the sample is only reset on changes of magnetization or of film thickness, one would expect, if it were the correct explanation, that the direction of change of the count rate would be independent of channeltron number and beam current, depending only on film thickness, as is (table 5.3) indeed observed in almost all cases. However, there are two strong arguments against this explanation. Firstly, the precision with which the sample was positioned was chosen on the basis of empirical evidence (section 5.4) about the precision needed to prevent this effect. Secondly, the overall proportions of “up” and “down” directions of change of electron arrival rate, on magnetization reversal, are (table 5.3) unequal, by an amount that, depending on the details of the explanation, may be statistically significant, and militate against any explanation that does not involve a true magnetic effect.
2. The experiment may not be performed quickly enough to prevent drift effects, of the kind observed in section 5.5 between the measurements for different magnetization directions on the same film thickness³, or the drift effects may be related to switching on and off the channeltron, rather than to a particular time-scale. In support of this explanation,

²Visual impressions have [86] also been used in this way in atmospheric science.

³Drift effects on the longer time-scale between measurements on different film thicknesses would not produce the effect that needs to be explained, and are modelled within appendix 5.3.2.

it is noted that, as long as the drift effects relate to switching on and off the channeltrons, which occurs only at changes of magnetization direction or film thickness, one would expect, if it were the correct explanation, that the direction of change of the count rate would be independent of channeltron number and beam current, depending only on film thickness, as is (table 5.3) indeed observed in almost all cases. However, there are three strong arguments against this explanation. Firstly, the speed, with which the experiments were performed, was chosen on the basis of empirical evidence (section 5.5) about the speed needed to prevent drift effects; of course, this argument does not apply, if the drift effects relate to switching on and off the channeltrons, rather than to a particular time-scale. Secondly, the overall proportions of “up” and “down” directions of change of electron arrival rate, on magnetization reversal, are (table 5.3) unequal, by an amount that, depending on the details of the explanation, may be statistically significant, and militate against any explanation that does not involve a true magnetic effect. Thirdly, if this explanation is correct, and the drift effects relate to a particular time-scale, rather than to switching on and off the channeltrons, then, given that the time-scale for changing channeltrons is only a factor of ~ 2 shorter than that for reversing magnetization direction, one would not expect the observed (table 5.3) high degree of independence of channeltron number, in the direction of change of the electron arrival rate.

3. A stray magnetic field, either from the sample itself, or from some ferromagnetic part of the sample holder (figure 4.5,) may be deflecting the electron beam in such a way as to change the acceptance probability at the front of the polarimeter (the a of appendix 5.3.2.) In support of this explanation, it is noted that one would expect, if it were the correct explanation:
 - that the direction of change of the count rate would be independent of channeltron number and beam current, depending only on film thickness, as is (table 5.3) indeed observed in almost all cases, and
 - in contrast to any effects that are not genuinely magnetic, that the overall proportions of “up” and “down” directions of change of electron arrival rate, on magnetization reversal, would be unequal, as they are (table 5.3,) by an amount that, depending on the details of the explanation, may be statistically significant.

If more quantitative theories are constructed, based on the first two ex-

planations, they would be expected to have significantly more adjustable parameters than the models in appendix 5.3.2, and therefore to take a prohibitive amount of CPU time to fit to the data using a Monte Carlo method. With reluctance, because it would have the consequence of ignoring evidence, which is relevant to a problem of parameter estimation and model comparison under consideration, long-term⁴, it might, therefore, be necessary to set aside the existing experimental results (chapter 5,) and instead assess the existing models (chapter 2, appendix 5.3.2,) in the light of future experimental results, with the experimental method adapted to position the sample more precisely, to be quicker, or to avoid switching on and off the channeltrons.

However, if more quantitative theories are constructed, based on the, apparently more plausible, third explanation, they will provide an exciting possibility for using electron beams to probe magnetic surfaces, without relying on spin polarization effects. The data in chapter 5 would be immediately suitable for use in this process, but future experimental data could be gathered without the practical difficulties involved in Mott polarimetry. If, despite this, demand for measurements of the spin polarization of reflected beams continues to exist, it may be worthwhile to know that Lind [65] discovered that the stray field around a sample could be substantially reduced, by briefly applying a magnetic field, smaller than that used to magnetize the sample and in the opposite direction, after the sample was magnetized.

It is also, of course, possible that the future of magnetism measurements with electron beams will take a course that the author has not foreseen; either one for which the measurements in chapter 5 are useful, or one for which they are not useful.

In passing, it is noted that although the author is familiar with several examples (section 2.10) [1, 4, 62, 63, 64, 25, 65, 26, 51] of published data, obtained using Mott polarimeters, on the spin polarization of reflected, diffracted, transmitted, inelastic, and secondary electron beams from magnetic and non-magnetic materials, these all present the data in a processed form, similar to that of section 5.2, rather than in the raw form of chapter 5. This is understandable, given the length constraints of papers in collections, journal articles, and theses, but regrettably, renders it impossible to apply reasoning of the kind above to these data.

Although the primary purpose of this section was to make qualitative suggestions, it will probably be useful to make a quantitative estimate of the deflection that a stray magnetic field produces, in a reflected electron beam (figure 5.3,) as a check on the plausibility of this suggestion.

The classical equations of motion of an electron, in a stray magnetic flux

⁴The author has made some comments elsewhere [10] on how this situation arises.

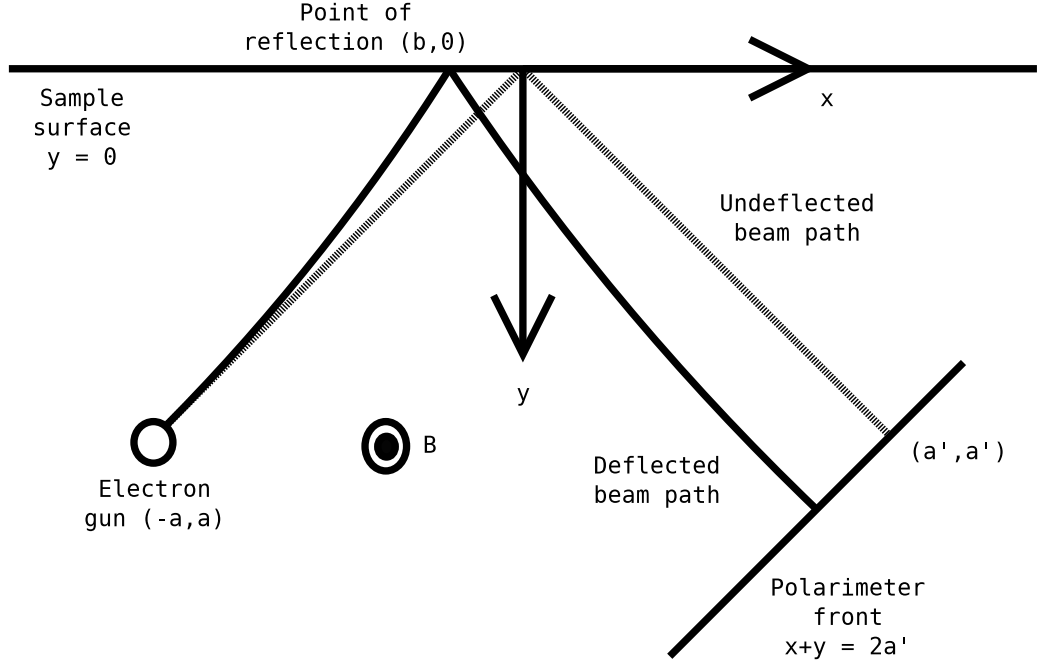


Figure 5.3: Deflection of an Electron Beam by a Stray Magnetic Field

density, in the z direction, B , are

$$\frac{d^2x}{dt^2} = \frac{eB}{m} \frac{dy}{dt}, \quad (5.1)$$

and

$$\frac{d^2y}{dt^2} = -\frac{eB}{m} \frac{dx}{dt}, \quad (5.2)$$

where t is the time, $-e$ is the charge on an electron, and m is the mass of an electron.

The general solutions of these equations of motion are

$$x = -\frac{imC}{eB} \exp\left(\frac{ieBt}{m}\right) + \frac{imD}{eB} \exp\left(-\frac{ieBt}{m}\right) + F, \quad (5.3)$$

and

$$y = \frac{mC}{eB} \exp\left(\frac{ieBt}{m}\right) + \frac{mD}{eB} \exp\left(-\frac{ieBt}{m}\right) + H, \quad (5.4)$$

where C , D , F , and H are arbitrary constants. Given the boundary conditions, for the incident beam, that, at $t = 0$, $(x, y) = (-a, a)$ and $\left(\frac{dx}{dt}, \frac{dy}{dt}\right) =$

$(u, -u)$, the arbitrary constants can be set, to give

$$x = \frac{mu}{eB} \left(\cos \left(\frac{eBt}{m} \right) + \sin \left(\frac{eBt}{m} \right) - 1 \right) - a, \quad (5.5)$$

and

$$y = \frac{mu}{eB} \left(\cos \left(\frac{eBt}{m} \right) - \sin \left(\frac{eBt}{m} \right) - 1 \right) + a. \quad (5.6)$$

Only the electron trajectory, not the behaviour in time, is of interest. Therefore, it would be useful to find a time-independent function of x and y . Using the advance knowledge that the trajectory would be a circle, it was decided to seek such a function of the form $(x - X)^2 + (y - Y)^2$. The incident electron trajectory was thus discovered to be, where $\mu(B) = \frac{mu}{eB}$,

$$(x + \mu(B) + a)^2 + (y + \mu(B) - a)^2 = 2(\mu(B))^2, \quad (5.7)$$

a circle, of radius $\sqrt{2}\mu(B)$, centred on $(-\mu(B) - a, -\mu(B) + a)$. The x co-ordinate at which the reflection takes place, i.e. of the intersection of this circle and the sample surface, is

$$b(B) = -\mu(B) - a \pm \sqrt{(\mu(B))^2 + 2\mu(B)a - a^2}. \quad (5.8)$$

Of the two intersections, the one of interest is that closest to the starting point $(-a, a)$. Therefore, where $\mu(B) < 0$,

$$b(B) = -\mu(B) - a - \sqrt{(\mu(B))^2 + 2\mu(B)a - a^2}, \quad (5.9)$$

and where $\mu(B) > 0$,

$$b(B) = -\mu(B) - a + \sqrt{(\mu(B))^2 + 2\mu(B)a - a^2}. \quad (5.10)$$

The reflected electron trajectory will also be a circle of radius $\sqrt{2}\mu(B)$. However, the centre will be geometrically reflected, in the plane $x = b(B)$, to $(\mu(B) + a + 2b(B), -\mu(B) + a)$, i.e. the trajectory is

$$(x - \mu(B) - a - 2b(B))^2 + (y + \mu(B) - a)^2 = 2(\mu(B))^2. \quad (5.11)$$

On the assumption that $a' = a$, this trajectory strikes the polarimeter front at an x co-ordinate

$$c(B) = \mu(B) + a + b(B) \pm \sqrt{(\mu(B))^2 - (b(B))^2}. \quad (5.12)$$

The intersection of interest is the one closest to the starting point $(b(B), 0)$, i.e. where $\mu(B) < -a$,

$$c(B) = \mu(B) + a + b(B) + \sqrt{(\mu(B))^2 - (b(B))^2}, \quad (5.13)$$

and where $\mu(B) > -a$,

$$c(B) = \mu(B) + a + b(B) - \sqrt{(\mu(B))^2 - (b(B))^2}. \quad (5.14)$$

The distance that the reflected electron beam is displaced, along the polarimeter front, on reversing the stray field, is

$$d(B) = \sqrt{2}(c(B) - c(-B)). \quad (5.15)$$

This distance is plotted against the stray magnetic flux density in figure 5.4, using the estimated $a = 100$ mm, and a value of u based on an estimated electron kinetic energy of 750 eV. The width of the electron beam is of the order of 1 mm, and the width of the polarimeter opening is of order 2 mm. Therefore, any displacement of ~ 100 μm or more will have a significant effect on the acceptance probability. It is clear, from the graph, that a displacement of this size can be obtained with a realistic flux density.

5.2 Traditional Estimation of the Mott Asymmetries

Other workers [5, 34] have considered, in a non-Bayesian framework, the possibility of the two electron detectors in a Mott polarimeter having different detection efficiencies η_i , either due to intrinsic properties of the detectors, or due to a misalignment of the heavy-metal foil that perturbed the scattering probabilities at the two detectors, and devised the following estimator of the product SP of Sherman function and beam polarization, in the presence of such a multiplicative systematic error:

$$SP = \frac{\sqrt{f_{+,1}f_{-,2}} - \sqrt{f_{+,2}f_{-,1}}}{\sqrt{f_{+,1}f_{-,2}} + \sqrt{f_{+,2}f_{-,1}}}. \quad (5.16)$$

This estimator relies on the electron arrival rates $f_{i,j}$, at detectors $j = 1$ and $j = 2$, being measured for beams which, on entering the polarimeter, are of the same intensity, and of polarizations that have equal magnitudes, and opposite signs $i = \pm$. These conditions are met, in the experiments currently being reported, as long as the only effect, on the reflected electron beam, of reversing the sample magnetization is to reverse the beam polarization. In particular, this requires that the spin-orbit interaction at the sample is negligible, as indeed it is, since the kinetic energies of the electrons are much less than their rest mass energy. Note that equation 5.16 is a repeat, in

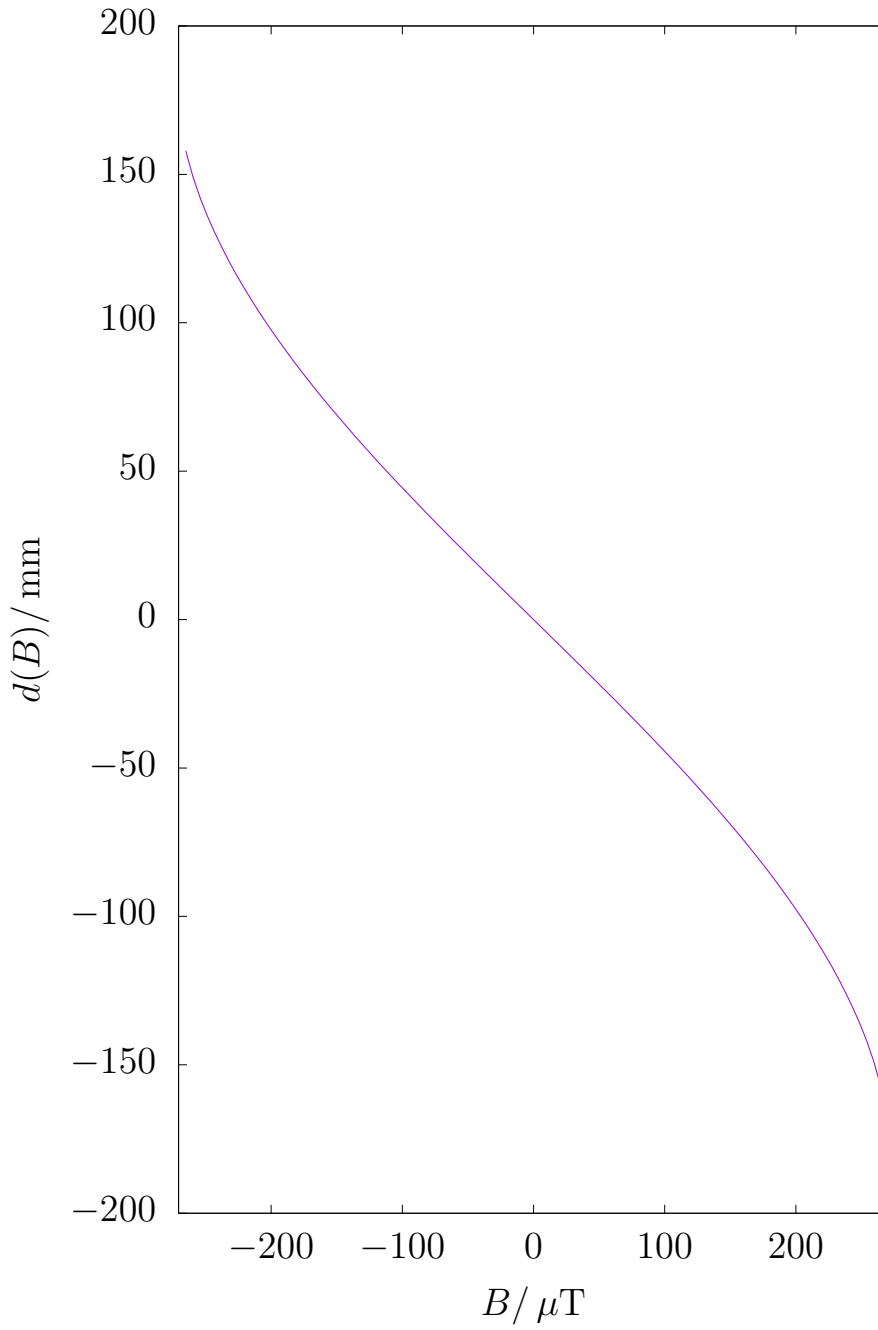


Figure 5.4: The Distance along the Polarimeter Front that the Reflected Electron Beam Is Displaced, on Reversing the Stray Magnetic Field, against Stray Magnetic Flux Density

slightly different notation, of equation 3.7, and is derived and explained in section 3.3.1.

In this section, the results will be interpreted using equation 5.16, as an alternative to the Bayesian inference process described in appendix 5.3.2. Note that the estimator could be re-derived, as the expectation value of SP in a Bayesian model with appropriate assumptions. This would have the advantage of allowing these assumptions, which would be made explicit by the Bayesian approach, to be examined for reasonableness, and changed if necessary (see also *Some Philosophical Implications of Bayesian Statistics* [10].) Unfortunately, the model would be a model of the reflected beam, not of the sample, and therefore successful estimation of its parameters does not further the aim of determining characteristics of the sample.

The procedure used here will be to divide the data set into subsets; the members of any given subset will be all the measurements of electron arrival rate taken under one particular set of conditions of film thickness, incident beam energy, incident beam current, and data acquisition apparatus dwell time. By the design of the experiments, each of these subsets will contain four measurements, of the correct mutual relationship to be used as the $f_{i,j}$ in equation 5.16. This will provide three or four asymmetry values for each combination of film thickness and beam energy; the arithmetic mean of these is taken for presentation. The results of this procedure are shown in figure 5.5.

From a visual inspection of published calibration data (figure 5.7,) the Sherman function is $S \approx -0.23$; this is expected to be independent of the beam energy, because the voltages on electrodes in the polarimeter were adjusted with beam energy to maintain a constant electron kinetic energy when the electrons arrived at the thorium foil. Similarly, it is expected to be independent of film thickness, because the cobalt film whose thickness is varied is not the thorium foil, part of the measuring apparatus, at which the Mott scattering effect takes place; the thickness of the latter is constant.

This estimator is clearly indicating non-zero asymmetries in most cases, indicating that, despite the above-described systematic error due to the stray field from the sample or its holder (section 5.1,) the experiments have successfully detected the cobalt's Weiss field. This is comforting, given that a Bayesian statistical analysis (section 5.3,) which the author believes to be more rigorous than the use of the estimator in equation 5.16, will indicate (section 5.3.3) very decisively that the experiments have detected the cobalt ferro-magnetism.

According to the new, classical-field theory of chapter 2, the reflected beam polarization is expected to be independent of beam energy, because the theory is a zeroth order Taylor expansion in the inverse beam energy,

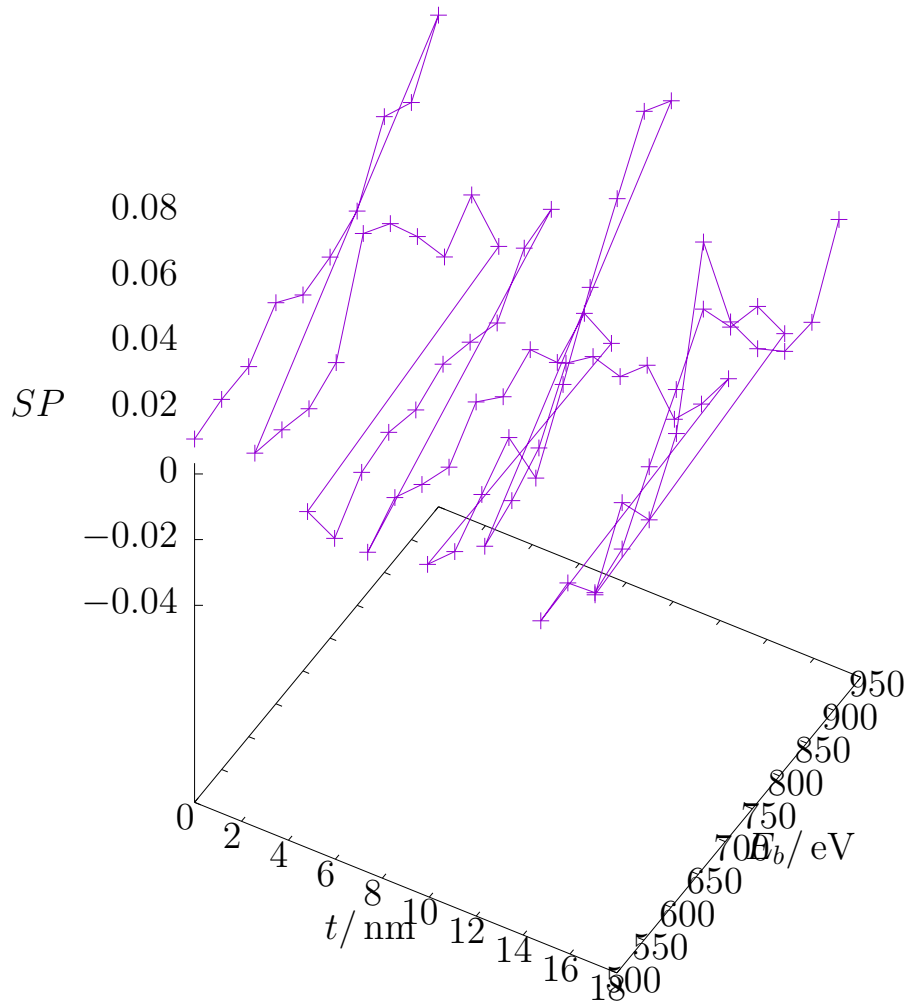


Figure 5.5: Traditional Estimator of Mott Asymmetry against Film Thickness and Incident Beam Energy, for Films on Substrate 9. The Thickness Axis Has a Fractional Calibration Error of $\pm 14\%$. The Lines Are a Guide to The Eye. No Error Bars Are Shown; the Dominant Random Errors Are Those in Mott Asymmetry, Which Are of the Order of 0.005.

the films are all thick enough that Fabry-Perot reflections from the Co/Cu interface, which would otherwise introduce an oscillatory energy dependence, are lost to inelastic scattering, and the energies in the experiments were high enough to be within the expected domain of validity of this Taylor expansion. Given the unfortunate absence of alternative theories, directly applicable to $Co/Cu(001)$ films, hinting at the conceivable form of a systematic energy-dependence in the polarization, it is impossible to comment valuably on whether the data support the hypothesis of energy-independence; it is, however, possible to comment that the generally non-zero measured polarization values appear to militate against versions of the theory in which the Weiss field affecting the probing electrons, and the resulting energy-independent polarization, are zero.

According to the new, classical-field theory of chapter 2, the reflected beam polarization is expected to depend on the film thickness only through the dependence of the electrostatic potential and Weiss field in the sample on film thickness. The only clear pointer available to the form of this dependence is the non-ferro-magnetic nature of bulk copper, which would lead one to expect a zero polarization from the zero-thickness film. Intriguingly, the measured polarizations from the zero-thickness film appear to depart from zero. It is not clear whether this is indicative of some localized magnetization at the surface of the copper, or of a systematic error in the measured results, such as that, discussed in a footnote above, which may be introduced by the use of a non-linear, and therefore potentially biased, polarization estimator, as will be discussed below (section 5.3.1.)

The size of the estimated reflected beam polarization is typically of the order of 0.1. This is the same order of magnitude as most of the published measured and theoretical reflected beam polarizations at high beam energies, reviewed in chapter 2.

Having used this simple estimator to analyse the data, the author will now implement a more sophisticated, Bayesian method for parameter estimation and model comparison.

5.3 Further Discussion of, and Conclusions from, the Experimental Results

Above, several references have been made to a Bayesian inference process, for drawing conclusions about sample characteristics from the experimental results. In this section, that Bayesian inference process is presented. First, an explanation will be given of why the author believes undertaking this

more sophisticated inference process to be desirable.

5.3.1 Why Is This Statistical Analysis Necessary?

The author is the first to acknowledge the benefits of having as little complicated mathematics as possible between raw experimental results and conclusions, in terms of the ability of complicated calculations to conceal mistakes. Therefore, some justification seems to be required for the intervention of a sophisticated statistical algorithm. The justification will have two parts: the first will explain why any statistical inference process is needed at all, and the second will explain why a new Markov Chain Monte Carlo algorithm was coded, rather than using computer codes already in the public domain.

Why Use Any Statistical Inference?

The community of researchers using measurements of the spin polarization of electron beams has long had available the estimator in equation 5.16, for obtaining the spin polarization of an electron beam, from the measured electron arrival rates at a Mott polarimeter's two detectors; this estimator eliminates systematic errors due to misalignment of the electron beam entering the polarimeter, and due to unequal sensitivities of the two detectors. By a happy coincidence, the systematic error that may be introduced by a stray field, which reverses with the sample magnetization, is also multiplicative, and is, therefore, also eliminated by this polarization estimator.

It was established, following a published derivation [5], in section 3.3.1 that, in the absence of random errors, the estimator is equal to the true polarization. Why, therefore, cannot the estimator, along with published values of the Sherman function S , be used to calculate the reflected beam polarization, and then equations 2.8 and 2.10 inverted to give the electromagnetic characteristics of the sample, avoiding any need for a statistical process?

A footnote to section 3.3 alludes to the answer, which lies in the seemingly innocuous phrase “in the absence of random errors.” Real experiments are characterized by the presence, not the absence, of random errors, in particular, in this case, in the measured electron arrival rates. When there are random errors, the electron arrival rate $f_{i,j}$, for given true values of the intensity and polarization of the beam entering the polarimeter, G_{true} and P_{true} , is characterized⁵ by a probability density distribution $P(f_{i,j}|G_{\text{true}}, P_{\text{true}})$. On the four-dimensional space of the $f_{i,j}$, one can define both the joint

⁵This is not one of the items of controversy between Bayesian and frequentist statisticians, and is a proposition that statisticians from both camps would accept.

probability density $\prod_{i,j} P(f_{i,j}|G_{\text{true}}, P_{\text{true}})$, and the polarization estimator $P_{\text{formula}}(\mathbf{f}) = \frac{\sqrt{f_{1,+}f_{2,-}} - \sqrt{f_{1,-}f_{2,+}}}{\sqrt{f_{1,+}f_{2,-}} + \sqrt{f_{1,-}f_{2,+}}}$. One can then, in principle, obtain the expectation value $\int_{\text{All space}} P_{\text{formula}}(\mathbf{f}) \prod_{i,j} P(f_{i,j}|G_{\text{true}}, P_{\text{true}}) df_{i,j}$ of the estimator, given G_{true} and P_{true} . If this expectation value is equal to P_{true} , the estimator is unbiased. If, on the other hand, the expectation value is not equal to P_{true} , it is a biased estimator; in other words, despite its success in eliminating systematic errors due to certain physical conditions, the estimator has created a new systematic error of its own, out of the random errors in the electron arrival rate measurements; this is the systematic error which, it was suggested above, may have been responsible for the non-zero polarization estimates obtained from bare copper.

Unfortunately, because the estimator is non-linear in the raw measurements, it is very likely that its expectation value will not be equal to P_{true} , and that such an artificial systematic error will arise. Worse still, evaluating the integral, to quantify the size of this systematic error (and possibly correct it,) is beyond the author's analytical capabilities; it could be integrated numerically, but this would sacrifice the advantage of mathematical simplicity, which was the motivation for examining this estimator. This is what justifies turning to statistical inference.

Why Write New Software for the Statistical Inference?

Having made the case for using a statistical process to obtain information, there remains a need to explain why the results were analysed using a new program, written by the author of this thesis, implementing a Markov chain Monte Carlo method, rather than using computer codes already in the public domain. Computer codes for statistical inference already in the public domain (or at least, those known to the author,) such as Gnuplot [87] and Origin [88], typically perform both model comparison and parameter estimation based on the χ^2 statistic for the badness of fit of a model to the data,

$$\chi^2 = \sum_i \left(\frac{(x_i - y_i)^2}{\sigma_i^2} \right), \quad (5.17)$$

where i indexes the experimental conditions where some measurements have been made, x_i is the measured value obtained in conditions i , y_i is the value predicted by the model in conditions i , and σ_i is the quoted random error on measurement x_i . y_i , and sometimes σ_i , depend on the values chosen for the model's adjustable parameters, and on which of the distinct, discrete models available is being considered; hence, the badness of fit χ^2 also de-

depends on these influences. The measure of goodness of fit used in Bayesian statistics (and in some non-Bayesian methods) is [89] the likelihood function $P(D|M, \mathbf{P})$, which is the conditional probability density distribution over the space of values of the set D of measurements, given a model M and a set of model parameter values \mathbf{P} ; the likelihood, like χ^2 , depends on the models that are chosen. On the common [90] assumption that this probability distribution, as a function of any single measured value, is Gaussian in shape, χ^2 has a clear meaning in Bayesian statistics:

$$P(D|M, \mathbf{P}) = \frac{1}{\sqrt{2^N \pi^N \prod_i (\sigma_i^2)}} \exp \left(-\frac{\chi^2}{2} \right), \quad (5.18)$$

i.e. χ^2 is proportional to the logarithm of the likelihood.

The output given by the typical parameter estimation and model comparison software already in the public domain consists of:

- The set \mathbf{P}^* of values of a model's parameters that minimizes χ^2 (equivalently, maximizes the likelihood,) providing an estimate of the parameter values in which it is reasonable to believe, given the experimental evidence; to find the minimum, the standard programs use the Marquadt-Levenberg algorithm, which is explained in *Numerical Recipes* [91],
- the coefficients of a second-order Taylor expansion of the χ^2 statistic in the parameters of a model, about \mathbf{P}^* , describing a parabolic approximation to χ^2 (equivalently, a Gaussian approximation to the likelihood) in parameter space, providing an estimate of the uncertainty in the parameter estimates \mathbf{P}^* ,
- the maximum value χ^{2*} of the χ^2 statistic, as a model's parameters are varied, providing an estimate of a model's badness of fit for model comparison purposes, and, in the case of Gnuplot,
- a version of χ^{2*} , adjusted by dividing it by the difference between the number of measurements and the number of adjustable model parameters, providing an alternative estimate of a model's badness of fit for model comparison purposes, which attempts to implement Occam's razor; the philosophical and statistical basis for implementing Occam's razor in this way is unclear.

The first reason for deciding against using codes of this form is that output of a best-fit goodness of fit for model comparison leaves the user with

a problem of how to implement Occam’s razor; Gnuplot’s adjusted χ^2 * attempts to implement Occam’s razor by penalizing models for having many adjustable parameters. However, if, like the author, one believes that the purpose of Occam’s razor is to prevent a model from using information from experimental results to fine-tune its parameters, then recycling the same information to act as evidence for itself against other models, then using an Occam’s razor based on the number of adjustable parameters raises the possibility of unfairly penalizing a model that, although it has many adjustable parameters, does not fine-tune them very much on the basis of the experimental data, i.e. that is a good fit to the experimental results over a wide range of parameter values. As it will transpire, this is precisely the situation encountered with the experiments and models central to this thesis. Bayesian methods implement [85, 52] Occam’s razor automatically, by comparing models’ average likelihoods over all values of their parameters (known as marginal likelihoods,) weighted according to the pre-experiment plausibility function encoded in the prior probability distribution, instead of comparing their maximum likelihoods; this directly penalises [85, 52] models for fine-tuning their parameters, not for merely having parameters to fine-tune.

The author is not claiming that it would be impossible to implement a fair Occam’s razor using, for example, Gnuplot. Indeed, since completing the analysis of the data presented in this thesis, the author has, in the course of a separate experimental project, devised a formula for obtaining a marginal likelihood from the outputs of Gnuplot. However, some programming is required to implement this.

The second reason for deciding against using the established, publicly available codes is that parameter estimation by a least-squares method has a number of features, some of which tend to render it unsuitable for use in the present project:

- The assumption, needed to give χ^2 a clear meaning in Bayesian (or any probabilistic) statistics, that the likelihood, as a function of the value of an individual experimental datum, for fixed model parameters, is a Gaussian, is reasonable, given that electron arrival at the detectors is expected to be a Poisson process, and that the numbers of electrons being counted are sufficiently large [84] for a Gaussian to be an extremely good approximation to a Poisson distribution; this assumption has not been challenged in the development of the author’s Bayesian method, and will be discussed briefly below (section 5.3.4.)
- The assumption that the likelihood associated with the experimental data set as a whole, as a function of the adjustable parameters of a

model, is well approximated by a Gaussian (the second order Taylor expansion of χ^2), cannot stand for this experiment and the new, classical-field model presented in chapter 2. This is because, when equation 2.8, which predicts the measurable reflected beam polarization P , as a function of the electrostatic potential V and Weiss field B in the sample, is inverted to give the ratio $\frac{B}{V}$ (or B or V individually) as a function of P , $\frac{B}{V}$ is found not to be single-valued. This means that the likelihood function has two peaks in parameter space; a Gaussian approximation can only hope to represent one of these peaks, and therefore will lose crucial information. This difficulty is likely to be surmountable; one of the standard computer codes could perhaps be used with some function of $\frac{B}{V}$, which is a single-valued function of P , as a fitting parameter, instead of B and V separately, or $\frac{B}{V}$ itself. Nevertheless, this introduces extra complication in configuring a standard fitting program, which slightly undermines the case in terms of simplicity for using a standard program.

- The parabolic approximation to χ^2 , or Gaussian approximation to the likelihood, output by a least-squares algorithm, even, if the approximation holds, encodes only the goodness of fit of the model to the data as a function of the adjustable parameters. In Bayesian statistics, this is only half the story of parameter estimation; to obtain a Bayesian “belief function” of the parameters, representing how strongly one believes in each conceivable set of parameter values, given the experimental results (this belief function is known as the posterior probability distribution,) the likelihood must be modulated by a plausibility function, or prior probability distribution, describing the level of credence one gives to each conceivable set of parameters before undertaking the experiment. Using the output of the least-squares algorithm directly for parameter estimation would be equivalent to an implicit, fixed assumption that the prior probability distribution is uniform over parameter space. Elsewhere [10], the author has expressed concern over the philosophical consequences of prior probability distributions being implicit and fixed. Here, it is possible to be more pragmatic, simply noting that for many parameters, a uniform prior probability distribution is inappropriate: for example, the parameter might be a quantum efficiency, in which case it makes sense to give it a non-zero prior probability density for parameter values between zero and one, and a zero prior probability density outside this domain; alternatively, standard data tables might give an estimate and uncertainty for the parameter, based on previous experimental evidence, which could be well represented by a Gaussian

prior probability distribution. This problem is also likely to be surmountable: since completing the analysis of the data presented in this thesis, the author has, in the course of a separate experimental project, examined the possibility of transforming a parameter a , over which a prior probability distribution $P(a)$ is required, to a parameter b , which is a function of a , such that $P(a)da = db$, i.e. the prior probability distribution over b is uniform, and b can be used as a fitting parameter in a least-squares algorithm; it transpires that, for the common forms of $P(a)$ that the author has examined to date, the differential equation has a ready analytical solution, providing a simple formula to transform between a and b . Nevertheless, this introduces extra complication in configuring a standard fitting program, which slightly undermines the case in terms of simplicity for using a standard program.

To summarize, there are certain obstacles to the use of computer codes already in the public domain to undertake a valid analysis of the experimental data presented in this project. Although methods of working around these obstacles could be devised, these methods entail some mathematical and computational complication, and therefore compromise the advantage of simplicity that would be the motivation for choosing existing computer codes. Therefore, the author has, for the purposes of this project, chosen instead to use a fundamentally Bayesian Markov chain Monte Carlo method for parameter estimation and model comparison, and to code this method anew, in the high-level programming language Perl; the choice of such a high-level language may recover some of the simplicity lost by choosing to write new code.

Having explained why the inference method has been chosen, it is time to undertake parameter estimation and model comparison according to that method.

5.3.2 Statistical Inference Process

In this section, the data presented in chapter 5 will be used to estimate the values of the adjustable parameters in two models of the system of samples and measuring apparatus, and to compare the two models. The framework used for this data interpretation will be Bayesian inference [89, 92, 85, 52, 93, 90]. The finer mathematical details of the inference method, including the prior probability distributions and likelihood functions, and a description of the numerical method used for the calculations, will be presented in section 5.3.4.

Framework of the Models

Both models are based on the new theory of polarized electron reflection from a bulk sample presented in chapter 2. The use of a model intended for a bulk sample is justified on the basis that the inelastic mean free path of electrons, of the energies used in this experiment, is [83, 51] no more than ~ 1 nm, with the result that even rather thin films will appear, when examined with an electron beam, to be bulk materials.

Therefore, when the beam current into the electron gun is F , the rate of electron incidence on the sample is F/e , and the rate of electrons leaving the sample, in the reflected beam (figure 3.1,) is, from integration of equation 2.26,

$$G = \left(\frac{e^2 V^2}{16 E_b^2 \cos^4 I} + \frac{e^2 \hbar^2 B^2}{192 m_e^2 E_b^2 \cos^4 I} \right) \frac{F}{e}. \quad (5.19)$$

The polarization of the reflected beam is, from equation 2.8,

$$P = -\frac{4e^2 \hbar m_e V_1 B_1}{12e^2 m_e^2 V_1^2 + e^2 \hbar^2 B_1^2}. \quad (5.20)$$

The electrostatic potential, V , and the magnetic flux density, B , in the sample, are adjustable parameters of the “main” model, while in the “null” model, only V is adjustable, B being fixed at zero. In fact, since there are eight cobalt film thicknesses, including zero thickness (table 5.1,) there are multiple parameters of this type, V_j and B_j , with the film thicknesses indexed by integers j , from 0 to 7 inclusive; for thickness 0, B_0 is fixed at zero even for the “main” model. These then lead to electron leaving rates G_j and reflected polarizations P_j .

Since the entrance hole of the polarimeter (figure 3.1) is of finite width, it is possible that not all of the electrons in the reflected beam will enter the polarimeter. Therefore, an acceptance probability a is defined, so that the rate of electrons entering the polarimeter is aG_j . The entrance hole and grids are assumed to be non-polarizing, with the result that the polarization of the beam entering the polarimeter is P_j .

The thorium foil then scatters electrons towards the two channeltrons. The rate of electron arrival at channeltron 1 will be, by equation 3.4,

$$f_a^{(1,j)} = \Gamma(1 + SP_j)aG_j, \quad (5.21)$$

and that at channeltron 2 will be, by equation 3.5,

$$f_a^{(2,j)} = \Gamma(1 - SP_j)aG_j, \quad (5.22)$$

where the spin-averaged scattering probability Γ and the Sherman function S are characteristics of the thorium foil. Calibration values of Γ and S for

a Mott polarimeter, of identical design to that used for these experiments, have been provided by other workers [6], and those for electrons with energy 20 keV are reproduced in figures 5.6 and 5.7. Although the energy of the electrons on striking the thorium foil, in the experiments presented in this thesis, is (20.5 ± 0.00725) keV, not 20 keV, the systematic error introduced by this energy difference [6] is negligible, compared with the quantization error of the author's readings from the published graphs (section 5.3.4.)

The published calibration data are for electron energies, on striking the thorium foil, of 20 keV and 25 keV, and are presented as a function of the energy loss window W , defined by the potential at the retarding grids (chapter 3.) The author has chosen to include the published data for a 20 keV energy, on striking the thorium foil, in the data set (section 5.3.4,) from which inference is to proceed, and to characterize the thorium foil by twelve adjustable parameters, Γ_k and S_k , where k runs through integers from 0 to 5 inclusive,

$$\Gamma = \sum_{k=0}^5 \Gamma_k W^k, \quad (5.23)$$

and

$$S = \sum_{k=0}^5 S_k W^k. \quad (5.24)$$

These fifth order Taylor expansions are an extension, to calibration data that include relatively large energy loss windows, of the spirit of the first and second order Taylor expansions in "Use of thorium as a target in electron-spin analyzers" [94]. The fifth order has been chosen to provide a number of adjustable parameters, in each Taylor expansion, that is the largest integer less than or equal to half the number of calibration data points, in line with MacKay's [93, 90] recommendation for the number of parameters in neural network models.

Channeltron i (figure 3.2,) used in single-electron counting mode in these experiments, has a detection efficiency η_i , adjusted by a time-dependent perturbation p_{ij} to allow for drift (section 5.5.) Since the speed of the present experiments has been chosen so that the drift should not be significant within the time-scale of measurements on a single film thickness, each channeltron has just one p_{ij} value for each film thickness; the subscript j , as before, indexes the film thickness. Therefore, the electron detection rate at the channeltron i , from film thickness j , is predicted to be

$$f_p^{(i,j)} = p_{ij} \eta_i f_a^{(i,j)}. \quad (5.25)$$

The p_{ij} and η_i values are further adjustable parameters of the model.

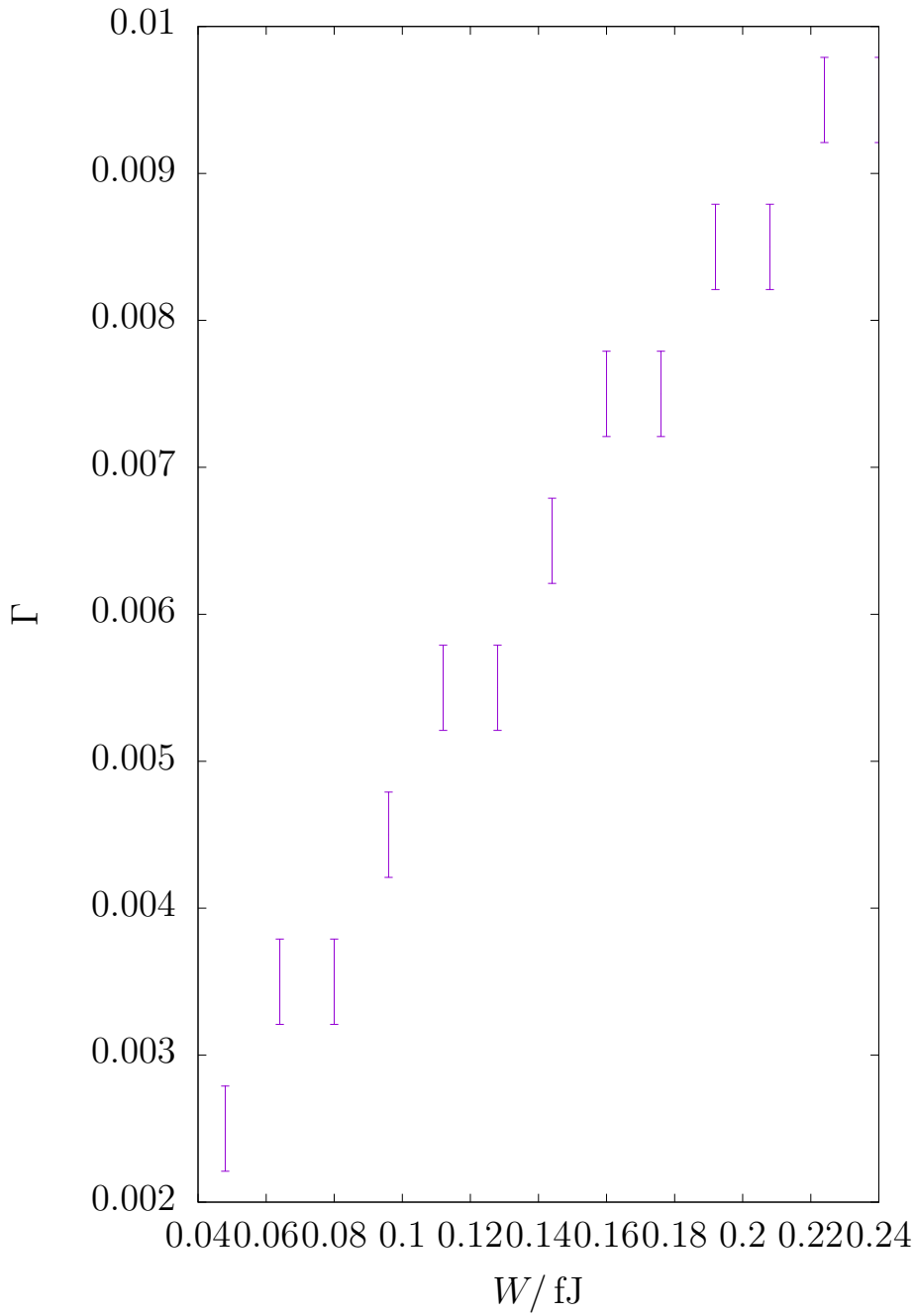


Figure 5.6: Graph of spin-averaged scattering probability Γ against energy loss window W , from the calibration data for the compact retarding-potential Mott polarimeter, provided in “High-efficiency retarding-potential Mott polarization analyzer” [6]. The error bars represent the standard deviations associated with the quantization of the author’s readings from the published graph.

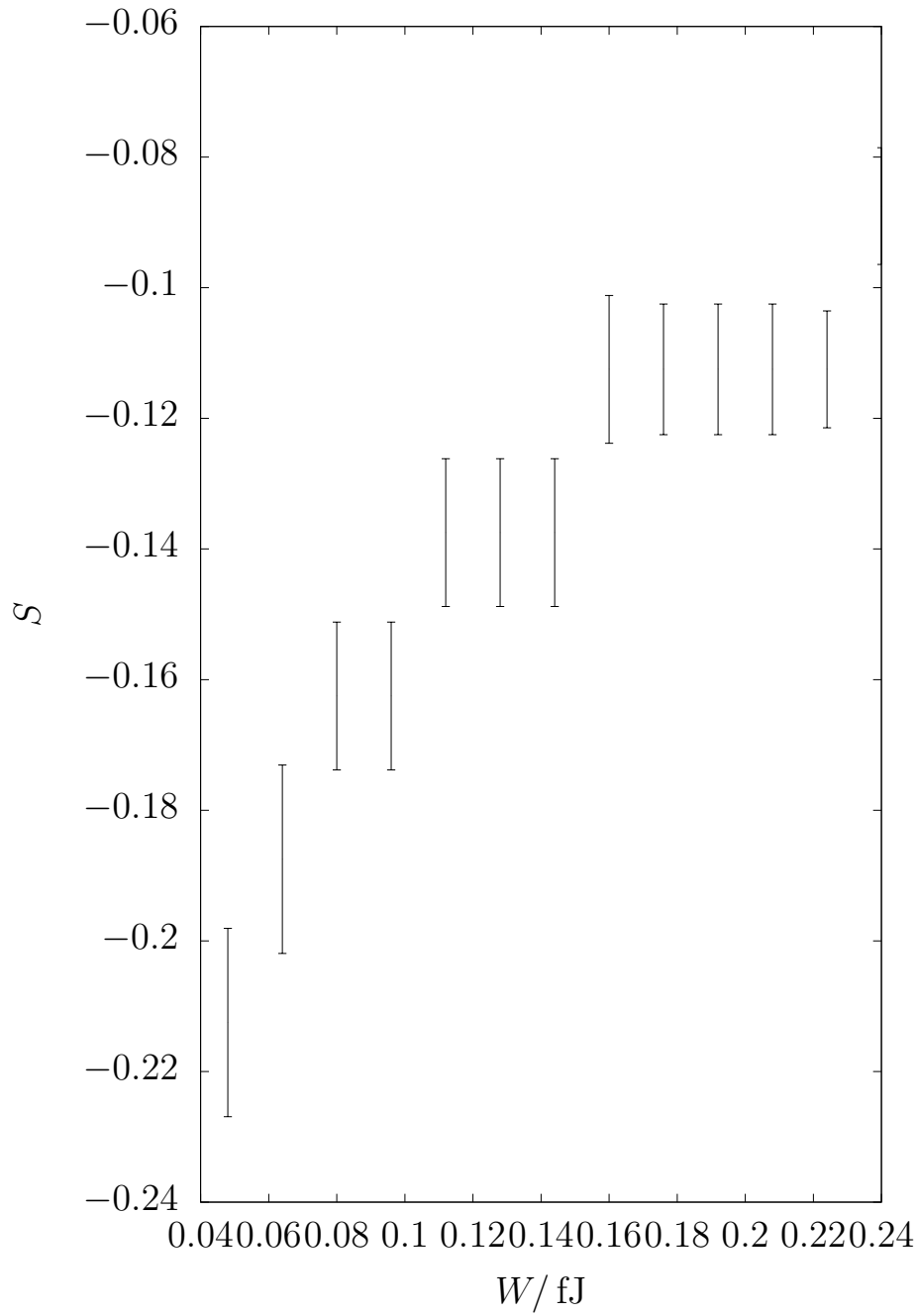


Figure 5.7: Graph of Sherman function S against energy loss window W , from the calibration data for the compact retarding-potential Mott polarimeter, provided in “High-efficiency retarding-potential Mott polarization analyzer” [6]. The error bars represent the sums in quadrature of the standard deviation associated with the quantization of the author’s readings from the published graph, and the error quoted on the published graph.

5.3.3 Conclusions

This section describes the conclusions, obtained from the Bayesian inference process, about the parameters in the two models, and about which model is correct.

1. The electrostatic potential in the sample, as a function of cobalt thickness, in the null model, is as shown in figure 5.8.
2. The electrostatic potential in the sample, as a function of cobalt thickness, in the main model, is as shown in figure 5.9.
3. The magnetic flux density in the sample, as a function of cobalt thickness, in the main model, is as shown in figure 5.10.
4. The posterior probability of the null model, in which cobalt ferromagnetism is not detected, is estimated at $0.34 \times 10^{-2014444631}$, and that of the main model, in which cobalt ferro-magnetism is detected, at 0.1×10^1 .

At first glance, the precision of the inferred electrostatic potentials and magnetic flux densities appears a rather unimpressive return on the experimental effort involved in obtaining the measurements. In addition, a comparison (tables 5.4, 5.5) of the beliefs held about all of the parameters, including those concerned with instrumental calibration and with transient instrumental characteristics, before and after the data in chapter 5, along with the published calibration data (figures 5.6, 5.7,) have been taken into account, shows a broadening, rather than the narrowing that one might expect, of the probability distribution over the parameter set, due to the data.

However, the very decisive choice of model with successful detection of the Weiss field as the better model supplies a greater reward.

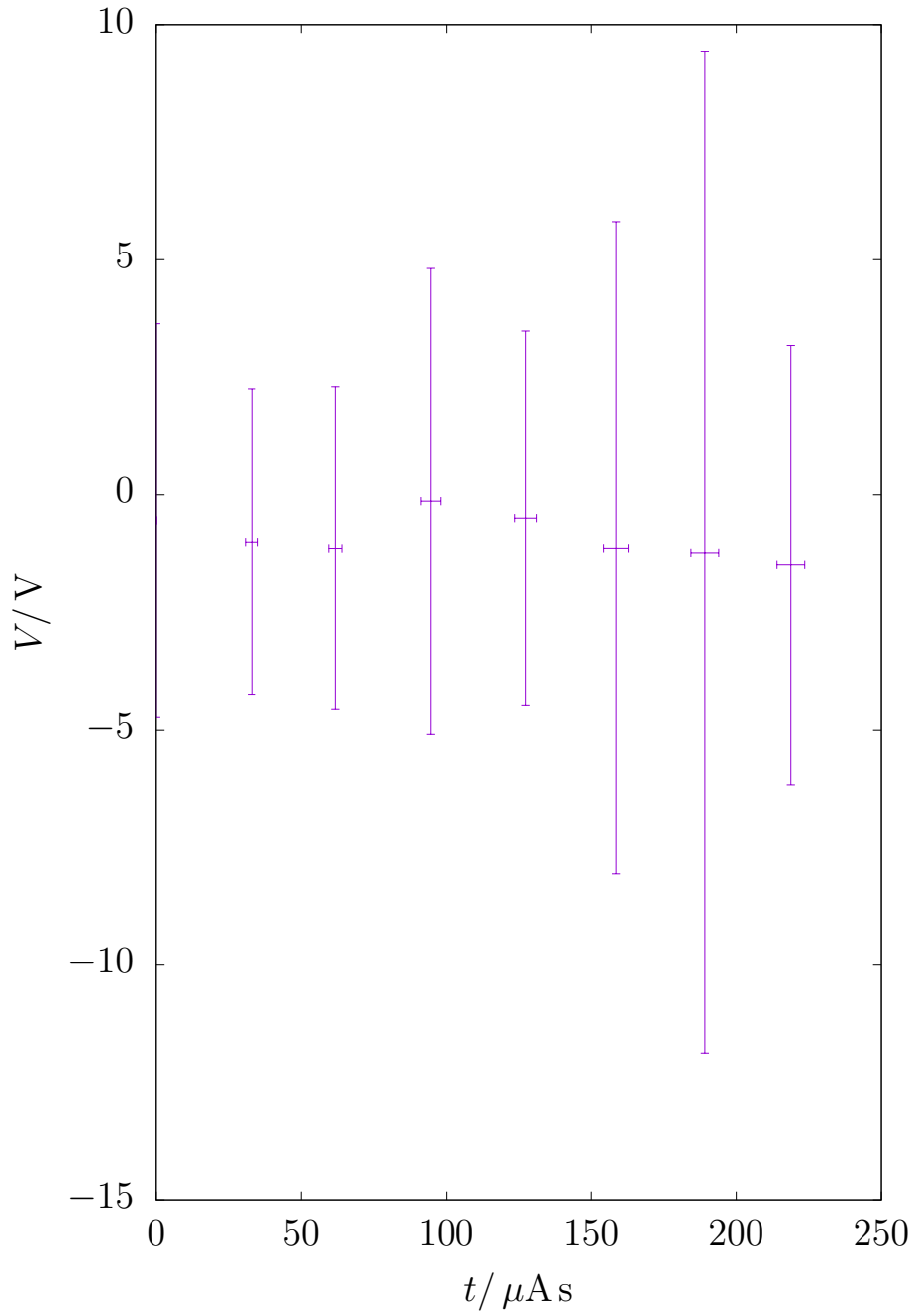


Figure 5.8: A Graph of the Inferred Electrostatic Potential in the Sample, in the Null Model, against *Co* Thickness. The Conversion factor between the Units of Thickness on the Horizontal Axis, and More Conventional Thickness Units, Is (appendix B) $(78 \pm 11) \mu\text{m A}^{-1} \text{s}^{-1}$.

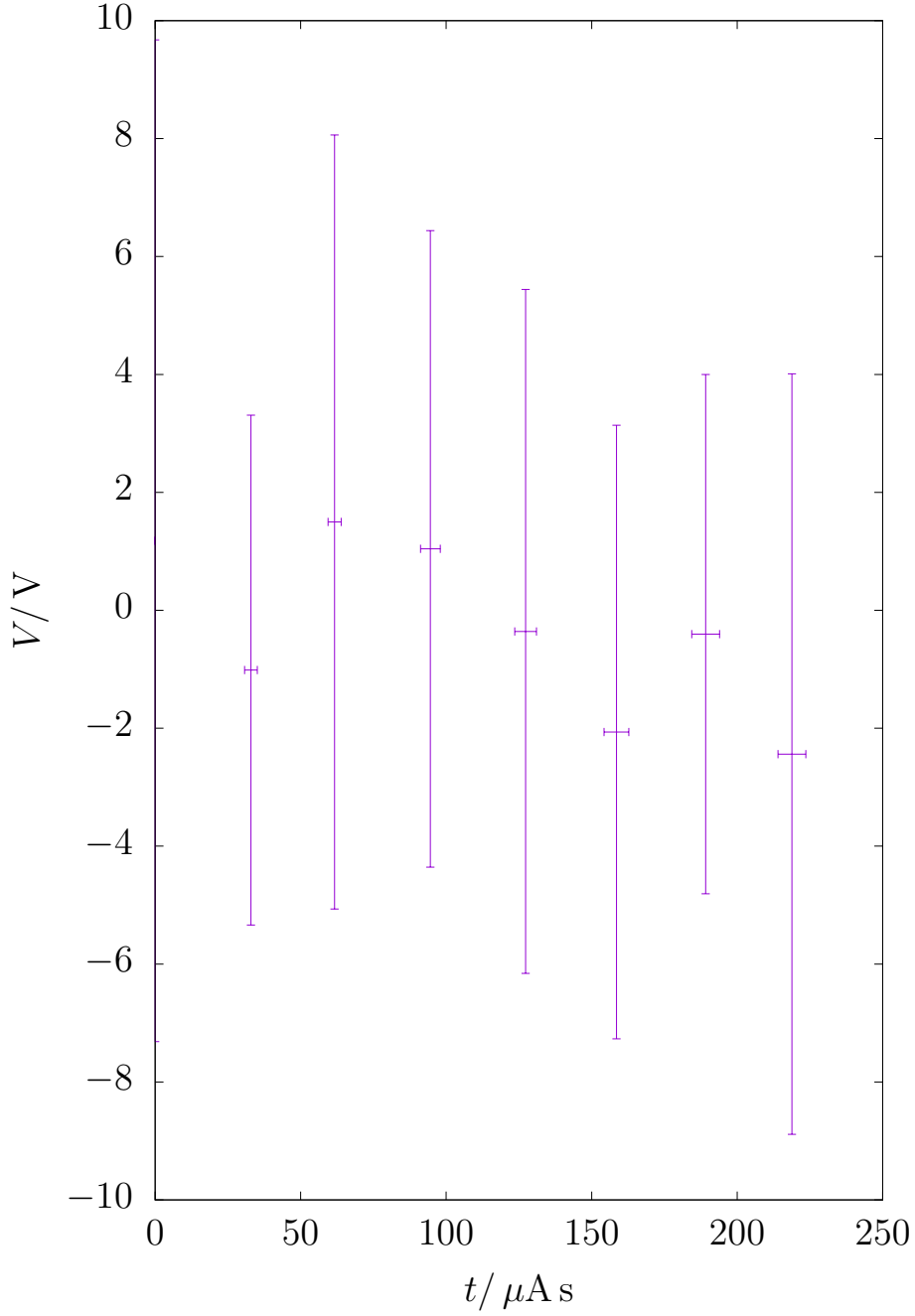


Figure 5.9: A Graph of the Inferred Electrostatic Potential in the Sample, in the Main Model, against Co Thickness. The Conversion factor between the Units of Thickness on the Horizontal Axis, and More Conventional Thickness Units, Is (appendix B) $(78 \pm 11) \mu\text{m A}^{-1} \text{s}^{-1}$.

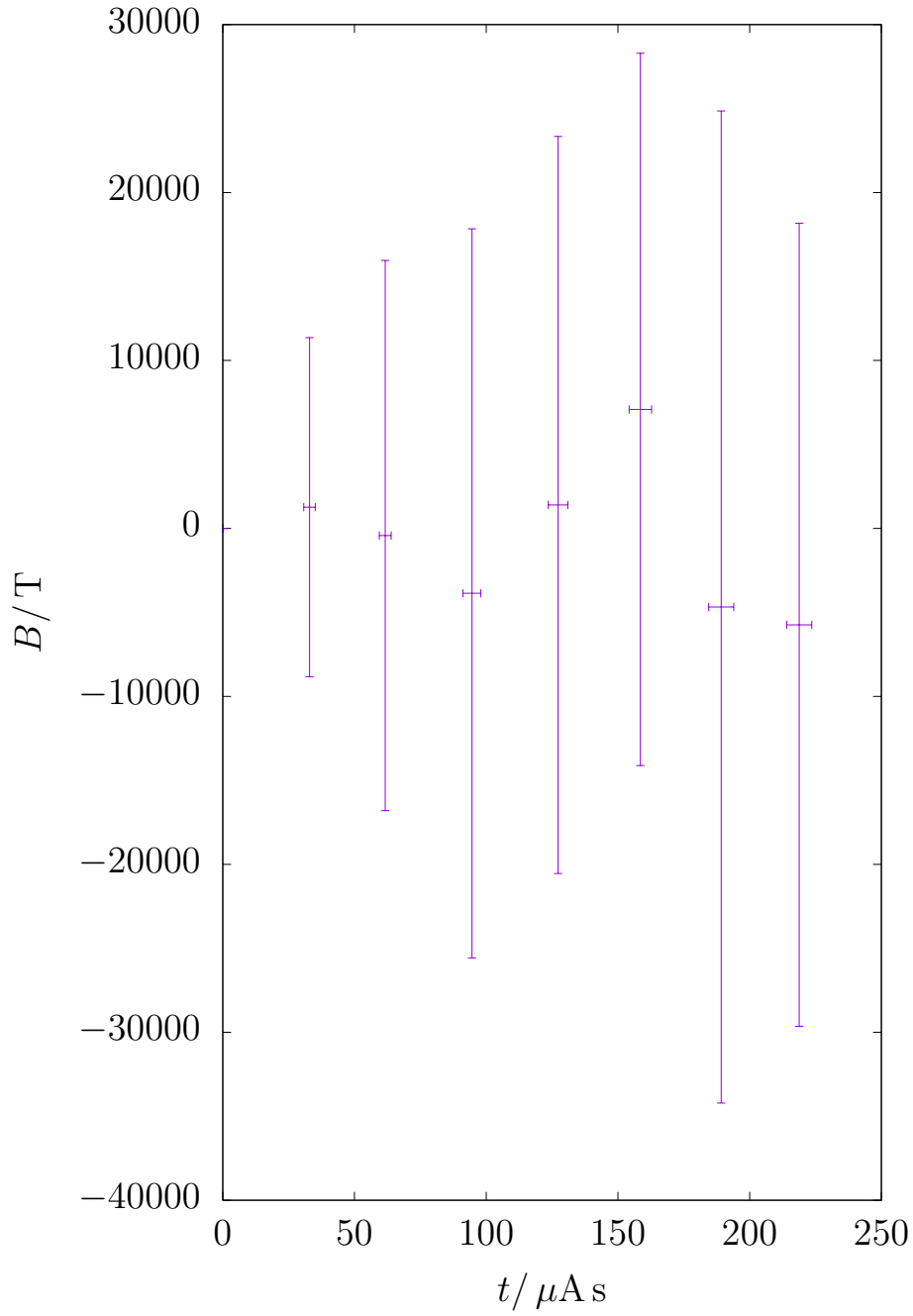


Figure 5.10: A Graph of the Inferred Magnetic Flux Density in the Sample, in the Main Model, against *Co* Thickness. The Conversion factor between the Units of Thickness on the Horizontal Axis, and More Conventional Thickness Units, Is (appendix B) $(78 \pm 11) \mu\text{m A}^{-1} \text{s}^{-1}$.

Parameter	Prior Value	Posterior Value
a	0.5 ± 0.29	-0.03 ± 0.53
P_{10}	1 ± 0.05	0.8 ± 3.1
P_{11}	1 ± 0.05	0.6 ± 3
P_{12}	1 ± 0.05	0.9 ± 3.7
P_{13}	1 ± 0.05	1.14 ± 0.82
P_{14}	1 ± 0.05	0.6 ± 3.5
P_{15}	1 ± 0.05	0.8 ± 5.1
P_{16}	1 ± 0.05	1.17 ± 0.97
P_{17}	1 ± 0.05	0.7 ± 1.8
P_{20}	1 ± 0.05	0.8 ± 3.1
P_{21}	1 ± 0.05	0.8 ± 2.9
P_{22}	1 ± 0.05	0.8 ± 3.8
P_{23}	1 ± 0.05	1.23 ± 0.67
P_{24}	1 ± 0.05	1.1 ± 3.3
P_{25}	1 ± 0.05	0.9 ± 5.1
P_{26}	1 ± 0.05	1.34 ± 0.73
P_{27}	1 ± 0.05	1.4 ± 1.4
Γ_0	0.5 ± 0.29	-0.4 ± 4.4
Γ_1/fJ^{-1}	0 ± 6.2	20 ± 170
Γ_2/fJ^{-2}	0 ± 39	-100 ± 1200
Γ_3/fJ^{-3}	0 ± 240	-600 ± 3100
Γ_4/fJ^{-4}	0 ± 1500	-4000 ± 19000
Γ_5/fJ^{-5}	0 ± 9500	30000 ± 170000
S_0	0 ± 0.58	0 ± 15
S_1/fJ^{-1}	0 ± 12	-10 ± 730
S_2/fJ^{-2}	0 ± 78	-100 ± 2000
S_3/fJ^{-3}	0 ± 490	-2000 ± 24000
S_4/fJ^{-4}	0 ± 3000	20000 ± 240000
S_5/fJ^{-5}	0 ± 19000	-60000 ± 680000
η_1	0.835 ± 0.032	0.79 ± 0.56
η_2	0.835 ± 0.032	0.81 ± 0.76
V_0/V	-0.55 ± 0.31	-0.5 ± 4.2
V_1/V	-0.9 ± 0.32	-1 ± 3.3
V_2/V	-0.9 ± 0.32	-1.1 ± 3.4
V_3/V	-0.9 ± 0.32	-0.1 ± 5
V_4/V	-0.9 ± 0.32	-0.5 ± 4
V_5/V	-0.9 ± 0.32	-1.1 ± 6.9
V_6/V	-0.9 ± 0.32	-1 ± 11
V_7/V	-0.9 ± 0.32	-1.5 ± 4.7

Table 5.4: The Effect of the Experimental Evidence on Beliefs about Parameters in the Null (Non-Magnetic Cobalt) Model. The Parameters Are Described in Tables 5.6 and 5.7

Parameter	Prior Value	Posterior Value
a	0.5 ± 0.29	0.06 ± 0.38
P_{10}	1 ± 0.05	1.27 ± 0.93
P_{11}	1 ± 0.05	1.8 ± 2.1
P_{12}	1 ± 0.05	-0.3 ± 2.8
P_{13}	1 ± 0.05	1.3 ± 2.3
P_{14}	1 ± 0.05	-0.3 ± 3.2
P_{15}	1 ± 0.05	0.8 ± 2
P_{16}	1 ± 0.05	0.4 ± 1.6
P_{17}	1 ± 0.05	0.2 ± 2.5
P_{20}	1 ± 0.05	0.3 ± 1.5
P_{21}	1 ± 0.05	0.6 ± 2.7
P_{22}	1 ± 0.05	1.3 ± 2.6
P_{23}	1 ± 0.05	0.5 ± 2.5
P_{24}	1 ± 0.05	1.5 ± 2.8
P_{25}	1 ± 0.05	1.8 ± 1.1
P_{26}	1 ± 0.05	0.4 ± 1.6
P_{27}	1 ± 0.05	0.8 ± 2.4
Γ_0	0.5 ± 0.29	-0.5 ± 2.8
Γ_1/fJ^{-1}	0 ± 6.2	25 ± 100
Γ_2/fJ^{-2}	0 ± 39	-260 ± 600
Γ_3/fJ^{-3}	0 ± 240	1500 ± 3000
Γ_4/fJ^{-4}	0 ± 1500	-2000 ± 12000
Γ_5/fJ^{-5}	0 ± 9500	-9000 ± 95000
S_0	0 ± 0.58	-0.3 ± 7.4
S_1/fJ^{-1}	0 ± 12	70 ± 200
S_2/fJ^{-2}	0 ± 78	-500 ± 1100
S_3/fJ^{-3}	0 ± 490	-700 ± 9700
S_4/fJ^{-4}	0 ± 3000	-20000 ± 62000
S_5/fJ^{-5}	0 ± 19000	170000 ± 530000

η_1	0.835 ± 0.032	0.5 ± 0.71
η_2	0.835 ± 0.032	0.71 ± 0.38
V_0/V	-0.55 ± 0.31	1.2 ± 8.5
V_1/V	-0.9 ± 0.32	-1 ± 4.3
V_2/V	-0.9 ± 0.32	1.5 ± 6.6
V_3/V	-0.9 ± 0.32	1 ± 5.4
V_4/V	-0.9 ± 0.32	-0.4 ± 5.8
V_5/V	-0.9 ± 0.32	-2.1 ± 5.2
V_6/V	-0.9 ± 0.32	-0.4 ± 4.4
V_7/V	-0.9 ± 0.32	-2.4 ± 6.5
B_1/T	0 ± 1000	1000 ± 10000
B_2/T	0 ± 1000	0 ± 16000
B_3/T	0 ± 1000	-4000 ± 22000
B_4/T	0 ± 1000	1000 ± 22000
B_5/T	0 ± 1000	7000 ± 21000
B_6/T	0 ± 1000	-5000 ± 30000
B_7/T	0 ± 1000	-6000 ± 24000

Table 5.5: The Effect of the Experimental Evidence on Beliefs about Parameters in the Main (Magnetic Cobalt) Model. The Parameters Are Described in Tables 5.6 and 5.7

5.3.4 The Details of the Inference Method

Standard Probability Distributions

In this process, definitions of some standard probability density distributions will be useful.

- The Dirac delta function is such that

$$\delta(x) = 0, \quad (5.26)$$

for $x \neq 0$, and

$$\int_{-\epsilon}^{\epsilon} \delta(x) dx = 1, \quad (5.27)$$

for any $\epsilon > 0$. This probability distribution expresses the certainty that $x = 0$.

- The Gaussian probability distribution is

$$G(x; \mu, \sigma) = \frac{1}{\sqrt{2\pi\sigma^2}} \exp \left(-\frac{(x - \mu)^2}{2\sigma^2} \right). \quad (5.28)$$

This probability distribution is a standard default, much beloved [93, 90] of the physics community, for the distribution over a parameter x , knowledge of which can be summarized by an expected value μ and a degree of variation σ about the expected value.

- A perfect top-hat function is

$$T_0(x; l, h) = \frac{1}{h - l}, \quad (5.29)$$

if $l \leq x \leq h$, and

$$T_0(x; l, h) = 0, \quad (5.30)$$

otherwise. This probability distribution expresses the certainty that a parameter x lies between l and h , and has equal probability of lying in any fixed-width subset of that domain. It is useful, for example, where x is a probability, and therefore must lie between 0 and 1, or where x is a measurement, quantized in units $h - l$ with an unknown origin by a digital meter, of a parameter $\frac{h+l}{2}$. In the rest of this section, an adapted version of the perfect top-hat

$$T(x; l, h) \frac{127}{128(h - l)}, \quad (5.31)$$

if $l \leq x \leq h$, and

$$T(x; l, h) = G\left(x; \frac{h + l}{2}, \frac{h - l}{5.32}\right), \quad (5.32)$$

otherwise, is used. This distribution has a probability $\frac{127}{128}$ of being in the top-hat region, and a probability density outside this region equal to a Gaussian of appropriate width [95, 96] for the probability integrated over this region to be $\frac{1}{128}$. Not only is this a more realistic belief density than a perfect top-hat, it provides a probability density gradient outside the top-hat region, which will help the leapfrog proposal density (section 5.3.4) to reduce the random walk behaviour of the metropolis method.

Prior Probability Distributions

Bayesian estimation of the parameters in a model, on the basis of experimental data, requires [89, 85, 52] the explicit statement of prior probability distributions, representing the beliefs that are held about the parameters, before the experimental data are examined. The author has made some remarks about the importance of this requirement elsewhere [10]. The prior

Parameter	Symbol	Prior Probability Distribution (Null Model)
Acceptance probability at front of polarimeter	a	$P(a M_N) = T(a; 0, 1)$
Channeltron i sensitivity perturbation, film j	p_{ij}	$P(p_{ij} M_N) = G(p_{ij}; 1, 0.05)$
Spin-averaged scattering probability, coefficient 0	Γ_0	$P(\Gamma_0 M_N) = T(\Gamma_0; 0, 1)$
Spin-averaged scattering probability, coefficient $k > 0$	Γ_k	$P(\Gamma_k M_N) = G(\Gamma_1; 0, 1/\xi^k)$
Sherman function, coefficient 0	S_0	$P(S_0 M_N) = T(S_0; -1, 1)$
Sherman function, coefficient $k > 0$	S_k	$P(S_k M_N) = G(S_k; 0, 2/\xi^k)$
Channeltron i average sensitivity	η_i	$P(\eta_i M_N) = T(\eta_i; 0.78, 0.89)$
Electrostatic potential, film 0	V_0	$P(V_0 M_N) = G(V_0; \Phi_{SS} - \Phi_{Cu}, \sqrt{\Delta\Phi_{SS}^2 + \Delta\Phi_{Cu}^2})$
Electrostatic potential, film $j > 0$	V_j	$P(V_j M_N) = G(V_j; \Phi_{SS} - \Phi_{Co}, \sqrt{\Delta\Phi_{SS}^2 + \Delta\Phi_{Co}^2})$
Weiss field, film 0	B_0	$P(B_0 M_N) = \delta(B_0)$
Weiss field, film $j > 0$	B_j	$P(B_j M_N) = \delta(B_j)$

Table 5.6: Parameters in the Null Model, with Their Prior Probability Distributions

Parameter	Symbol	Prior Probability Distribution (Main Model)
Acceptance probability at front of polarimeter	a	$P(a M_M) = T(a; 0, 1)$
Channeltron i sensitivity perturbation, film j	p_{ij}	$P(p_{ij} M_M) = G(p_{ij}; 1, 0.05)$
Spin-averaged scattering probability, coefficient 0	Γ_0	$P(\Gamma_0 M_M) = T(\Gamma_0; 0, 1)$
Spin-averaged scattering probability, coefficient $k > 0$	Γ_k	$P(\Gamma_k M_M) = G(\Gamma_k; 0, 1/\xi^k)$
Sherman function, coefficient 0	S_0	$P(S_0 M_M) = T(S_0; -1, 1)$
Sherman function, coefficient $k > 0$	S_k	$P(S_k M_M) = G(S_k; 0, 2/\xi^k)$
Channeltron i average sensitivity	η_i	$P(\eta_i M_M) = T(\eta_i; 0.78, 0.89)$
Electrostatic potential, film 0	V_0	$P(V_0 M_M) = G(V_0; \Phi_{SS} - \Phi_{Cu}, \sqrt{\Delta\Phi_{SS}^2 + \Delta\Phi_{Cu}^2})$
Electrostatic potential, film $j > 0$	V_j	$P(V_j M_M) = G(V_j; \Phi_{SS} - \Phi_{Co}, \sqrt{\Delta\Phi_{SS}^2 + \Delta\Phi_{Co}^2})$
Weiss field, film 0	B_0	$P(B_0 M_M) = \delta(B_0)$
Weiss field, film $j > 0$	B_j	$P(B_j M_M) = G(B_j; 0, k_B m_e T_C / e\hbar)$

Table 5.7: Parameters in the Main Model, with Their Prior Probability Distributions

probability distributions for this problem are presented in tables 5.6 and 5.7.

Justifications for these prior probability distributions follow.

- For the acceptance probability a , a uniform distribution over the range from 0 to 1 seems sensible, given that we know very little about the properties of this system, other than that the energy loss window at the front of the polarimeter is (table A.1) held constant throughout the experiments.
- The author and collaborators performed (section 5.5) experiments, before those described here, which provided a rough estimate of the extent of the drift in the channeltron detection efficiencies. The magnitude of the drift was found to be $\sim 10\%$ peak-to-peak, on a typical time-scale of the order of a few hours. The time-scale is represented in the division of the data set into chronologically contiguous subsets, which, by the design of the present experiment, coincide with single film thicknesses, and the magnitude in the standard deviation of the prior probability distributions over the time-dependent perturbations p_{ij} .
- The scattering probability Γ at the thorium foil must be in the range between zero and one, leading to the top-hat form for the distribution over Γ_0 .
- In the distributions over Γ_k , $k > 0$, the typical range of variation of the scattering probability over the energy scale of the experiments, due to any one term in the Taylor expansion, is asserted to be one.
- The Sherman function S at the thorium foil must be in the range between -1 and one, leading to the top-hat form for the distribution over S_0 .
- In the distributions over S_k , $k > 0$, the typical range of variation of the Sherman function over the energy scale of the experiments, due to any one term in the Taylor expansion, is asserted to be two.
- Because the front ends of the channeltrons are earthed, the electrons reach them with the same kinetic energy that they have at the sample. This means that the energies of the electrons, on arrival at the channeltrons, will range from 250 eV to 1500 eV. The detection efficiencies of channeltrons of the type used, in this energy range, are [66] between 0.78 and 0.89. Therefore, a top-hat probability distribution, with these as its limits, is used for η_i . The author does not believe that it is

worthwhile to create an energy-dependent model, since the uncertainty in the efficiency, at a particular energy, is [97, 66] comparable with its variation with energy, over this range.

- It can be assumed that, in as much as the sample is believed to be bulk, the bulk material in question is, for $j > 0$, cobalt, or, for the clean sample $j = 0$, copper, because the meaning of “bulk” is “top-most layer too thick for the electron beam to penetrate,” i.e. of a thickness that is large compared with 1 nm [83, 51]. Therefore, the electrostatic potential V_j is expected to be the difference in expected work function between stainless steel, which is the material from which the front end of the electron gun, which sets the zero of potential for the electrons, is constructed, and copper for $j = 0$, or cobalt for other film thickness indices j . The width of the distribution of V_j can be estimated by combining in quadrature the random errors $\Delta\Phi_l = 0.05\Phi_l$ [44] in measured work functions for the materials. The work functions are $\Phi_{SS} = 4.1$ V for stainless steel [49], $\Phi_{Cu} = 4.65$ V for copper [50], and $\Phi_{Co} = 5$ V for cobalt [50].
- For the copper surface $j = 0$ in the main model, and for all film thickness indices j in the null model, there are assumed to be no magnetic effects; the magnetic flux densities B_j acting on the electrons, in these cases, are certainly zero.
- The magnetic flux density B_j that affects the electrons is expected to be the same effective field, originating in the exchange interaction [31, 32], which creates ferro-magnetism. For the samples with a cobalt surface, $j > 0$, in the main model, a prior expectation of zero will be used, with the width of the prior probability distribution, i.e. the typical size of the flux density, being given by the order-of-magnitude estimate $\frac{k_B m_e T_c}{e\hbar}$ of the strength of this Weiss field that can [44] be obtained from the Curie temperature T_C . This is the only difference between the null and main models.

The parameters are taken, a priori, to be independent. Therefore, the prior probability density of the parameter vector

$$\begin{aligned}
 \mathbf{Q} &= (Q_1, Q_2, \dots, Q_{47}) \\
 &= (a, p_{10}, \dots, p_{17}, p_{20}, \dots, p_{27}, \Gamma_0, \dots, \Gamma_5, S_0, \dots, S_5, \eta_1, \eta_2, \\
 &\quad V_0, \dots, V_7, B_0, \dots, B_7)
 \end{aligned} \tag{5.33}$$

is

$$\begin{aligned}
P(\mathbf{Q}|M_n) &= \prod_{m=1}^{47} P(Q_m|M_n) \\
&= P(a|M_n) \left(\prod_{i=1}^2 \prod_{j=0}^7 P(p_{ij}|M_n) P(\eta_i|M_n) P(V_j|M_n) P(B_j|M_n) \right) \\
&\quad \times \left(\prod_{k=0}^5 P(\Gamma_k|M_n) P(S_k|M_n) \right). \tag{5.34}
\end{aligned}$$

There are also prior probabilities of each model, with any set of parameter values. These are taken to be

$$\begin{aligned}
P(M_N) &= P(M_M) \\
&= \frac{1}{2}. \tag{5.35}
\end{aligned}$$

The Likelihood

The data set D is the disjunction of the set D_0 of results of the present experiments (chapter 5,) the set D_Γ of published Γ calibration data (figure 5.6,) and the set D_S of published S calibration data (figure 5.7.)

For each measured electron arrival rate $f_m^{(i,j)} \in D_0$, the expectation of $f_m^{(i,j)}$, with a given parameter vector \mathbf{Q} , is $f_p^{(i,j)}$ (equation 5.25,) calculated using parameter vector \mathbf{Q} , and the values of E_b and F pertaining to the data point in question. There are two known, significant sources of uncertainty in this prediction. The first results from the Poisson process [84] of discrete electron arrivals at the channeltron, and introduces into the measured arrival rate a standard deviation $\sqrt{\frac{f_p^{(i,j)}}{256\tau}}$, where 256τ is the time interval, over which electrons are counted to obtain the arrival rate $f_m^{i,j}$. The second results from the standard deviation uncertainty ΔF , in the incident beam current F , and introduces into the measured arrival rate a standard deviation $\frac{f_p^{(i,j)} \Delta F}{F}$. These are combined in quadrature to give an overall standard deviation $\sqrt{\frac{f_p^{(i,j)}}{256\tau} + \frac{f_p^{(i,j)2} \Delta F^2}{F^2}}$. The likelihood function is then taken to be

$$P(f_m^{(i,j)}|\mathbf{Q}) = G \left(f_m^{(i,j)}; f_p^{(i,j)}, \sqrt{\frac{f_p^{(i,j)}}{256\tau} + \frac{f_p^{(i,j)2} \Delta F^2}{F^2}} \right). \tag{5.36}$$

For a given parameter vector, the measurements are assumed to be independent:

$$P(D_0|\mathbf{Q}) = \prod_{f_m^{(i,j)} \in D_0} P(f_m^{(i,j)}|\mathbf{Q}). \quad (5.37)$$

For each measured spin-averaged scattering probability $\Gamma_E \in D_\Gamma$, the expectation of Γ_E , with a given parameter vector \mathbf{Q} , is Γ (equation 5.23,) calculated using the Γ_k from \mathbf{Q} , and the value of W relevant to Γ_E . The uncertainty is introduced by the quantization, in units of $q_\Gamma = 0.001$, of the author's readings from the published [6] graphs. This gives

$$P(\Gamma_E|\mathbf{Q}) = T\left(\Gamma_E; \Gamma - \frac{q_\Gamma}{2}, \Gamma + \frac{q_\Gamma}{2}\right). \quad (5.38)$$

For a given parameter vector, the measurements are assumed to be independent:

$$P(D_\Gamma|\mathbf{Q}) = \prod_{\Gamma_E \in D_\Gamma} P(\Gamma_E|\mathbf{Q}). \quad (5.39)$$

For each measured Sherman function $S_E \in D_S$, the expectation of S_E , with a given parameter vector \mathbf{Q} , is S (equation 5.24,) calculated using the S_k from \mathbf{Q} , and the value of W relevant to S_E . As well as the published [6] uncertainty ΔS_E , uncertainty is introduced by the quantization, in units of $q_S = 0.025$, of the author's readings from the published [6] graphs: the standard deviation associated with this is $\frac{q_S}{\sqrt{12}}$. These are combined in quadrature, to give a standard deviation $\sqrt{\Delta S_E^2 + \frac{q_S^2}{12}}$. The likelihood is then taken to be

$$P(S_E|\mathbf{Q}) = G\left(S_E; S, \sqrt{\Delta S_E^2 + \frac{q_S^2}{12}}\right). \quad (5.40)$$

For a given parameter vector, the measurements are assumed to be independent:

$$P(D_S|\mathbf{Q}) = \prod_{S_E \in D_S} P(S_E|\mathbf{Q}). \quad (5.41)$$

For a given parameter vector, the three data sets are assumed to be independent:

$$P(D|\mathbf{Q}) = P(D_0|\mathbf{Q})P(D_\Gamma|\mathbf{Q})P(D_S|\mathbf{Q}). \quad (5.42)$$

Posterior Probability Distribution

The posterior probability distribution over the parameters in the null model (tables 5.6, 5.7) M_N is given by Bayes' theorem [89]:

$$P(\mathbf{Q}|D, M_N) = \frac{P(D|\mathbf{Q})P(\mathbf{Q}|M_N)}{P(D|M_N)}, \quad (5.43)$$

where

$$P(D|M_N) = \int_{\text{All } \mathbf{Q} \text{ space}} P(\mathbf{Q}|M_N)P(D|\mathbf{Q})d^{47}\mathbf{Q}. \quad (5.44)$$

Similarly, for the main model,

$$P(\mathbf{Q}|D, M_M) = \frac{P(D|\mathbf{Q})P(\mathbf{Q}|M_M)}{P(D|M_M)}, \quad (5.45)$$

where

$$P(D|M_M) = \int_{\text{All } \mathbf{Q} \text{ space}} P(\mathbf{Q}|M_M)P(D|\mathbf{Q})d^{47}\mathbf{Q}. \quad (5.46)$$

The posterior probabilities of the models are

$$P(M_N|D) = \frac{P(D|M_N)P(M_N)}{P(D)} \quad (5.47)$$

and

$$P(M_M|D) = \frac{P(D|M_M)P(M_M)}{P(D)}, \quad (5.48)$$

where

$$P(D) = P(M_N)P(D|M_N) + P(M_M)P(D|M_M). \quad (5.49)$$

Parameter Estimation and Model Comparison

The posterior probability distributions of section 5.3.4 constitute a complete description of the author's beliefs about the models and their parameters, once the data (chapter 5) are taken into account. However, it is a very unwieldy description, consisting as it does of two scalar fields defined on a 47-dimensional space. A summary is required for presentation. The author believes that the most useful summary will be to give, for each parameter Q_m , estimates of its posterior marginal expectations

$$\langle Q_m|D, M_N \rangle = \int_{\text{All } \mathbf{Q} \text{ space}} Q_m P(\mathbf{Q}|D, M_N) d^{47}\mathbf{Q} \quad (5.50)$$

and

$$\langle Q_m|D, M_M \rangle = \int_{\text{All } \mathbf{Q} \text{ space}} Q_m P(\mathbf{Q}|D, M_M) d^{47}\mathbf{Q}, \quad (5.51)$$

and of its posterior marginal standard deviations,

$$\sigma(Q_m|D, M_N) = \sqrt{\langle Q_m^2|D, M_N \rangle - \langle Q_m|D, M_N \rangle^2} \quad (5.52)$$

and

$$\sigma(Q_m|D, M_M) = \sqrt{\langle Q_m^2|D, M_M \rangle - \langle Q_m|D, M_M \rangle^2}, \quad (5.53)$$

where

$$\langle Q_m^2|D, M_n \rangle = \int_{\text{All } \mathbf{Q} \text{ space}} Q_m^2 P(\mathbf{Q}|D, M_n) d^{47} \mathbf{Q}. \quad (5.54)$$

The summary should also include the estimates of the model posterior probabilities $P(M_n|D)$ (equations 5.47, 5.48.)

If a means can be found of drawing samples $\mathbf{Q}^{(\text{pos},n,i,j)}$ from the distribution $P(\mathbf{Q}|D, M_n)$, where i runs from 1 to I , j runs from 1 to J , and the total number of samples is, therefore, IJ , $\langle Q_m|D, M_n \rangle$ can [48] be estimated by

$$\bar{Q}_m^{(\text{pos},n)} = \frac{\sum_{i=1}^I \bar{Q}_m^{(\text{pos},n,i)}}{I}, \quad (5.55)$$

where

$$\bar{Q}_m^{(\text{pos},n,i)} = \frac{\sum_{j=1}^J Q_m^{(\text{pos},n,i,j)}}{J}. \quad (5.56)$$

Similarly, $\sigma(Q_m|D, M_n)$ can [48] be estimated by

$$\sigma_m^{(\text{pos},n)} = \sqrt{\frac{IJ(\bar{Q}_m^{2(\text{pos},n,i)} - (\bar{Q}_m^{(\text{pos},n,i)})^2)}{IJ - 1}}, \quad (5.57)$$

where

$$\bar{Q}_m^{2(\text{pos},n)} = \frac{\sum_{i=1}^I \bar{Q}_m^{2(\text{pos},n,i)}}{I}, \quad (5.58)$$

and

$$\bar{Q}_m^{2(\text{pos},n,i)} = \frac{\sum_{j=1}^J ((Q_m^{(\text{pos},n,i,j)})^2)}{J}. \quad (5.59)$$

Similarly, if a means can be found of drawing samples $\mathbf{Q}^{(\text{pri},n,i,j)}$ from the distribution $P(\mathbf{Q}|M_n)$, where i runs from 1 to I , j runs from 1 to J , and the total number of samples is, therefore, IJ , $P(D|M_n)$ can [48] be estimated by

$$\bar{L}^{(\text{pri},n)} = \frac{\sum_{i=1}^I \bar{L}^{(\text{pri},n,i)}}{I}, \quad (5.60)$$

where

$$\bar{L}^{(\text{pri},n,i)} = \frac{\sum_{j=1}^J P(D|\mathbf{Q}^{(\text{pri},n,i,j)})}{J}. \quad (5.61)$$

All of these estimators are [90] non-Bayesian, i.e. they coincide exactly with Bayesian posterior expectations of the quantities being estimated, given

the samples, only for specific, but not specified, prior probability distributions over moments of the distribution $P(\mathbf{Q}|D, M_n)$. The estimators will, therefore, differ by an amount δ from the posterior expectations that would be obtained with explicit statements of plausible prior probability distributions over these moments, if this were technically feasible. Fortunately, however, the size of δ tends [10] to decrease with decreasing marginal likelihood, i.e. with increasing number of samples. Equally fortunately, when the inference process aims to estimate moments of a probability distribution, from samples from that distribution, a critical δ for each moment is made available, by the degree of variation implied by the higher moments, such that significantly smaller values of δ can be safely ignored. All this means that, for large numbers of samples, the non-Bayesian estimators are acceptable.

The means of obtaining samples is the leapfrog method. This is explained in detail in *Information Theory, Inference and Learning Algorithms* [90], where it is attributed to Skilling. Each iteration of the method consists of the application of a leapfrog proposal density, followed by the application of a Metropolis decision algorithm. For sampling from the posterior probability distribution, after the i th iteration, the method's state is a set of J parameter vectors $\mathbf{Q}^{(\text{POS}, n, i, j)}$, which are the samples to be used in the estimators. The leapfrog proposal density sets

$$\mathbf{Q}'^{(\text{POS}, n, i, j)} = 2\mathbf{Q}^{(\text{POS}, n, i, k)} - \mathbf{Q}^{(\text{POS}, n, i, j)}, \quad (5.62)$$

where, for each j , a k is chosen at random from the other $J - 1$ integers from 1 to J , with each of these being equi-probable. The Metropolis decision algorithm then works as follows:

- if $\frac{P(\mathbf{Q}'^{(\text{POS}, n, i, j)}|D, M_n)}{P(\mathbf{Q}^{(\text{POS}, n, i, j)}|D, M_n)} \geq 1$, then $\mathbf{Q}^{(\text{POS}, n, i+1, j)}$ is set to $\mathbf{Q}'^{(\text{POS}, n, i, j)}$. Otherwise,
- $\mathbf{Q}^{(\text{POS}, n, i+1, j)}$ is set at random, either to $\mathbf{Q}'^{(\text{POS}, n, i, j)}$, with probability $\frac{P(\mathbf{Q}'^{(\text{POS}, n, i, j)}|D, M_n)}{P(\mathbf{Q}^{(\text{POS}, n, i, j)}|D, M_n)}$, or to $\mathbf{Q}^{(\text{POS}, n, i, j)}$, with probability $1 - \frac{P(\mathbf{Q}'^{(\text{POS}, n, i, j)}|D, M_n)}{P(\mathbf{Q}^{(\text{POS}, n, i, j)}|D, M_n)}$.

An analogous process is used to draw samples $\mathbf{Q}^{(\text{PRI}, n, i, j)}$ from the prior probability distribution.

As part of the preparation of the present thesis, the author has written Perl code that implements the leapfrog method; in the transparent copy of this thesis, the code for the null model M_N is in the file `null`, and the code for the main model M_M is in the file `main`. As far as the author has been able to discover, the present thesis is the first use of the leapfrog method to infer parameters and model likelihoods from real experimental data. Some

further details are needed to define the particular version of the leapfrog method used in this thesis:

- Initial vector sets $\mathbf{Q}^{(\text{pri},n,0,j)}$ and $\mathbf{Q}^{(\text{pos},n,0,j)}$ are chosen, centred around the analytically-derived prior expectation values $\langle Q_m | M_n \rangle$ of the parameters. The displacements of the J initial vectors from the prior expectation are picked randomly from a perfect top-hat distribution out to a maximum size of each displacement component, which is the product of a constant factor α_{pri} or α_{pos} , and the prior standard deviation $\sigma(Q_m | M_n)$ of the relevant parameter. That is to say, $Q_m^{(\text{pri},n,0,j)}$ is drawn from a distribution

$$T_0(Q_m^{(\text{pri},n,0,j)}; \langle Q_m | M_n \rangle - \alpha_{\text{pri}}\sigma(Q_m | M_n), \langle Q_m | M_n \rangle + \alpha_{\text{pri}}\sigma(Q_m | M_n)),$$

and $Q_m^{(\text{pos},n,0,j)}$ is drawn from a distribution

$$T_0(Q_m^{(\text{pos},n,0,j)}; \langle Q_m | M_n \rangle - \alpha_{\text{pos}}\sigma(Q_m | M_n), \langle Q_m | M_n \rangle + \alpha_{\text{pos}}\sigma(Q_m | M_n)).$$

It has [90] been shown that the leapfrog method rapidly grows an initial vector set that is narrower than the distribution, from which one wishes to sample. However, the author does not know of any analogous proof that the algorithm can shrink an initial vector set that is broader than the distribution, from which one wishes to sample. Therefore, the initial vector set, for sampling from the prior probability distribution is made a factor of $\exp(1)$, in each dimension, narrower than the prior probability distribution. An attempt is made to achieve the same for the posterior probability distribution, using a guess at the width of the posterior probability distribution. This gives $\alpha_{\text{pri}} = \frac{\sqrt{3}}{\exp(1)}$, and $\alpha_{\text{pos}} = \frac{\sqrt{3}}{(|D|-A)\exp(1)}$, where $|D| = 1018$ is the number of data points, and the number of adjustable parameters is $A = 39$ for the null model M_N , and $A = 46$ for the main model M_M , because a parameter whose prior probability distribution is a Dirac delta function is not truly adjustable. One further complication is that it is necessary to ensure that, in each dimension, the width of the initial vector set is comfortably greater than the quantum of floating point numbers of the order of magnitude of $\langle Q_m | M_n \rangle$. Mantissae have 53 bits ‘on typical hardware’ [98]. One bit is assumed to be taken up by the sign, and four bits are left, to provide 16 possible starting ordinates, i.e. if the half-width of the top-hat distribution is less than $2^{-48} |\langle Q_m | M_n \rangle|$, it is adjusted to $2^{-48} |\langle Q_m | M_n \rangle|$.

- The author believes that the number J of state vectors maintained simultaneously, in the Monte Carlo algorithm, must be at least the

number A of adjustable parameters. This is because every state vector ever obtained will be some linear combination of the J initial state vectors, and to obtain a representative sample, the J initial state vectors must, therefore, span the parameter space. In this thesis, therefore, $J = 2A$ is chosen, rather than the $J = 6$ or $J = 12$ suggested in *Information Theory, Inference and Learning Algorithms* [90].

- The author also believes that having a large value of J will ameliorate the problem, noted by MacKay [90], of the state vectors in the leapfrog algorithm becoming stuck permanently at one vector set, after it has converged, because, as long as the parameter of interest varies smoothly in \mathbf{Q} space, as the Q_m must, if $J \gg 1$, there will be a reasonable sampling of the distribution even if all the individual state vectors are stationary. $P(D|\mathbf{Q}, M_n)$, however, might not vary smoothly in \mathbf{Q} space. Therefore, the quantitative estimates of $P(D|M_n)$ obtained herein should be treated with some scepticism.

The Parameter Estimates

The convergence of the estimates of some of the various parameters, in the main and null models, is displayed in figures 5.11, 5.12, and 5.13.

Having presented and discussed the results of the main experiments, it is now time to present results of some similar, earlier experiments; the primary use of these experiments will not be in inferring physical properties of samples, but in identifying imperfections in the experimental methods, the solutions to which motivate, and are built into, the experimental methods above.

5.4 Intermediate Experiment 1

A preliminary experiment, related to this thesis, was described in *Mott Polarimetry at the Cavendish Laboratory* [8]. That report presents Mott asymmetries of reflected electron beams from a $Cu/Mn/Co/Cu(001)$ structure, using the estimator of equation 5.16. Those measurements are of much lower precision than the measurements presented in this thesis (chapter 5, section 5.2,) and the report remains of interest primarily for its list of the adaptations that were made to the polarimeter, and to the measurement technique, in order to bring it into a sufficiently functional condition to undertake the preliminary experiment. That list is repeated in section 2.11 of this thesis. Similarly, this section, and section 5.5, are concerned with the polarimetry measurements that were performed after the preliminary experiment, and

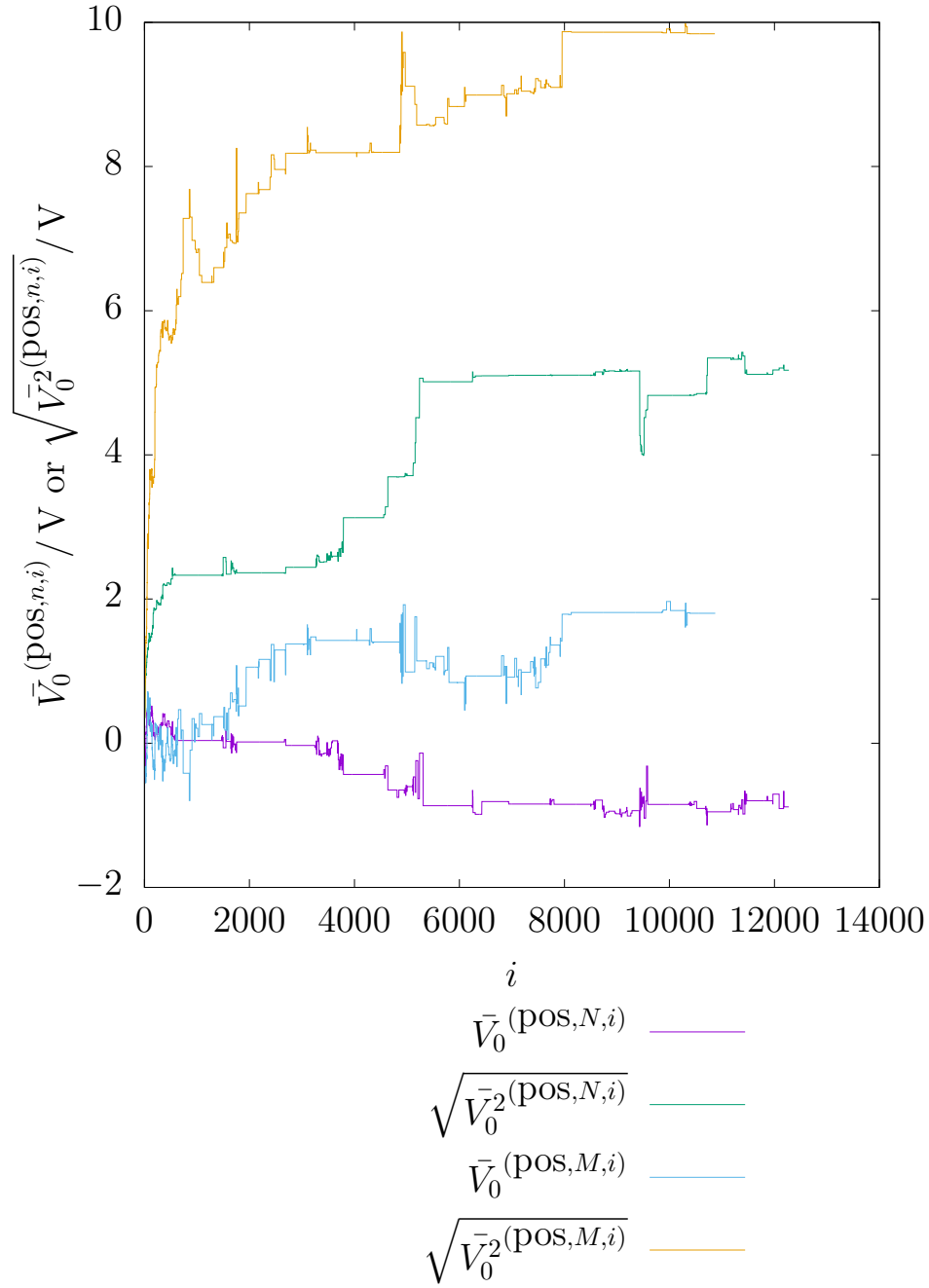


Figure 5.11: The Convergence of the Electrostatic Potential with No Film, Displayed as a Graph of the Iteration Mean and Root Mean Square of the Potential, for Each Model, Against Iteration Number

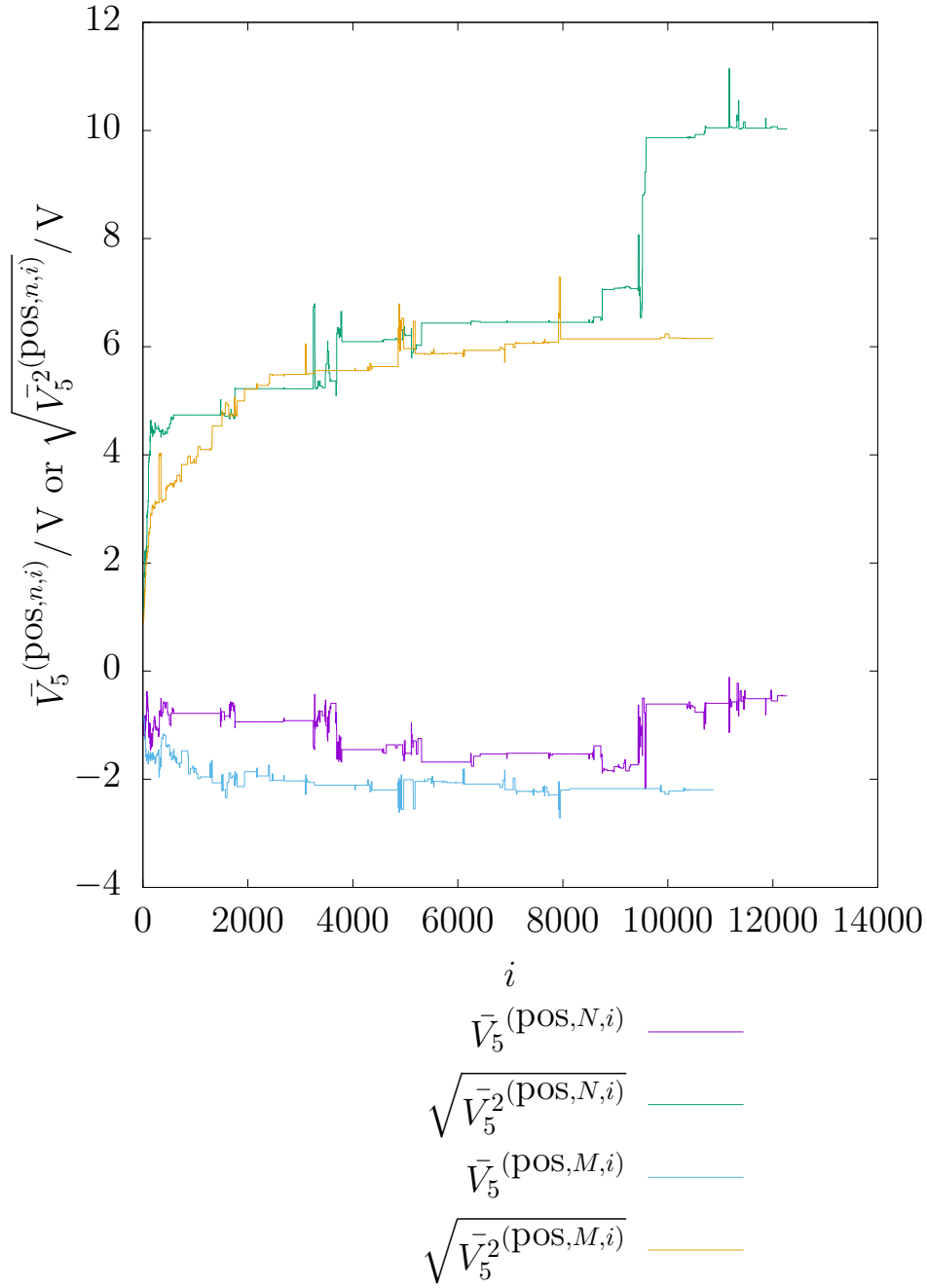


Figure 5.12: The Convergence of the Electrostatic Potential with Film Thickness 5, Displayed as a Graph of the Iteration Mean and Root Mean Square of the Potential, for Each Model, Against Iteration Number

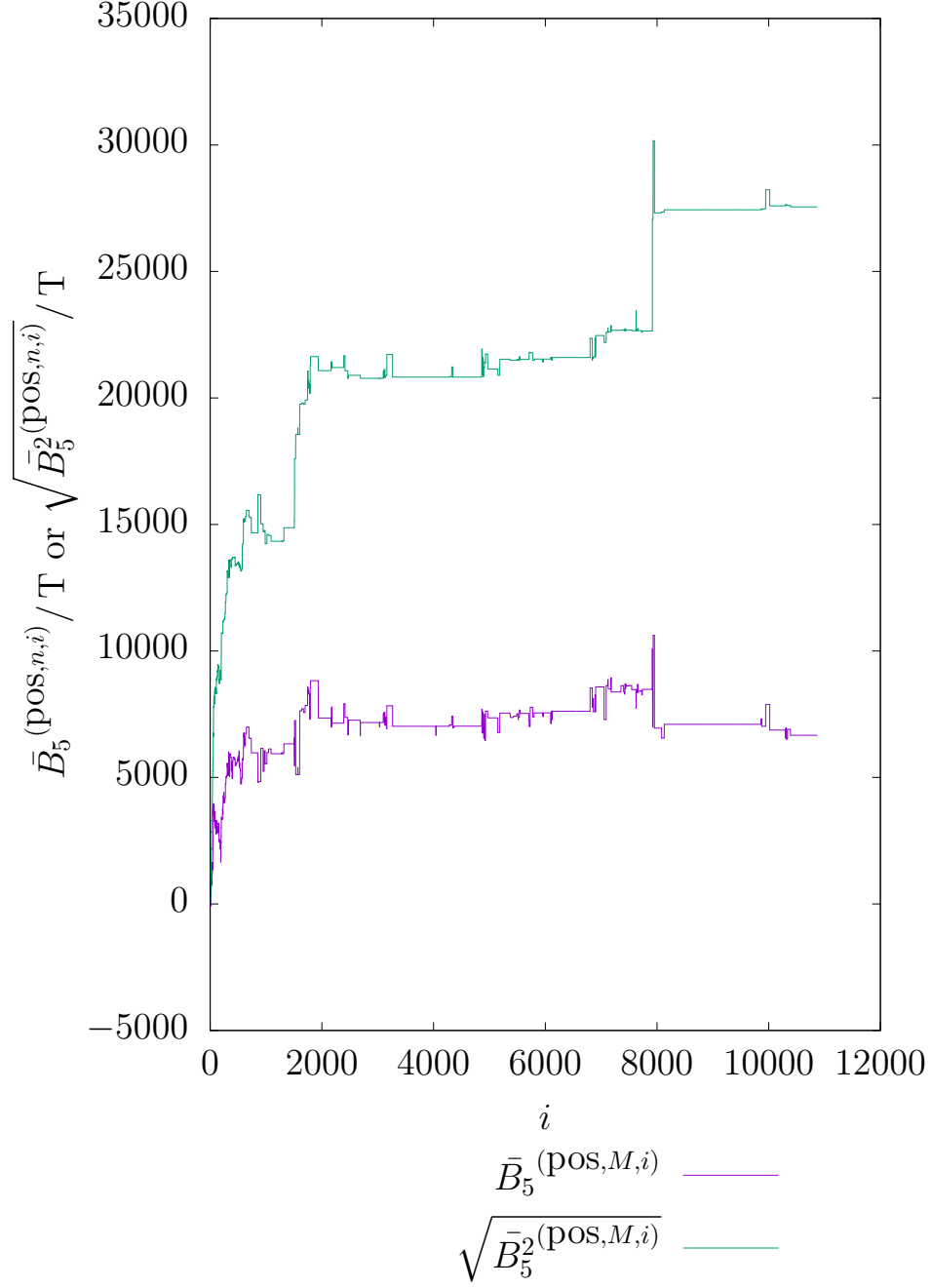


Figure 5.13: The Convergence of the Magnetic Flux Density with Film Thickness 5, Displayed as a Graph of the Iteration Mean and Root Mean Square of the Flux Density, for the Main Model, Against Iteration Number

Substrate Index	Thickness Index	Thickness/ $\mu\text{A s}$	Thickness/ pm
2	0	0	0
2	1	9.01 ± 0.18	700 ± 100
2	2	14.29 ± 0.27	1110 ± 160
1	1	17.4 ± 5	1360 ± 430
2	3	23.12 ± 0.42	1800 ± 260
2	4	32.57 ± 0.54	2540 ± 360
2	5	41.66 ± 2.79	3250 ± 510

Table 5.8: The Cobalt Thicknesses Used in the Intermediate Experiments Described in This Appendix

before the main experiment of part III, the technical adaptations that were discovered to be necessary, as a result of those intermediate measurements, and the implementation of those adaptations.

After the preliminary experiment, considerable resources were devoted to equipment repairs, and to safety-related upgrades, which did not constitute adaptations of the polarimeter, or of the measurement technique. Once this was done, concerted efforts began to produce more decisive polarized electron reflection measurements than those in that report, starting with pilot experiments on *Co/Cu*(001) structures, without the added manganese; compared with most of the preliminary measurements, lower beam energies were used in the intermediate experiments, leading to more intense reflected beams, and greater precision in the current (or electron arrival rate) measurements at the channeltrons.

In the first such intermediate experiment, the method was very similar to that in chapter 4.4, with the significant differences being that the channeltrons were used as Faraday cups, measuring continuous currents, instead of counting individual electrons, and that the position of the sample was only set to a precision of 1 mm in translational degrees of freedom, and 1° in the rotational degree of freedom with the vertical rotation axis. Some of the results are displayed in table 5.8 and figures 5.14, 5.15, and 5.16. Readers who would prefer to see the full data set, rather than just examples, might like to down-load the transparent copy of this thesis, and check out RCS version 18.1.

In addition to the polarized electron reflection measurements, Auger electron spectroscopy and low-energy electron diffraction were used for structural characterization of some of these samples. They revealed that the copper surfaces produced by a sputtering and annealing process of similar extent to that in chapter 5 were clean and well ordered, and that a significant amount of

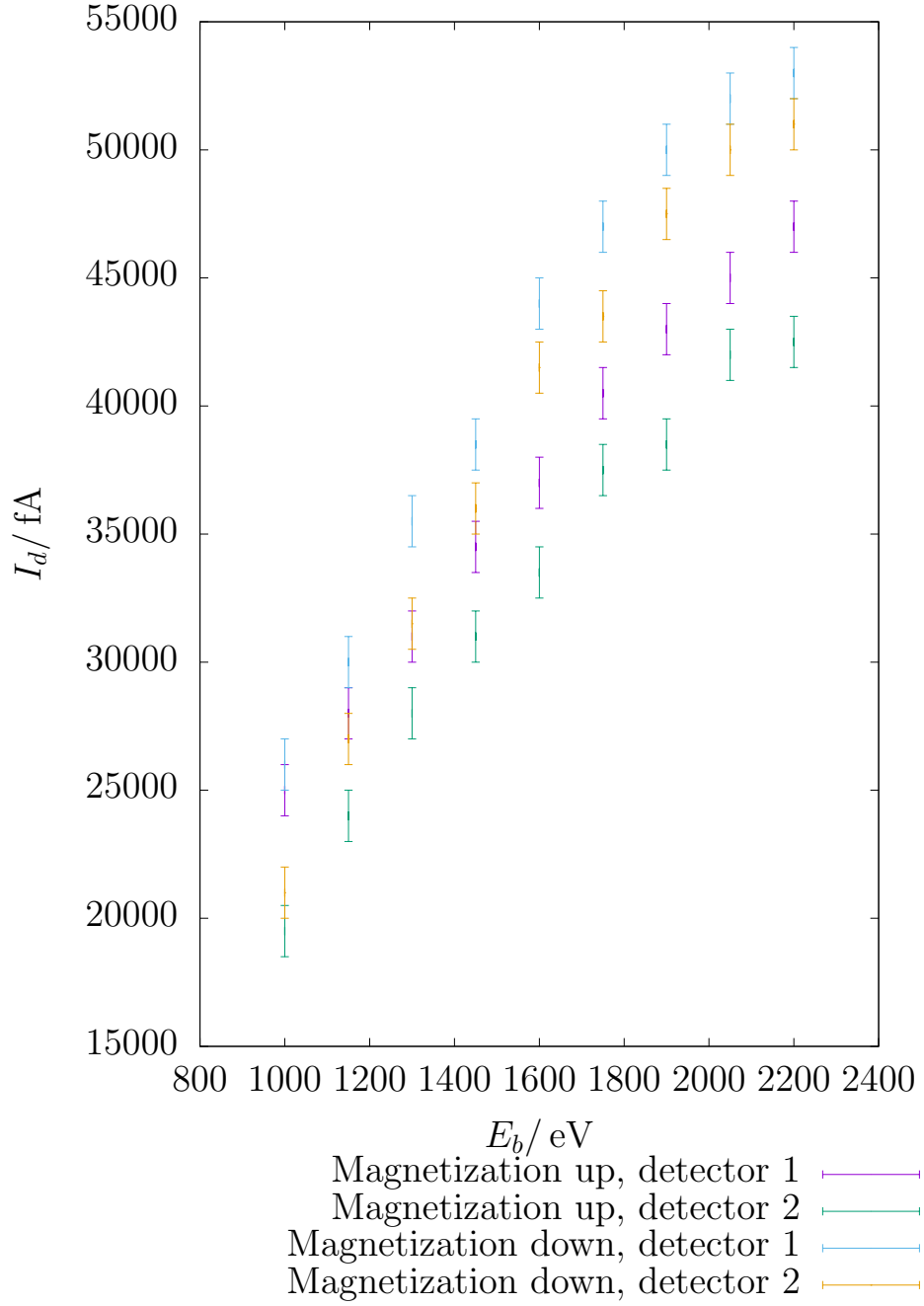


Figure 5.14: Measured Current at Detectors against Incident Beam Energy for an Incident Beam Current of $(108.8 \pm 0.2) \mu\text{A}$, Both Sample Magnetization Directions, and Thickness 3 $((1800 \pm 260) \text{ pm})$ on Substrate 2.

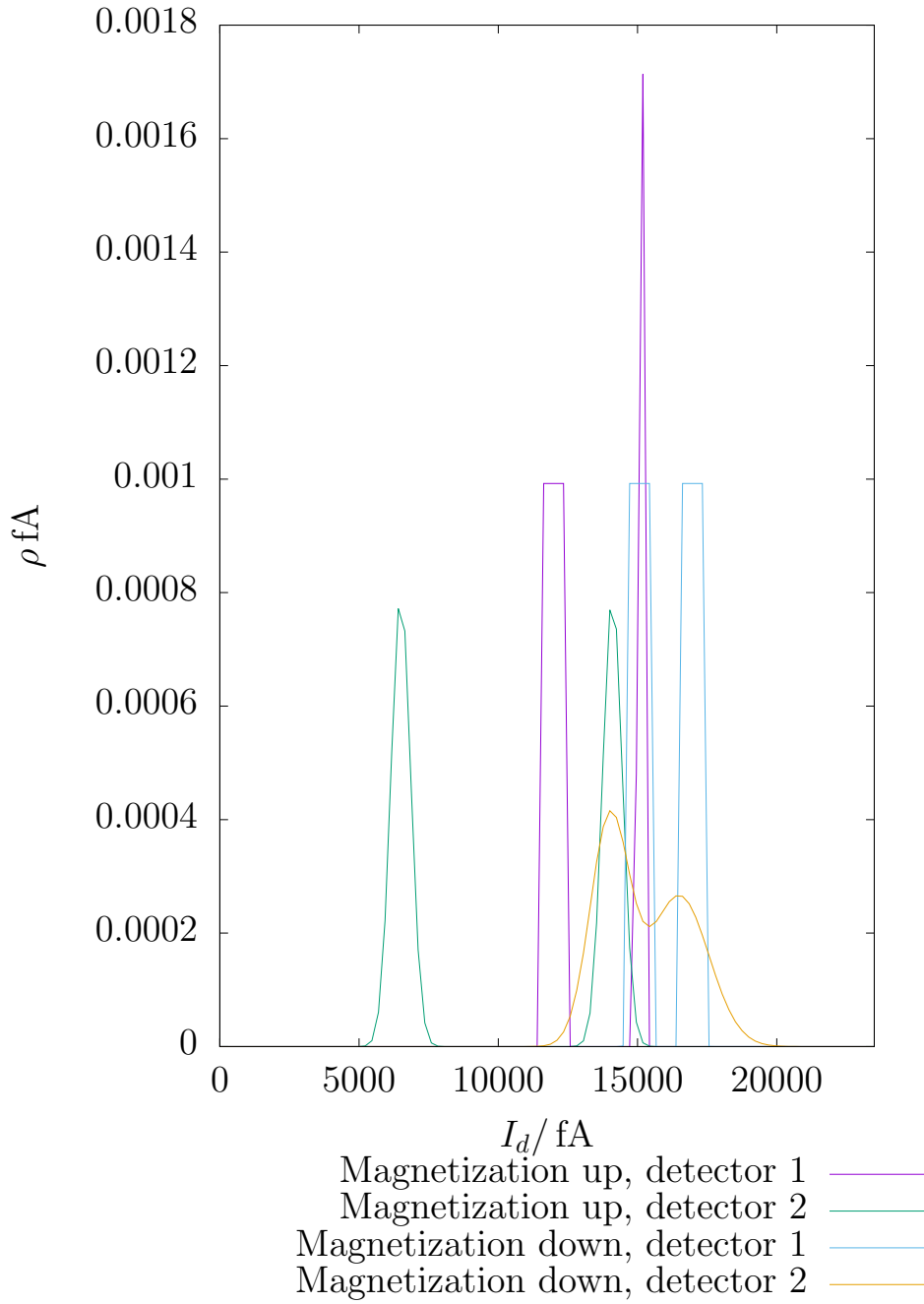


Figure 5.15: Histogram Showing the Sum of the Likelihood Density Functions, for Multiple Detector Current Measurements, against Current at the Detectors, for an Incident Beam Energy of (1000 ± 0.29) eV, an Incident Beam Current of (108.65 ± 0.4) μA , Both Sample Magnetization Directions, and Thickness 4 $((2540 \pm 360)$ pm) on Substrate 2.

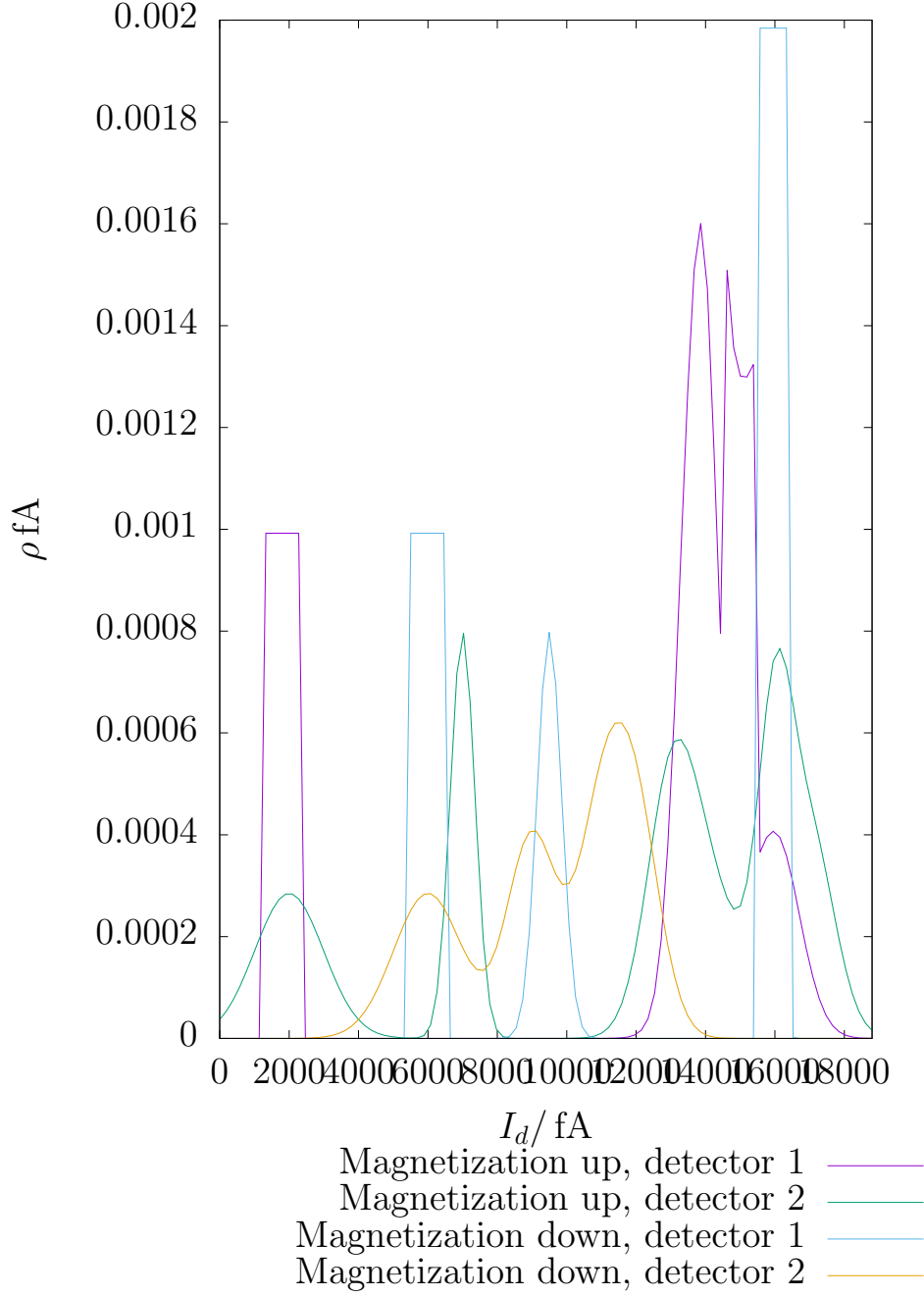


Figure 5.16: Histogram Showing the Sum of the Likelihood Density Functions, for Multiple Detector Current Measurements, against Current at the Detectors, for an Incident Beam Energy of $(1000 \pm 0.29) \text{ eV}$, an Incident Beam Current of $(108.25 \pm 0.04) \mu\text{A}$, Both Sample Magnetization Directions, and Thickness 5 $((3250 \pm 510) \text{ pm})$ on Substrate 2.

cobalt was being deposited.

A number of features of the data stand out. Firstly, instead of being downward sloping and convex \cup , the electron arrival rate as a function of beam energy is upward sloping and concave \cap . After independent tests of the voltage arriving at the retarding grids (figure 3.1,) this was attributed to the power supply in use for the retarding grids having the wrong polarity to maintain a constant energy loss window, resulting in an energy loss window that increased at twice the rate of increase of the incident beam energy, and a Γ (figure 5.6) that increased with increasing incident beam energy. A new power supply, with the correct polarity, was procured for the experiments described in section 5.5 and section 4.4. Secondly, the electron arrival rate for a given set of conditions was not reproduce-able, as is vividly displayed in the histograms of the detector current, which are clearly multi-modal. After independent tests of the current arriving at a given detector, as the sample position was varied, this was attributed to the variation in position of the sample between different measurements, and a corresponding variation in the fraction of the specularly reflected beam that was accepted at the front of the polarimeter. Fortunately, the same tests indicated that a precision of 0.1 mm in the translational degrees of freedom, and 0.1° in the rotation about the vertical axis, which was feasible with the available equipment (figure 4.5,) would be adequate to render this effect negligible. Thirdly, at the low incident beam energies, where the energy loss window was in the region where S is large enough to provide spin sensitivity (figure 5.7,) Γ was so small as to stretch the limits of the sensitivity of continuous current measurements. For subsequent experiments (section 5.5, section 4.4,) therefore, a move was made to single electron counting. To succeed in this move required the procurement and installation of new channeltrons.

5.5 Intermediate Experiment 2

In the second intermediate experiment, the method was very similar to that in chapter 4.4, with the significant differences being that longer dwell times were used, and more electron counts were recorded, resulting in an experiment that lasted around 17 hours for each film thickness, rather than the 2 hours or so of the experiment in part III. Some of the results are displayed in table 5.9, and figures 5.17 and 5.18. A sample described as “slightly dirty” has been left in non-UHV conditions (gas pressure greater than 10 pbar) for a few hours, and a sample described as “very dirty” has been left in non-UHV conditions for around a day. Readers who would prefer to see the full data set, rather than just examples, might like to down-load the transparent copy of this thesis,

Substrate Index	Thickness Index	Thickness/ $\mu\text{A s}$	Thickness/ nm
3	0	0	0
3	1	53 ± 47	4.1 ± 3.7
4	0	0	0
6	0	0	0
8	0	0	0
5	1	108.7 ± 7.2	8.5 ± 1.3
7	1	108 ± 14	8.4 ± 1.6

Table 5.9: The Cobalt Thicknesses Used in the Intermediate Experiments Described in This Appendix

and check out RCS version 18.1.

In addition to the polarized electron reflection experiments, one of the author’s colleagues confirmed using MOKE measurements that the films on substrates 5 and 7 were ferromagnetic [3].

In many cases, the electron arrival rate appears not to be a smooth function of the incident beam energy. Inspection of the detailed data sets, based on the counts in single periods of τ , rather than of 256τ , reveals that this is associated with a gradual variation in time of the count rate, for fixed conditions⁶. The variations are tentatively attributed to drift in the detection efficiencies of the channeltrons, and have an amplitude of approximately 10% of the average sensitivity peak-to-peak, on a time-scale of the order of a few hours. This is the reason for much faster experiments being used in the main experiment of this chapter.

⁶These detailed data sets are available in the transparent copy of this thesis, in the files whose names contain the word “detailed.”

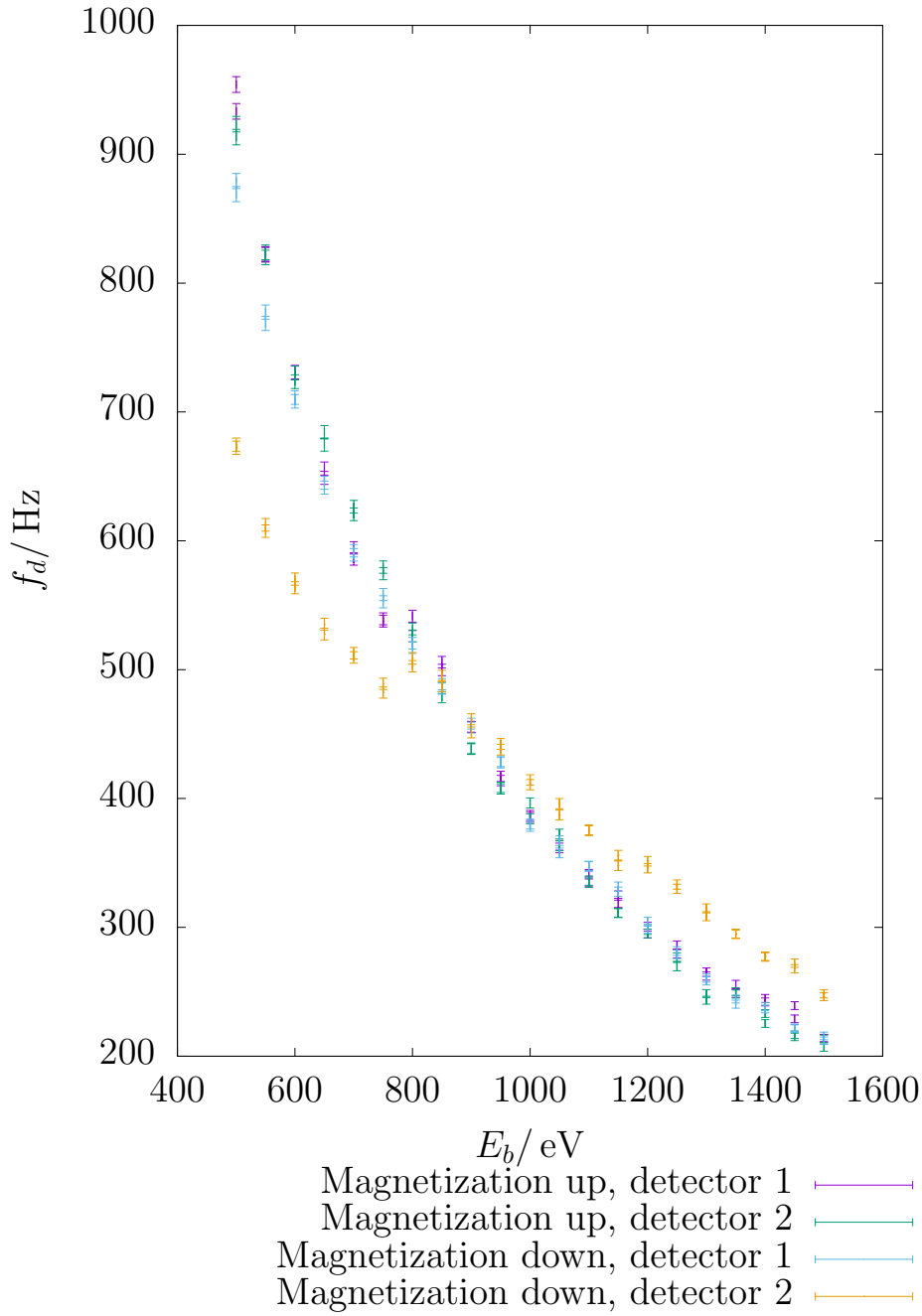


Figure 5.17: Measured Electron Arrival Rate at Detectors against Incident Beam Energy for an Incident Beam Current of $(6 \pm 0.029) \mu\text{A}$, Both Sample Magnetization Directions, and Substrate 4 with No Film. These data have previously appeared in *Electron Spin Polarimetry Studies of Ultra-Thin Magnetic Films* [3].

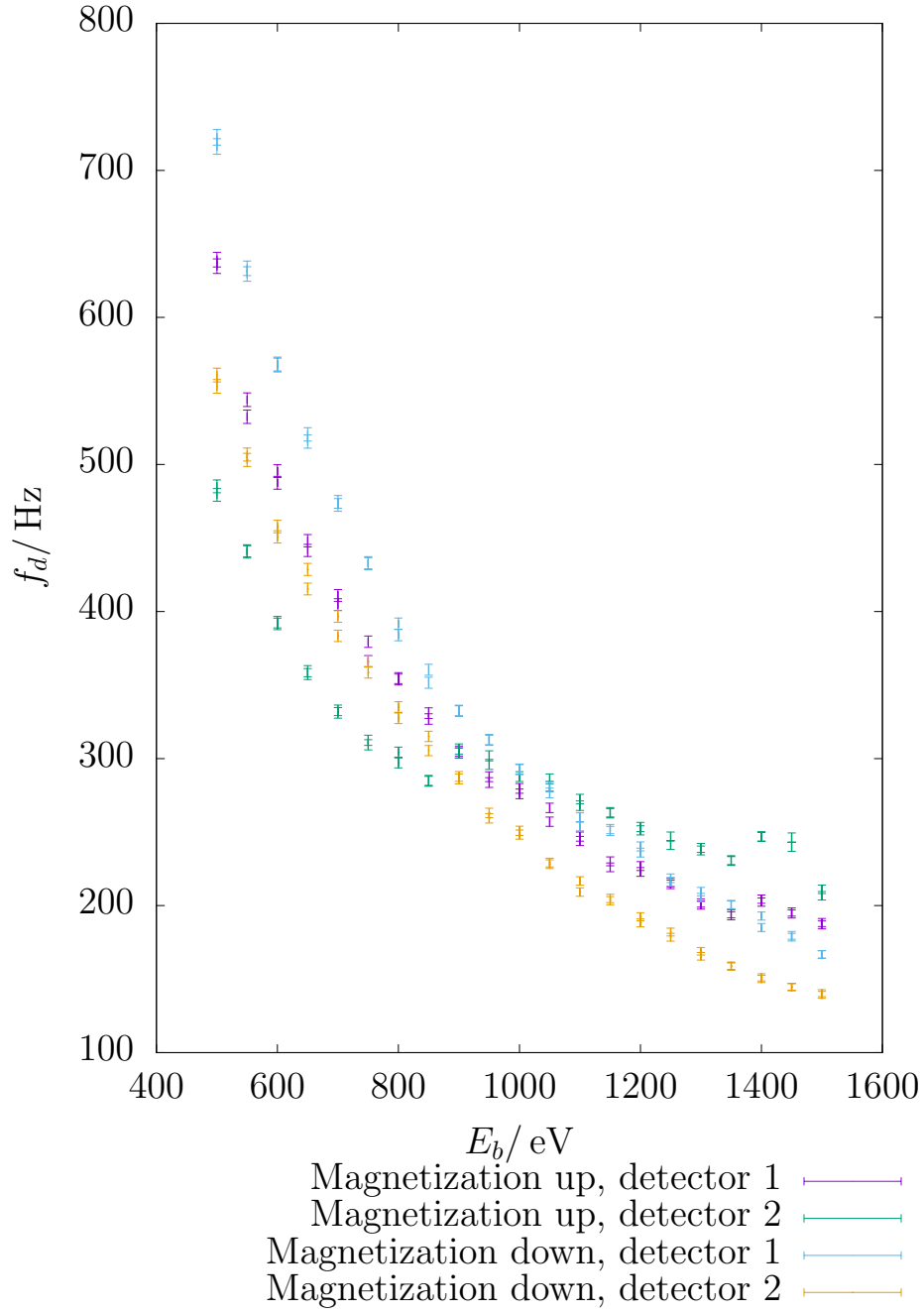


Figure 5.18: Measured Electron Arrival Rate at Detectors against Incident Beam Energy for an Incident Beam Current of $(6 \pm 0.029) \mu\text{A}$, Both Sample Magnetization Directions, and the Film $((8.4 \pm 1.6) \text{ nm})$ on Substrate 7. These data have previously appeared in *Electron Spin Polarimetry Studies of Ultra-Thin Magnetic Films* [3].

Chapter 6

Conclusions

Having presented and analysed the experimental results, it is time to summarize the conclusions that can be drawn from these results.

1. A non-zero Weiss field in the cobalt films has been detected; according to the Bayesian model comparison method, the experimental data rule out the null hypothesis, in which no such field has been detected, very strongly indeed, leaving it with a posterior probability of $0.34 \times 10^{-2014444631}$; this is about as firm a conclusion as it is conceivable to obtain, although properties of the Monte Carlo method used to estimate this probability suggest that some caution should be applied to the sheer size of the number.
2. The traditional estimator of the Mott asymmetry, and therefore of the reflected electron beam's spin polarization, provides well-defined, mostly non-zero values, indicating, in support of the last aforesaid Bayesian conclusion, that, despite the systematic error in the electron arrival rates, described below, the experiments have successfully detected the cobalt's Weiss field.
3. The experimental results can be used to estimate quantitatively the electrostatic potential V and Weiss field B in the samples; the estimates obtained, using the Bayesian parameter estimation method, are shown in figures 5.9 and 5.10. As can be seen from the figures, the estimates produced are extremely imprecise, i.e. the quoted standard deviation random errors in them are very large. The bulk of the large random error does not result from the posterior probability distribution, over the electrostatic potential or Weiss field, having a wide peak, but rather from this probability distribution having two widely-separated peaks, associated with the fact that the theoretical equation

2.8, when inverted to give the ratio $\frac{B}{V}$, as a function of the measurable reflected beam polarization, gives two solutions for $\frac{B}{V}$, for any given polarization; however, the moderately large random errors found in the traditional estimators of Mott asymmetry, related to the fact that the measured beam polarization is, in some sense, a small difference between two large numbers (the spin-up and spin-down currents,) suggest that each of the two peaks will itself be quite broad. Ironically, this lack of precision contributes positively to the ability to draw such an immensely firm conclusion that a non-zero Weiss field has been detected; underlying the Occam's razor that implements [85, 52] itself automatically in Bayesian statistics is the idea that a model should not be allowed to use information from experimental data to fine-tune its adjustable parameters, then recycle the same information to support it against other models. In the problem at hand, the model with extra adjustable parameters (non-zero Weiss fields in the cobalt films) does not significantly fine-tune those parameters using the experimental data, as is evident from the large residual random errors in those parameters. Therefore, Occam's razor does not significantly penalise this model, relative to the simpler model with the Weiss fields fixed at zero.

4. The spin polarization produced by the cobalt's Weiss field, as estimated in traditional fashion, is of a similar order of magnitude ($\sim 10\%$) to that found by other workers in various independent laboratories, using polarized electron reflection from other ferro-magnetic transition metals (section 2.10.)
5. There is some strong evidence that the stray magnetic field of the sample (or of some part of the sample holder) is significantly affecting the electron trajectories, creating a magnetization-dependent systematic error in the measured electron arrival rates at the Mott polarimeter's detectors.

The genuine effect of the cobalt's Weiss field can be detected, even in the presence of the systematic error due to stray magnetic fields, because the two have significantly different signatures in the electron arrival rates at the channeltrons. When the sample magnetization is reversed, the characteristic behaviour caused by the stray-field systematic error is for the electron arrival rates, at the two channeltrons, to change by the same factor, in the same sense, i.e. either both increase, or both decrease. The characteristic behaviour caused by a genuine spin polarization, produced by the cobalt's Weiss field, on the other hand, is for the electron arrival rates, at the two channeltrons,

to change by the same factor, in opposite senses, i.e. one increases and the other decreases. It was also this dissimilarity in signatures that allowed the systematic error to be noticed in the first place (table 5.3.)

In physical terms, the various methods used to analyse the data, namely the least-squares curve fitting of chapter 5, the asymmetry estimation of section 5.2, and the Bayesian inference of section 5.3 are all seeking the same effect, notwithstanding their substantial differences of statistical approach. All of them are testing for the electron arrival rates changing, on sample magnetization reversal, by the same factor in opposite senses. All of them are, therefore, sensitive to genuine spin polarizations, rather than to the stray-field systematic error, and all of them declare decisively that they have found such polarizations.

Of course, it is possible for both a genuine polarization and a stray field to occur simultaneously, and for their effects to be superimposed on one another. This appears to be the case in the experiments discussed in the present thesis. In this case, the systematic error in the electron arrival rates, caused by the stray field, has the following two effects.

1. Quantitative estimation of the polarizations, and therefore of the electro-magnetic parameters of the sample, by any of the data processing methods, is rather imprecise, i.e. has a large random error; however, this effect does not dominate the standard deviation random errors found in the estimates of electro-magnetic parameters, the bulk of which result from the double-valued nature of equation 2.8, when inverted to give electro-magnetic parameters as a function of spin polarization.
2. Visual inspection of the electron arrival rate data cannot easily pick out the individual effects (genuine spin polarization and stray field) from the superposition of the two.

It would, therefore, be much better if a way were found to eliminate the stray field, both to make the essential physical process of spin polarization by the exchange interaction more obvious visually, and to improve quantitative estimation of the Weiss field involved. Lind [65] found such a method for his particular experimental configuration, which involved following the field applied to magnetize the sample with a smaller applied field, in the opposite direction. It is, however, unclear how Lind determined that this method was a success, what physical mechanism allows the technique to work, and whether it will be applicable to experimental apparatus other than Lind's, such as the apparatus used for the present thesis.

Having drawn conclusions from the experimental results hereinbefore presented, some suggestions will now be given as to future research directions

related to the work in this thesis.

6.1 Suggestions for Further Work

- It would be intriguing to attempt to repeat Lind’s [65] method of eliminating the stray-field systematic error, by following the applied field used to set the sample magnetization direction with a smaller applied field in the opposite direction. As well as experimental reproduction of the technique, some theorizing would be in order, in the hope of understanding the physical mechanisms behind it.
- As a complement to attempts to eliminate the spatial deflection of the electron beam by a stray field from the sample or sample holder, there may be benefits in attempting to use this spatial deflection, along with spatially-resolved detection of the reflected beam, as an alternative means of determining a sample’s magnetic state using an electron beam.
- The numerical method, presented in this thesis, for obtaining summary data about the Bayesian posterior probability distributions, given the experimental data presented here, has performed disappointingly: it was very slow to run, taking CPU time of the order of a month to reach the conclusions presented here, and even after this time, there remains some doubt over whether it has reached a final conclusion on the marginal likelihoods used for model comparison, given that the likelihood function may not vary smoothly in parameter space. The slowness is in large part due to the many extra adjustable parameters, which have had to be inserted into the physical models, to handle the systematic errors now attributed to stray magnetic fields, and experimental techniques that eliminate these errors may resolve the problems with the numerical method. Nevertheless, there may be benefits in exploring alternative numerical methods, particularly if it is possible to increase the simplicity of their implementation by using adaptations of widely-available fitting software, rather than having to program a Markov chain Monte Carlo method anew; since completing the analysis herein presented, the author has, in the course of a separate experimental project, made considerable progress in devising means whereby, with a little algebra, ubiquitous chi-squared fitting routines can be used for Bayesian parameter estimation and model comparison.
- It will soon be necessary to consider what kinds of samples it is most interesting to examine with the polarized electron reflection technique;

the $Co/Cu(001)$ structure considered in this thesis was chosen primarily as a trial system, for development of the instrumentation. Above, the $c(2 \times 2)$ surface alloy of manganese on a cobalt (001) surface, with a copper substrate, was also mentioned as a candidate system for examination by polarized electron reflection. The author would characterize the motivation for experiments on this alloy as aesthetic: the wish to peer deeper into a beautiful and unusual system. The author has discussed with colleagues a number of other combinations of copper, cobalt, and manganese, which hold similar interest. However, as has been discussed elsewhere [10], the author now takes the view that the scientific value of experimental results stems primarily not from their aesthetic appeal, but from their ability to help policy-makers reach better decisions. In the case of research in magnetic film structures, the most relevant policy-makers are managers in the magnetic data storage industry, and the most relevant decisions are those about which systems of magnetic materials to include in future hard discs, read heads, and magnetic random access memories. The author believes that the time is ripe to consult managers in this industry about how they can use information about the Weiss fields of materials in multi-layer structures, and what multi-layer structures are most important to them.

Appendix A

Fine Details of the Experimental Method

A.1 Procedure for Placing the Sample in a Previously Determined Position

1. The three linear motion drivers, and the one of the two rotational motion drivers with a vertical rotation axis, attached to the sample (section 4.1,) were used to position the sample in the previously determined position, to the nearest tenth of a millimetre in the each of the three translational dimensions, and to the nearest tenth of a degree in the rotational dimension. The reasons for choosing this level of precision are discussed in section 5.4.

A.2 Procedure for Magnetizing a Sample

The purpose of this procedure is to set the magnetization direction of the sample.

1. The sample was placed, according to the procedure in appendix A.1, in a position that had previously been determined, by visual inspection, to allow an electromagnet consisting of a pair of Helmholtz coils to be raised, so that the sample was at its centre, without placing damaging stresses on the sample or surrounding apparatus (section 4.1.)
2. The electromagnet was raised, so that the sample was at its centre.
3. A current of (4.5 ± 0.04) A, equivalent [37] to a field of (17.9 ± 0.16) kA m⁻¹, was passed through the electromagnet for (10 ± 2) s. The sign of the

Electrode	Voltage
Front grids	$(-100 \pm 1) \text{ V} - \frac{E_b}{e}$
First lens	$(1.7 \pm 0.005) \text{ kV}$
Second lens	$(1 \pm 0.005) \text{ kV}$
Thorium foil	$(20.5 \pm 0.00725) \text{ kV} - \frac{E_b}{e}$
Focus electrodes	$(1.5 \pm 0.005) \text{ kV}$
Retarding grids	$(-200 \pm 1) \text{ V} - \frac{E_b}{e}$
Channeltron front ends	$(0 \pm 1) \text{ V}$
Channeltron anodes	$(2.2 \pm 0.005) \text{ kV}$

Table A.1: The Voltages, Relative to Earth, on the Electrodes of the Mott Polarimeter, During the Polarized Electron Reflection Experiment

current was chosen to obtain the required direction (up or down) of the magnetic flux density.

4. The electromagnet was lowered away from the sample.

A.2.1 Procedure for Conducting Polarized Electron Reflection Measurements on One Magnetization Direction

The purpose of this procedure is to measure the electron arrival rates at both channeltrons of the Mott polarimeter, with the order in which the two channeltrons are measured varying, to protect against drift effects.

1. The sample was placed, according to the procedure in appendix A.1, in a position that had previously been determined (section 5.4) to direct the specularly reflected electron beam into the polarimeter.
2. One channeltron was chosen, connected to the data acquisition apparatus (chapter 3,) and switched on (table A.1.) If the procedure being described here had been performed previously, the channeltron chosen was the one that had not been chosen at the same stage in the preceding performance of this procedure. Otherwise, a channeltron was chosen at random.
3. A series of electron arrival rate measurements was taken, according to the procedure in appendix A.2.2.
4. The other channeltron was connected to the data acquisition apparatus (chapter 3) and switched on (table A.1.)

5. A series of electron arrival rate measurements was taken, according to the procedure in appendix A.2.2.

A.2.2 Procedure for Conducting Polarized Electron Measurements with One Channeltron

The purpose of this procedure is to obtain measurements of the electron arrival rate at the channeltron as a function of the incident beam energy, with a variable direction of variation of the beam energy, to protect against drift effects.

1. The electron gun's beam energy E_b was set to (500 ± 0.3) eV, with corresponding adjustments (table A.1) in the voltages on the polarimeter's front grid, thorium foil, and retarding grids.
2. The dwell time τ of the data acquisition apparatus (chapter 3) was set to 1 s. The reasons for choosing this dwell time are discussed in section 5.5.
3. The electron gun's beam current F was set to (4 ± 0.1) μ A.
4. A series of electron arrival rate measurements was taken, according to the procedure in appendix A.4.
5. τ was set to 50 ms. The reasons for choosing this dwell time are discussed in section 5.5.
6. Either an ascending or a descending order was chosen for incident beam energies E_b . If the procedure being described here had been performed previously, then the order chosen was opposite to that chosen in the preceding performance of the procedure. Otherwise, an order was chosen at random.
7. The electron gun beam energy, along with the voltages on the polarimeter's front grid, thorium foil, and retarding grids, was varied, in the chosen order, in 50 eV steps between 500 eV and 1 keV inclusive, with a random error of 300 meV in each beam energy.
8. At each of the beam energies, a series of electron arrival rate measurements was taken, according to the procedure in appendix A.3.

A.3 Procedure for Conducting Polarized Electron Reflection Measurements at One Beam Energy

1. Either an ascending or a descending order was chosen for incident beam currents F . If the procedure being described here had been performed previously, then the order chosen was opposite to that chosen in the preceding performance of the procedure. Otherwise, an order was chosen at random.
2. The electron gun beam current was varied, in the chosen order, in $2\ \mu\text{A}$ steps between $2\ \mu\text{A}$ and $6\ \mu\text{A}$.
3. At each of the beam currents, a series of electron arrival rate measurements was taken, according to the procedure in appendix A.4.

A.4 Procedure for Conducting Polarized Electron Reflection Measurements at One Beam Current

1. In each of 256 consecutive periods of τ , the number of electrons detected at the relevant channeltron was recorded; τ is a controllable parameter in the logging software, known as the dwell time. Its values for each of the individual performances for this procedure are specified above.

Appendix B

Auger Electron Spectrum Interpretation

Auger electron spectroscopy is [81, 82, 83] an experimental technique for determining the chemical composition of a sample, which involves measurement of the rate of secondary electrons leaving a sample, on bombardment with a primary electron beam, as a function of energy. The results are usually presented as a graph of $\frac{dN(E)}{dE}$ against E , where $N(E)dE$ is the rate of arrival at the detector of secondary electrons, of energies between E and $E + dE$. This graph contains a series of minima, each of which is generated by a particular chemical element or combination of chemical elements in the sample. It is possible to find look-up tables [83], which give the sensitivity $S_{E,X}$ of a minimum at energy E to element X .

The author has been unable to find, in the literature, any pointers to the construction of a model of the Auger process detailed enough to allow Bayesian inference of the posterior probability distribution over the thickness of a cobalt film on a copper surface, given a measured Auger spectrum. Therefore, the author has devised the following, rough method of estimating the thickness:

1. The “peak height” of a minimum at energy E can be estimated as

$$h_E = \frac{n_L + n_R - 2n_C}{2} \pm \left| \frac{n_L - n_R}{2} \right|, \quad (\text{B.1})$$

where n_C is the $\frac{dN(E)}{dE}$ value at the minimum, n_L that at the maximum immediately to the left of the minimum, and n_R that at the maximum immediately to the right of the minimum. This method is used to estimate $h_{777.5\text{eV}}$ and $h_{922\text{eV}}$, since both of these minima have non-zero sensitivities to both copper and cobalt.

2. It is assumed that, in terms of an effective copper concentration in the sample c_{Cu} , and an effective cobalt concentration c_{Co} ,

$$h_{777.5\text{ eV}} = S_{777.5\text{ eV},Cu}c_{Cu} + S_{777.5\text{ eV},Co}c_{Co}, \quad (\text{B.2})$$

and

$$h_{922\text{ eV}} = S_{922\text{ eV},Cu}c_{Cu} + S_{922\text{ eV},Co}c_{Co}. \quad (\text{B.3})$$

Therefore,

$$c_{Cu} = \frac{S_{922\text{ eV},Co}h_{777.5\text{ eV}} - S_{777.5\text{ eV},Co}h_{922\text{ eV}}}{S_{777.5\text{ eV},Cu}S_{922\text{ eV},Co} - S_{777.5\text{ eV},Co}S_{922\text{ eV},Cu}}, \quad (\text{B.4})$$

and

$$c_{Co} = \frac{S_{922\text{ eV},Cu}h_{777.5\text{ eV}} - S_{777.5\text{ eV},Cu}h_{922\text{ eV}}}{S_{777.5\text{ eV},Co}S_{922\text{ eV},Cu} - S_{777.5\text{ eV},Cu}S_{922\text{ eV},Co}}. \quad (\text{B.5})$$

3. The effective copper concentration due to copper between depths z and $z + dz$ is assumed to be

$$dc_{Cu} = A \exp(-\lambda z)dz, \quad (\text{B.6})$$

where the exponential factor represents the loss of incident electrons to inelastic scattering, the mean free path $\frac{1}{\lambda}$ of which can be found in look-up tables [83]. Therefore, for a cobalt thickness t , the total effective copper concentration is

$$\begin{aligned} c_{Cu} &= \int_{z=t}^{\infty} A \exp(-\lambda z)dz \\ &= \frac{A}{\lambda} \exp(-\lambda t). \end{aligned} \quad (\text{B.7})$$

Similarly,

$$\begin{aligned} c_{Co} &= \frac{A}{\lambda} (1 - \exp(-\lambda t)) \\ &= c_{Cu} (\exp(\lambda t) - 1) \end{aligned} \quad (\text{B.8})$$

$$\Rightarrow t = \frac{\ln\left(\frac{c_{Co}}{c_{Cu}} + 1\right)}{\lambda}. \quad (\text{B.9})$$

4. The estimate of cobalt thickness, in ordinary units of length, thus obtained can be compared with the thickness, in $\mu\text{A s}$, obtained from the ion flux monitor (section 4.3,) to give a conversion factor between the two unit systems.

Shortly before the experiments in section 5.4, two cobalt films were grown, and their thicknesses calibrated in this manner. The resulting conversion factors were $(104 \pm 20) \mu\text{m A}^{-1} \text{s}^{-1}$ and $(67 \pm 13) \mu\text{m A}^{-1} \text{s}^{-1}$. The average is $(78 \pm 11) \mu\text{m A}^{-1} \text{s}^{-1}$.

Since this estimate has been produced in the absence of a genuinely quantitative understanding of the Auger process, it should be treated with some scepticism; the large random error estimate quoted above, resulting from the differing base signals on either side of an Auger peak, embodies just such a healthy scepticism. Hope [37], who devised a thickness estimation method in a similar spirit, suggested that it may introduce an extra calibration error of $\sim 25\%$, of the same order as that quoted here.

It could be suggested that the errors in this estimate render Auger spectroscopy an unsuitable method of thickness measurement, compared with, say, the use of a quartz thickness monitor. It should be noted that Auger spectroscopy and the quartz thickness monitor play different roles in thickness measurement, and are not directly interchangeable. A quartz thickness monitor would reveal relative thicknesses, a task which is undertaken in this thesis, not with the Auger electron spectroscopy, but with the ion flux monitor in the cobalt evaporator. The Auger spectroscopy is used to calibrate the ion flux monitor, to produce absolute thicknesses; similar measures would be necessary for a quartz thickness monitor; one study [47] is an exception to this division of labour, having used Auger spectroscopy for relative thickness measurements, and a stylus profilometer, acting on thick films, for absolute calibration.

The literature on *Co/Cu* structures seems to reveal Auger electron spectroscopy as the usual method for achieving this calibration [38, 55, 59, 37]. The author is aware of one attempt [41] to calibrate the thickness monitor by observing the onset of ferro-magnetism with increasing thickness, then comparing with earlier measurements of the critical thickness for the onset of ferro-magnetism; however, these earlier measurements [55] were themselves made with a thickness monitor calibrated using Auger electron spectroscopy. Also, in one instance [38], the mono-layer-period oscillations in medium-energy electron diffraction and thermal-energy atom scattering intensity were used as back-ups to Auger electron spectroscopy for thickness calibration; the three methods produced results consistent with one another. Another alternative absolute thickness measurement method is scanning tunnelling microscopy [56], and one study [46] has used this as a means of calibrating an Auger electron spectroscopy apparatus, which was then used for relative thickness measurements. A third absolute thickness measurement method, which has been used [39] to calibrate a quartz thickness monitor, with a claimed calibration error of just 5%, is ‘*ex situ* X-ray interference.’

Part IV

Legal Notices

Appendix C

GNU Free Documentation License

Version 1.1, March 2000

Copyright © 2000 Free Software Foundation, Inc.
59 Temple Place, Suite 330, Boston, MA 02111-1307 USA
Everyone is permitted to copy and distribute verbatim copies of this license document, but changing it is not allowed.

Preamble

The purpose of this License is to make a manual, textbook, or other written document “free” in the sense of freedom: to assure everyone the effective freedom to copy and redistribute it, with or without modifying it, either commercially or noncommercially. Secondly, this License preserves for the author and publisher a way to get credit for their work, while not being considered responsible for modifications made by others.

This License is a kind of “copyleft”, which means that derivative works of the document must themselves be free in the same sense. It complements the GNU General Public License, which is a copyleft license designed for free software.

We have designed this License in order to use it for manuals for free software, because free software needs free documentation: a free program should come with manuals providing the same freedoms that the software does. But this License is not limited to software manuals; it can be used for any textual work, regardless of subject matter or whether it is published as a printed book. We recommend this License principally for works whose

purpose is instruction or reference.

C.1 Applicability and Definitions

This License applies to any manual or other work that contains a notice placed by the copyright holder saying it can be distributed under the terms of this License. The “Document”, below, refers to any such manual or work. Any member of the public is a licensee, and is addressed as “you”.

A “Modified Version” of the Document means any work containing the Document or a portion of it, either copied verbatim, or with modifications and/or translated into another language.

A “Secondary Section” is a named appendix or a front-matter section of the Document that deals exclusively with the relationship of the publishers or authors of the Document to the Document’s overall subject (or to related matters) and contains nothing that could fall directly within that overall subject. (For example, if the Document is in part a textbook of mathematics, a Secondary Section may not explain any mathematics.) The relationship could be a matter of historical connection with the subject or with related matters, or of legal, commercial, philosophical, ethical or political position regarding them.

The “Invariant Sections” are certain Secondary Sections whose titles are designated, as being those of Invariant Sections, in the notice that says that the Document is released under this License.

The “Cover Texts” are certain short passages of text that are listed, as Front-Cover Texts or Back-Cover Texts, in the notice that says that the Document is released under this License.

A “Transparent” copy of the Document means a machine-readable copy, represented in a format whose specification is available to the general public, whose contents can be viewed and edited directly and straightforwardly with generic text editors or (for images composed of pixels) generic paint programs or (for drawings) some widely available drawing editor, and that is suitable for input to text formatters or for automatic translation to a variety of formats suitable for input to text formatters. A copy made in an otherwise Transparent file format whose markup has been designed to thwart or discourage subsequent modification by readers is not Transparent. A copy that is not “Transparent” is called “Opaque”.

Examples of suitable formats for Transparent copies include plain ASCII without markup, Texinfo input format, \LaTeX input format, SGML or XML using a publicly available DTD, and standard-conforming simple HTML designed for human modification. Opaque formats include PostScript, PDF,

proprietary formats that can be read and edited only by proprietary word processors, SGML or XML for which the DTD and/or processing tools are not generally available, and the machine-generated HTML produced by some word processors for output purposes only.

The “Title Page” means, for a printed book, the title page itself, plus such following pages as are needed to hold, legibly, the material this License requires to appear in the title page. For works in formats which do not have any title page as such, “Title Page” means the text near the most prominent appearance of the work’s title, preceding the beginning of the body of the text.

C.2 Verbatim Copying

You may copy and distribute the Document in any medium, either commercially or noncommercially, provided that this License, the copyright notices, and the license notice saying this License applies to the Document are reproduced in all copies, and that you add no other conditions whatsoever to those of this License. You may not use technical measures to obstruct or control the reading or further copying of the copies you make or distribute. However, you may accept compensation in exchange for copies. If you distribute a large enough number of copies you must also follow the conditions in section 3.

You may also lend copies, under the same conditions stated above, and you may publicly display copies.

C.3 Copying in Quantity

If you publish printed copies of the Document numbering more than 100, and the Document’s license notice requires Cover Texts, you must enclose the copies in covers that carry, clearly and legibly, all these Cover Texts: Front-Cover Texts on the front cover, and Back-Cover Texts on the back cover. Both covers must also clearly and legibly identify you as the publisher of these copies. The front cover must present the full title with all words of the title equally prominent and visible. You may add other material on the covers in addition. Copying with changes limited to the covers, as long as they preserve the title of the Document and satisfy these conditions, can be treated as verbatim copying in other respects.

If the required texts for either cover are too voluminous to fit legibly, you should put the first ones listed (as many as fit reasonably) on the actual

cover, and continue the rest onto adjacent pages.

If you publish or distribute Opaque copies of the Document numbering more than 100, you must either include a machine-readable Transparent copy along with each Opaque copy, or state in or with each Opaque copy a publicly-accessible computer-network location containing a complete Transparent copy of the Document, free of added material, which the general network-using public has access to download anonymously at no charge using public-standard network protocols. If you use the latter option, you must take reasonably prudent steps, when you begin distribution of Opaque copies in quantity, to ensure that this Transparent copy will remain thus accessible at the stated location until at least one year after the last time you distribute an Opaque copy (directly or through your agents or retailers) of that edition to the public.

It is requested, but not required, that you contact the authors of the Document well before redistributing any large number of copies, to give them a chance to provide you with an updated version of the Document.

C.4 Modifications

You may copy and distribute a Modified Version of the Document under the conditions of sections 2 and 3 above, provided that you release the Modified Version under precisely this License, with the Modified Version filling the role of the Document, thus licensing distribution and modification of the Modified Version to whoever possesses a copy of it. In addition, you must do these things in the Modified Version:

- Use in the Title Page (and on the covers, if any) a title distinct from that of the Document, and from those of previous versions (which should, if there were any, be listed in the History section of the Document). You may use the same title as a previous version if the original publisher of that version gives permission.
- List on the Title Page, as authors, one or more persons or entities responsible for authorship of the modifications in the Modified Version, together with at least five of the principal authors of the Document (all of its principal authors, if it has less than five).
- State on the Title page the name of the publisher of the Modified Version, as the publisher.
- Preserve all the copyright notices of the Document.

- Add an appropriate copyright notice for your modifications adjacent to the other copyright notices.
- Include, immediately after the copyright notices, a license notice giving the public permission to use the Modified Version under the terms of this License, in the form shown in the Addendum below.
- Preserve in that license notice the full lists of Invariant Sections and required Cover Texts given in the Document's license notice.
- Include an unaltered copy of this License.
- Preserve the section entitled "History", and its title, and add to it an item stating at least the title, year, new authors, and publisher of the Modified Version as given on the Title Page. If there is no section entitled "History" in the Document, create one stating the title, year, authors, and publisher of the Document as given on its Title Page, then add an item describing the Modified Version as stated in the previous sentence.
- Preserve the network location, if any, given in the Document for public access to a Transparent copy of the Document, and likewise the network locations given in the Document for previous versions it was based on. These may be placed in the "History" section. You may omit a network location for a work that was published at least four years before the Document itself, or if the original publisher of the version it refers to gives permission.
- In any section entitled "Acknowledgements" or "Dedications", preserve the section's title, and preserve in the section all the substance and tone of each of the contributor acknowledgements and/or dedications given therein.
- Preserve all the Invariant Sections of the Document, unaltered in their text and in their titles. Section numbers or the equivalent are not considered part of the section titles.
- Delete any section entitled "Endorsements". Such a section may not be included in the Modified Version.
- Do not retitle any existing section as "Endorsements" or to conflict in title with any Invariant Section.

If the Modified Version includes new front-matter sections or appendices that qualify as Secondary Sections and contain no material copied from the Document, you may at your option designate some or all of these sections as invariant. To do this, add their titles to the list of Invariant Sections in the Modified Version's license notice. These titles must be distinct from any other section titles.

You may add a section entitled "Endorsements", provided it contains nothing but endorsements of your Modified Version by various parties – for example, statements of peer review or that the text has been approved by an organization as the authoritative definition of a standard.

You may add a passage of up to five words as a Front-Cover Text, and a passage of up to 25 words as a Back-Cover Text, to the end of the list of Cover Texts in the Modified Version. Only one passage of Front-Cover Text and one of Back-Cover Text may be added by (or through arrangements made by) any one entity. If the Document already includes a cover text for the same cover, previously added by you or by arrangement made by the same entity you are acting on behalf of, you may not add another; but you may replace the old one, on explicit permission from the previous publisher that added the old one.

The author(s) and publisher(s) of the Document do not by this License give permission to use their names for publicity for or to assert or imply endorsement of any Modified Version.

C.5 Combining Documents

You may combine the Document with other documents released under this License, under the terms defined in section 4 above for modified versions, provided that you include in the combination all of the Invariant Sections of all of the original documents, unmodified, and list them all as Invariant Sections of your combined work in its license notice.

The combined work need only contain one copy of this License, and multiple identical Invariant Sections may be replaced with a single copy. If there are multiple Invariant Sections with the same name but different contents, make the title of each such section unique by adding at the end of it, in parentheses, the name of the original author or publisher of that section if known, or else a unique number. Make the same adjustment to the section titles in the list of Invariant Sections in the license notice of the combined work.

In the combination, you must combine any sections entitled "History" in the various original documents, forming one section entitled "History";

likewise combine any sections entitled “Acknowledgements”, and any sections entitled “Dedications”. You must delete all sections entitled “Endorsements.”

C.6 Collections of Documents

You may make a collection consisting of the Document and other documents released under this License, and replace the individual copies of this License in the various documents with a single copy that is included in the collection, provided that you follow the rules of this License for verbatim copying of each of the documents in all other respects.

You may extract a single document from such a collection, and distribute it individually under this License, provided you insert a copy of this License into the extracted document, and follow this License in all other respects regarding verbatim copying of that document.

C.7 Aggregation With Independent Works

A compilation of the Document or its derivatives with other separate and independent documents or works, in or on a volume of a storage or distribution medium, does not as a whole count as a Modified Version of the Document, provided no compilation copyright is claimed for the compilation. Such a compilation is called an “aggregate”, and this License does not apply to the other self-contained works thus compiled with the Document, on account of their being thus compiled, if they are not themselves derivative works of the Document.

If the Cover Text requirement of section 3 is applicable to these copies of the Document, then if the Document is less than one quarter of the entire aggregate, the Document’s Cover Texts may be placed on covers that surround only the Document within the aggregate. Otherwise they must appear on covers around the whole aggregate.

C.8 Translation

Translation is considered a kind of modification, so you may distribute translations of the Document under the terms of section 4. Replacing Invariant Sections with translations requires special permission from their copyright holders, but you may include translations of some or all Invariant Sections

in addition to the original versions of these Invariant Sections. You may include a translation of this License provided that you also include the original English version of this License. In case of a disagreement between the translation and the original English version of this License, the original English version will prevail.

C.9 Termination

You may not copy, modify, sublicense, or distribute the Document except as expressly provided for under this License. Any other attempt to copy, modify, sublicense or distribute the Document is void, and will automatically terminate your rights under this License. However, parties who have received copies, or rights, from you under this License will not have their licenses terminated so long as such parties remain in full compliance.

C.10 Future Revisions of This License

The Free Software Foundation may publish new, revised versions of the GNU Free Documentation License from time to time. Such new versions will be similar in spirit to the present version, but may differ in detail to address new problems or concerns. See <http://www.gnu.org/copyleft/>.

Each version of the License is given a distinguishing version number. If the Document specifies that a particular numbered version of this License "or any later version" applies to it, you have the option of following the terms and conditions either of that specified version or of any later version that has been published (not as a draft) by the Free Software Foundation. If the Document does not specify a version number of this License, you may choose any version ever published (not as a draft) by the Free Software Foundation.

ADDENDUM: How to use this License for your documents

To use this License in a document you have written, include a copy of the License in the document and put the following copyright and license notices just after the title page:

Copyright © YEAR YOUR NAME. Permission is granted to copy, distribute and/or modify this document under the terms of the GNU Free Documentation License, Version 1.1 or any later

version published by the Free Software Foundation; with the Invariant Sections being LIST THEIR TITLES, with the Front-Cover Texts being LIST, and with the Back-Cover Texts being LIST. A copy of the license is included in the section entitled “GNU Free Documentation License”.

If you have no Invariant Sections, write “with no Invariant Sections” instead of saying which ones are invariant. If you have no Front-Cover Texts, write “no Front-Cover Texts” instead of “Front-Cover Texts being LIST”; likewise for Back-Cover Texts.

If your document contains nontrivial examples of program code, we recommend releasing these examples in parallel under your choice of free software license, such as the GNU General Public License, to permit their use in free software.

Bibliography

- [1] F. B. Dunning and G. K. Walters. Elastic spin-polarized low-energy electron scattering from non-magnetic surfaces. In Feder [100], chapter 6, pages 287–320.
- [2] J. D. Lang, K. D. Jamison, F. B. Dunning, G. K. Walters, M. A. Passler, A. Ignatiev, E. Tamura, and R. Feder. Spin polarization in low-energy electron diffraction from $Ni(001)$ and $Ni(001)c(2 \times 2)Te$. *Surface Science*, 123(2–3):247–263, 1982.
- [3] Klaus Peter Kopper. Electron spin polarimetry studies of ultra-thin magnetic films. M.phil. dissertation, University of Cambridge, Selwyn College, August 2002.
- [4] U. Gradmann and S. F. Alvarado. Elastic spin-polarized low-energy electron scattering from magnetic surfaces. In Feder [100], chapter 7, pages 321–352.
- [5] T. J. Gay and F. B. Dunning. Mott electron polarimetry. *Review of Scientific Instruments*, 63(2):1635–1651, February 1992.
- [6] G. C. Burnett, T. J. Monroe, and F. B. Dunning. High-efficiency retarding-potential Mott polarization analyzer. *Review of Scientific Instruments*, 65(6):1893–1896, June 1994.
- [7] A. Vega, J. C. Parlebas, and C. Demangeat. Electronic structure calculations of low-dimensional transition-metals. In K. Buschow, editor, *Handbook of Magnetic Materials*. December 2002. Draft version.
- [8] D[aniel] C[hristopher] Hatton. Mott polarimetry at the Cavendish Laboratory. First year report, University of Cambridge, December 2000.
- [9] G. F. Weston. *Ultrahigh vacuum practice*. Butterworths, London, 1985.

- [10] D[aniel] C[hristopher] Hatton. Some philosophical implications of Bayesian statistics: Departure from positivism and association with standpoint epistemology. World-Wide Web page, 2002–2003. In preparation.
- [11] N. Thangaraj, C. Echer, Kannan M. Krishnan, R. F. C. Farrow, R. F. Marks, and S. S. P. Parkin. Giant magnetoresistance and microstructural characteristics of epitaxial *Fe-Ag* and *Co-Ag* granular thin films. *Journal of Applied Physics*, 75(10):6900–6902, May 1994.
- [12] Q. Jiang, H. N. Yang, and G. C. Wang. Correlation between dynamic magnetic hysteresis loops and nanoscale roughness of ultrathin *Co* films. *Journal of Vacuum Science and Technology B: Microelectronics and Nanometer Structures. Processing Measurement and Phenomena*, 14(4):3180–3188, August 1996.
- [13] P. M. Dodd, R. Atkinson, P. Papakonstantinou, M. S. Araghi, and H. S. Gamble. Correlation between crystalline structure and soft magnetic properties in sputtered sendust films. *Journal of Applied Physics*, 81(8):4104–4106, April 1997.
- [14] B.-Ch. Choi, P. J. Bode, and J. A. C. Bland. Formation of a two-dimensional $c(2 \times 2)$ *Mn-Co*(001) ferromagnetic surface alloy on *Cu*(001). *Physical Review B: Condensed Matter and Materials Physics*, 58(9):5166–5168, September 1998. URL: <http://homer.phy.cam.ac.uk/publications/papers98/prbbc1.pdf>.
- [15] B.-Ch. Choi, P. J. Bode, and J. A. C. Bland. Magnetic anisotropy strength and surface alloy formation in *Mn/Co/Cu*(001) overlays. *Physical Review B: Condensed Matter and Materials Physics*, 59(10):7029–7032, March 1999. URL: <http://homer.phy.cam.ac.uk/publications/papers99/prbc1.pdf>.
- [16] B.-Ch. Choi, P. J. Bode, and J. A. C. Bland. Structure and magnetic properties of a two-dimensional $c(2 \times 2)$ *Mn-Co/Cu*(001) surface alloy. *Journal of Applied Physics*, 85(8):5063–5065, April 1999. URL: <http://homer.phy.cam.ac.uk/publications/papers99/japc1.pdf>.
- [17] M. Wuttig, Y. Gauthier, and S. Blügel. Magnetically driven buckling and stability of ordered surface alloys—*Cu*(100) $c2 \times 2$ *Mn*. *Physical Review Letters*, 70:3619–3622, 1993. Cited in [14].

- [18] R. G. P. van der Kraan and H. van Kempen. Growth of *Mn* on *Cu*(100) studied by STM—the $c(2 \times 2)$ and $p(4 \times 2)$ ordered surface alloys. *Surface Science*, 338:19–30, 1995. Cited in [14].
- [19] M. T. Kief and W. F. Egelhoff. Growth and structure of *Fe* and *Co* thin-films on *Cu*(111), *Cu*(100) and *Cu*(110)—a comprehensive study of metastable film growth. *Physical Review B: Condensed Matter and Materials Physics*, 47:10785–10814, 1993. Cited in [37, 99].
- [20] E. Tamura, S. Bluegel, and R. Feder. On the determination of surface antiferromagnetism by low-energy electron-diffraction. *Solid State Communications*, 65:1255–1257, 1988. Cited in [15].
- [21] A. Noguera, S. Bouarab, A. Mokrani, C. Demangeat, and H. Dreyssé. Very thin *Mn* films on fcc *Co*(001). *Journal of Magnetism and Magnetic Materials*, 156(1–3):21–22, April 1996.
- [22] S. Meza-Aguilar, O. Elmouhssine, H. Dreyssé, and C. Demangeat. Two-dimensional surface ordered *Mn-Co* alloys on *Co*(001). *Physical Review B: Condensed Matter and Materials Physics*, 63(6):064421–1–064421–6, February 2001.
- [23] B. M’Passi-Mabiala, S. Meza[-]Aguilar, and C. Demangeat. Ferromagnetic ground state for *Mn-Co* surface ordered alloy on a *Co*(001) substrate. *Physical Review B: Condensed Matter and Materials Physics*, 65(1):012414–1–012414–3, January 2002. URL: http://www.ictp.trieste.it/cgi-bin/ICTPpreprints/swish.11/swish-web.cgi?keywords=IC2001084*.
- [24] R. Feder. Principles and theory of electron scattering and photoemission. In *Polarized Electrons in Surface Physics* [100], chapter 4, pages 125–241.
- [25] D[avid] M[elvin] Lind, K. D. Jamison, F. B. Dunning, G. K. Walters, and H. L. Davis. An experimental/theoretical comparison of spin-polarized low energy electron diffraction from the *Cu*(100) surface. *Journal of Vacuum Science and Technology A: Vacuum, Surfaces, and Films*, 4(3):1271–1273, May–June 1986.
- [26] D[avid] M[elvin] Lind, F. B. Dunning, G. K. Walters, and H. L. Davis. Surface-structural analysis by use of spin-polarized low-energy electron diffraction: An investigation of the *Cu*(100) surface. *Physical Review B: Condensed Matter and Materials Physics*, 35(17):9037–9044, June 1987.

- [27] C. G. Darwin. On the diffraction of the magnetic electron. *Proceedings of the Royal Society of London Series A: Mathematical and Physical Sciences*, 120:631–642, 1928.
- [28] S. J. Blundell and J. A. C. Bland. Polarized neutron reflection as a probe of magnetic-films and multilayers. *Physical Review B: Condensed Matter and Materials Physics*, 46(6):3391–3400, August 1992.
- [29] S. J. Blundell and J. A. C. Bland. Polarised neutron reflection as a probe of in-plane magnetisation vector rotation in magnetic multilayers. *Journal of Magnetism and Magnetic Materials*, 121:185–188, 1993.
- [30] Alastair I. M. Rae. *Quantum Mechanics*. Institute of Physics Publishing, Bristol, 3rd edition, 1992.
- [31] Joachim Kessler. *Polarized Electrons*. Texts and Monographs in Physics. Springer-Verlag, Berlin, 1976.
- [32] Joachim Kessler. *Polarized Electrons*. Springer Series on Atoms and Plasmas. Springer-Verlag, Berlin, 2nd edition, 1985.
- [33] L. A. Hodge, T. J. Moravec, F. B. Dunning, and G. K. Walters. Mott electron spin polarization analysis system of novel design. *Review of Scientific Instruments*, 50:5–8, 1979.
- [34] F. B. Dunning. Mott electron polarimetry. *Nuclear Instruments and Methods in Physics Research A: Accelerators, Spectrometers, Detectors and Associated Equipment*, 347(1–3):152–160, August 1994.
- [35] P. Hammond. *Electromagnetism for Engineers: An Introductory Course*. Number 7 in Textbooks in Electrical and Electronic Engineering. Oxford University Press, Oxford, fourth edition, 1997.
- [36] M. T. Johnson, P. J. H. Bloemen, F. J. A. van den Broeder, and J. J. de Vries. Magnetic anisotropy in metallic multilayers. *Reports on Progress in Physics*, 59(11):1409–1458, November 1996. URL: <http://www.physics.uwa.edu.au/pub/EMC/r611r2.pdf>.
- [37] Stephen Hope. *Spin Polarised Radiation Studies of Ultrathin Magnetic Films*. PhD thesis, University of Cambridge, Downing College, October 1997.
- [38] C. M. Schneider, P. Bressler, P. Schuster, J. Kirschner, J. J. Demiguel, and R. Miranda. Curie-temperature of ultrathin films of FCC cobalt

- epitaxially grown on atomically flat $Cu(100)$ surfaces. *Physical Review Letters*, 64:1059–1062, February 1990.
- [39] P. Krams, F. Lauks, R. L. Stamps, B. Hillebrands, and G. Güntherodt. Magnetic anisotropies of ultrathin $Co(001)$ films on $Cu(001)$. *Physical Review Letters*, 69(25):3674–3677, December 1992.
- [40] B. Heinrich and J. F. Cochran. Ultrathin metallic magnetic films: magnetic anisotropies and exchange interactions. *Advances in Physics*, 42(5):523–639, 1993.
- [41] M. E. Buckley, S[tephen] Hope, F. O. Schumann, and J. A. C. Bland. Variations in the magnetic properties of ultrathin Co films due to the adsorption of non-magnetic metal atoms at the Co /vacuum interface. *Journal of Magnetism and Magnetic Materials*, 156(1–3):211–212, April 1996.
- [42] J. A. C. Bland, S[tephen] Hope, M. Tselepi, and B.[-Ch.] Choi. Atomic scale evolution of magnetic anisotropies. *Journal of Physics D: Applied Physics*, 31(6):622–629, March 1998.
- [43] V. L. Moruzzi, J. F. Janak, and A. R. Williams. *Calculated Electronic Properties of Metals*. Pergamon Press, New York, 1978.
- [44] N. W. Ashcroft and N. D[avid] Mermin. *Solid State Physics*. Harcourt Brace & Company, Orlando, 1976.
- [45] Stephen Gasiorowicz. *Quantum Physics*. John Wiley & Sons, New York, second edition, 1996.
- [46] U. Ramsperger, A. Vaterlaus, P. Pfäffli, U. Maier, and D. Pescia. Growth of Co on a stepped and on a flat $Cu(001)$ surface. *Physical Review B: Condensed Matter and Materials Physics*, 53(12):8001–8006, March 1996.
- [47] W. Weber, C. H. Back, A. Bischof, Ch. Würsch, and R. Allenspach. Morphology-induced oscillations of the magnetic anisotropy in ultrathin Co films. *Physical Review Letters*, 76(11):1940–1943, March 1996.
- [48] F. G. Gallagher and J. R. Shakeshaft. Mathematical formulae: A handbook with table of physical constants. On sale at the Cavendish Stores, Cavendish Laboratory, University of Cambridge, Madingley Road, Cambridge, UK. CB3 0HE. Version 1.4.

- [49] Kelvin probe FAQ page. World-Wide Web page, October 2001. URL: <http://www.mcallister.com/kpfaqpg.html>.
- [50] Periodic table of elements. World-Wide Web page, 2001. URL: <http://www.environmentalchemistry.com/yogi/periodic/>.
- [51] W. Weber, D. Oberli, S. Riesen, and H. C. Siegmann. The electron analogue to the Faraday rotation. *New Journal of Physics*, 1:9, May 1999. URL: <http://stacks.iop.org/NJP/1/9/>.
- [52] David John Cameron MacKay. *Bayesian Methods for Adaptive Models*. PhD thesis, California Institute of Technology, Computation and Neural Systems, 1992. URL: <http://www.inference.phy.cam.ac.uk/mackay/PhD.html>.
- [53] P[hilip] W. Anderson. More is different: Broken symmetry and the nature of the hierarchical structure of science. *Science*, 177(4047):393–396, August 1972.
- [54] A. Taylor and Brenda J. Kagle. *Crystallographic Data on Metal and Alloy Structures*. Dover Publications, New York, 1963.
- [55] L. Smardz, U. Koebler, D. Kerkmann, F. Schumann, D. Pescia, and W. Zinn. Room-temperature ferromagnetism of the *Co* monolayer on *Cu*(100). *Zeitschrift für Physik B: Condensed Matter*, 80:1–2, 1990.
- [56] A. K. Schmid, D. Atlan, H. Itoh, B. Heinrich, T. Ichinokawa, and J. Kirschner. Fast interdiffusion in thin films: Scanning-tunneling-microscopy determination of surface diffusion through microscopic pinholes. *Physical Review B: Condensed Matter and Materials Physics*, 48(4):2855–2861, August 1993.
- [57] W. Weber, A. Bischof, R. Allenspach, C. H. Back, J. Fassbender, U. May, B. Schirmer, R. M. Jungblut, G. Güntherodt, and B. Hillebrands. Structural relaxation and magnetic anisotropy in *co/cu*(001) films. *Physical Review B: Condensed Matter and Materials Physics*, 54(6):4075–4079, August 1996.
- [58] W. Weber, A. Bischof, R. Allenspach, Ch. Würsch, C. H. Back, and D. Pescia. Oscillatory magnetic anisotropy and quantum well states in *Cu/Co/Cu*(100) films. *Physical Review Letters*, 76(18):3424–3427, April 1996.

- [59] F. O. Schumann, M. E. Buckley, and J. A. C. Bland. Paramagnetic-ferromagnetic phase transition during growth of ultrathin *co/cu*(001) films. *Physical Review B: Condensed Matter and Materials Physics*, 50(22):16424–16427, December 1994.
- [60] J. A. C. Bland, B.-Ch. Choi, S[tephen] Hope, and M. Tselepi. Atomic scale evolution of magnetic anisotropies. *Journal of Magnetism and Magnetic Materials*, 197:8–12, May 1999.
- [61] H. P. J. Wijn, editor. *Magnetic Properties of Metals: d-Elements, Alloys and Compounds*. Data in Science and Technology. Springer-Verlag, Berlin, 1991.
- [62] J. Kirschner. Sources and detectors for polarized electrons. In Feder [100], chapter 5, pages 245–286.
- [63] J. Kirschner. Inelastic electron scattering by ferromagnets. In Feder [100], chapter 8, pages 353–383.
- [64] M. Landolt. Spin polarized secondary electron emission from ferromagnets. In Feder [100], chapter 9, pages 385–421.
- [65] David Melvin Lind. *Studies of Surface Geometric and Magnetic Structure Utilizing Spin-Polarized Low-Energy Electron Diffraction: Cu(001) and Ni(111)*. PhD thesis, Rice University, December 1987.
- [66] Dr. Sjuts Optotechnik, Katlenburg-Lindau. *Channel Electron Multipliers Series KBL*. URL: <http://www.sjuts.com/>.
- [67] U. Heinzmann. Photoemission and absorption spectroscopy of solids and interfaces with synchrotron radiation. In M. Campagna and R. Ro-
sei, editors, *Photoemission and Absorption Spectroscopy of Solids and Interfaces with Synchrotron Radiation*, Proceedings of the International School of Physics “Enrico Fermi”. North-Holland, Amsterdam, 1990. Cited in [34].
- [68] G. A. Mulhollan, A. B. Andrews, and J. L. Erskine. Layer-dependent spin-polarized 3*p* core level photoemission from ultrathin *Fe* films. *Physical Review B: Condensed Matter and Materials Physics*, 46:11212–11215, 1992. Cited in [34].
- [69] N. Sherman. Coulomb scattering of relativistic electrons by point nuclei. *Physical Review*, 103:1601–1607, 1956.

- [70] R. Bertacco, D. Onofrio, and F. Ciccacci. A novel electron spin-polarization detector with very large analyzing power. *Review of Scientific Instruments*, 70(9):3572–3576, September 1999.
- [71] X. Zhang, H. Hsu, F. B. Dunning, and G. K. Walters. Low-energy-electron probing depths in metals. *Physical Review B: Condensed Matter and Materials Physics*, 44:9133–9136, 1991. Cited in [34].
- [72] F. B. Dunning, C. Tang, and G. K. Walters. Use of thick gold foils in retarding-potential Mott polarimeters. *Review of Scientific Instruments*, 58:2195–2196, 1987. Cited in [34].
- [73] SPECS, Berlin. *User’s Manual: ErLEED Digital*, 2.0 edition, August 1997.
- [74] Varian, Palo Alto. *LEED/Auger Electron Gun Model #981-2125: Instruction Manual*, August 1978.
- [75] vacuum technology. In Hoiberg [101].
- [76] M. Luntz. Radiation: Tertiary effects of radiation on materials: Surface effects. In Hoiberg [101].
- [77] F. P. Bowden and D. Tabor. *Friction and Lubrication*. Methuen’s Physical Monographs. Methuen & Company, London, revised reprint edition, 1967.
- [78] Fisons VG Microtech. *Operating Instructions: AG5000*, 1 edition, March 1991.
- [79] M. Wells. Thin films—molecular beam epitaxy. Workshop lecture Preparation of Magnetic Materials: 6, Institute of Physics, Postgraduate Workshop in Magnetism, November 28 2001.
- [80] Omicron Vakuumphysik, Taunusstein. *Instruction Manual: UHV Evaporator E F M 3*, 1.6 edition, November 1992.
- [81] Ch. Linsmeier. Auger electron spectroscopy. In J. M. Walls and R. Smith, editors, *Surface Science Techniques*. Pergamon Press, Oxford, 1994.
- [82] Ch. Linsmeier. Auger electron spectroscopy. *Vacuum*, 45:673–690, 1994.

- [83] Kenton D. Childs, Brad A. Carlson, Lori A. LaVanier, John F. Moulder, Dennis F. Paul, William F. Stickle, and David G. Watson. *Handbook of Auger Electron Spectroscopy: A Book of Reference Data for Identification and Interpretation in Auger Electron Spectroscopy*. Physical Electronics, Eden Prairie, third edition, 1995.
- [84] Mary L. Boas. *Mathematical Methods in the Physical Sciences*. John Wiley & Sons, New York, second edition, 1983.
- [85] David J[ohn] C[ameron] MacKay. Bayesian interpolation. *Neural Computation*, 4(3):415–447, May 1992. URL: <http://www.inference.phy.cam.ac.uk/mackay/inter.nc.ps.gz>.
- [86] Ian James. Evolving three-dimensional structures in atmospheric flow: visualisation and communication. Workshop lecture, National Institute for Environmental eScience, Workshop on visualisation techniques for environmental escience, January 28 2003.
- [87] Dick Crawford. *gnuplot*, December 1998. URL: <http://www.ucc.ie/gnuplot/gnuplot.html>.
- [88] OriginLab Corporation. *Getting Started Manual*, English version 7.5 edition. URL: <http://www.originlab.com/pdfs/GettingStarted.PDF>.
- [89] Harold Jeffreys. *Theory of Probability*. The International Series of Monographs on Physics. Clarendon Press, Oxford, third edition, 1961.
- [90] David J[ohn] C[ameron] MacKay. Information theory, inference, and learning algorithms. World Wide Web page, February 25 2002. Draft 2.4.1. URL: <http://www.inference.phy.cam.ac.uk/itprnn/book.html>.
- [91] William H. Press, Brian P. Flannery, Saul A. Teukolsky, and William T. Vetterling. *Numerical Recipes: The Art of Scientific Computing*. Cambridge University Press, Cambridge, 1986.
- [92] Colin Howson and Peter Urbach. *Scientific Reasoning: the Bayesian Approach*. Open Court Publishing Company, La Salle, 1989.
- [93] David J[ohn] C[ameron] MacKay. Information theory, inference, and learning algorithms. World Wide Web page, January 2001. Draft 2.2.1. URL: <http://www.inference.phy.cam.ac.uk/itprnn/book.html>.

- [94] J. J. McClelland, M. R. Scheinfein, and D. T. Pierce. Use of thorium as a target in electron spin analyzers. *Review of Scientific Instruments*, 60(4):683–687, April 1989.
- [95] David Manura. Math2. World-Wide Web page, 2002. URL: <http://www.math2.org/index.xml>.
- [96] Engineering statistics handbook. World-Wide Web page. URL: <http://www.itl.nist.gov/div898/handbook/>.
- [97] F. Bordoni. Channel electron multiplier efficiency for 10–1000 eV electrons. *Nuclear Instruments and Methods*, 97:405–408, 1971.
- [98] Carlos Ramirez. Perl documentation. World-Wide Web page, June 2002. URL: <http://www.perldoc.com/>.
- [99] S[tephen] Hope, E. Gu, B.-Ch. Choi, and J. A. C. Bland. Spin engineering in ultrathin *Cu/Co/Cu(110)*. *Physical Review Letters*, 80(8):1750–1753, February 1998.
- [100] R. Feder, editor. *Polarized Electrons in Surface Physics*. Advanced Series in Surface Science. World Scientific Publishing, Singapore, 1985.
- [101] Encyclopaedia Britannica CD 99 multimedia edition. CD-ROM Distributed by Encyclopaedia Britannica, Chicago, 1999.